UNIVERSITÀ
DEGLI STUDI
DI PADOVA

Università degli Studi di Padova

Department of Industrial Engineering

Ph.D Course in

Science and Engineering of Materials and Nanostructures

XXIX Cycle

INTEGRATED MICRO AND NANO SYSTEMS FOR PHOTONIC DETECTION IN LIQUIDS

Coordinator: Ch.mo Prof. Gaetano Granozzi

Supervisor: Ch.mo Prof. Giovanna Brusatin

Co-Supervisor: Dr.ssa Laura Brigo

Ph.D student: Sujatha Giacomazzo

Abstract

The aim of this Ph.D. work was the study of functional materials and micro/nano structures for the realization of optical sensors for chemical or biological species in liquid media. The research was focused on two different areas of interest: biology and food industry. A disorder of zinc metabolism is closely associated with severe diseases, including diabetes. Functional and porous sol-gel films, doped with a fluorescent molecule, able to detect Zn^{2+} down to the nanomolar range were engineered. The systems allow to detect dynamic concentrations in time, showing selectivity overall other ions, stability provided by covalent binding of the fluorophore, and most relevantly reversibility. The second part of the dissertation is focused on the detection of residual antibiotics. The concern for food safety in milk industry has determined definition of residue levels of antibiotics in milk samples. Strong interest is evident in the development of high sensitivity optical sensors, giving reliable responses and allowing in situ multiple antibiotics detection. Two different plasmonic architectures for performing high-sensitive, selective and cost-effective detection of residual antibiotics in milk, and in particular of ampicillin, were developed. An SPR-based sensing strategy which consists in the combination of resonant optical and magnetic properties in a single nanostructure, and a plasmonic sinusoidal grating coupling supporting the propagation LRSPPs were studied. Selectivity is achieved by functionalization with specific aptamers.

Even if further in-depth investigations are needed, this work has provided awareness and competence of the fabrication techniques and analytical instruments for characterization and use of the developed devices.

Index

Introduction

Biosensors are devices exploited for the detection of analytes, that combine a biological element with a physiochemical detector, and convert the response into an electrical signal by the transducer [1]; in general they can be classified by measurand (physical quantities, chemical quantities and biological quantities) or by method (thermal, optical, electrical and magnetic). They can provide cost-effective, easy-to-use, sensitive and highly accurate detection in many research fields and commercial application ranging from clinical through to environmental, agricultural and even food industry.

As regards to its performance, a sensor has basic characteristics to be considered:

- *Measurand range*: corresponds to the specification of upper and lower limits of measurand values that a sensor can measure;

- *Repeatability* and *reproducibility*: is the ability to reproduce an output reading when the same measurand value is applied to the sensor consecutively under the same conditions;

- *Response time*: is defined as the amount of time required for the output to raise to a specific percentage, usually 90, 95 or 98 % of its final value;

- *Sensitivity*: is defined as the change in sensor response to the change in the value of measurand;

- *Detection limit*: is the smallest change in measurand that will result in measurable change in sensor response; often it has different values in different portions of the range;

- *Environmental effect*: when a measure is conducted with a sensor, external and environmental conditions have to be considered because may influence the output. For example, pH, temperature and the presence of other compounds could influence an optical chemical sensor due to the change in reactivity of analyte or indicator molecule;

- *Selectivity*: it is an important characteristic for chemical sensors used to detect concentration of a specific compound or ion; the more the sensor is selective, the more accurate and reliable is the measure, and this is really important especially in sensors with very low detection limit.

- *Reversibility:* it is a key parameter, as sensor can be used to track analyte fluctuations over the course of selected time periods.

Over the past two decades, the potential to detect very small amounts of analytes has driven research toward chemical and biological sensors based on different principles [2]. Miniaturization is an increasing request to get sensors more suitable for first response, law enforcement and military missions. Many and many applications for chemical sensors are found in chemical analysis, environmental monitoring, medicine, industry, etc. A great number of chemical sensors have been developed and commercialized over the last decades. The chemical sensors in general are based on potentiometric, amperometric and spectroscopic principles and many of them are specialized to specific requirements that allow measurement of only one element, molecule or ion. This measurement is performed in batch solution or in a flow configuration, monitoring the trend of concentration. The fast growing market and requirements such as small sample consumption (due to high cost of reagents and minimum detectable concentration) and devices portability are the driving force for the development of microsensors and micro total analysis systems. This work is focused on synthesis of novel miniaturized optical sensors for the detection of biological and chemical species in liquid media.

This Ph.D project study was focused on the development of functional materials and micro/nano structures for the realization of biosensors in two different areas of interest, where high sensitivity and in situ systems are demanded:

1- biological application; lowered circulating levels of zinc are found in diabetes mellitus.
The techniques for monitoring insulin provide remarkable temporal resolution, but they suffer of considerable drawbacks: they are very limited in spatial aspects of insulin release, are applicable only to a single cell at a time, and can disrupt plasma membranes. Fluorescent sensors were suggested as a possible solution to detect zinc divalent ions as they answer to a request of sensitive and non-invasive technique to accomplish real-time, local and reversible detection of specific analytes.

Several efforts were taken to minimize the response time of the sensor, to achieve reproducibility and to obtain a reversible system by investigating the behaviour of several fluorescent molecules and proper matrices.

2- food industry; excessive use of antibiotics in dairy cow diet has given rise to stronger bacterial resistance; therefore the concern for food safety in milk industry has determined their definition levels. The general idea was to develop two plasmonic architectures, specifically designed, for performing high-sensitive, selective and cost-effective detection of residual antibiotics in milk.
As a result it was studied a SPR-based sensing strategy which consists in the combination of resonant optical and magnetic properties in a single nanostructure, made of a superparamagnetic-core gold-shell nanoparticles exploiting a magnetic separation process combined to a plasmonic readout, and a plasmonic structure consisting of a thin metal film embedded in a refractive-index symmetrical layer architecture with a sinusoidal grating coupling supporting the propagation LRSPPs.
In order to obtain a portable sensor, integration of the sensor in microfluidic devices will be addressed.

Both of these themes are very interesting and up-to-date with strong industrial applications. The proposed strategies to face the problems are very valued and innovative and the chosen materials are suitable for fabrication of new sensors.

In chapter 1 the importance of the detection of zinc ions in biological system is described, followed by a discussion aimed to explain the reason why fluorescent sensors are favoured candidates for accomplishing sensing for this application. Chapter 2 resumes experimental materials and methods employed in this study and chapter 3 collects the obtained result data.
Chapter 4 introduces to the second project, which is related to the detection of antibiotics residues in milk, underlying the importance and the aim of this study. In chapter 5 experimental materials and methods employed are described. Finally, in chapter 6, overall conclusions are reported.

Chapter 1

Zinc fluorescent sensors: state of the art

1.1 The importance of Zn^{2+} in biological systems and its detection

Zinc is a transition metal of 12th group of periodic table, with an external configuration providing 10 electrons in the d orbital. It is a divalent cation with small dimensions with a radius of about 0.69 Å that favors high coordination numbers; in particular in presence of polydentate ligands with small donor atoms (like N and O) it can form complex with a coordination number higher than 4 but hardly higher than 6. Zn is the second most abundant transition metal following iron and occurs as divalent ion (Zn^{2+}) or in hydrolyzed form in human body, concentrated especially in nerve tissues. In general, zinc ions are well known to play different roles in biological processes, with a total amount of 2-3 g in an adult human body. The most important role for zinc is as structural cofactor in metalloproteins; recently zinc proteins with one or more zinc-stabilizer amino acids motifs have been studied and classified. For example, zinc-fingers are proteins that possess a zinc binding motif with high affinity toward zinc free ion involved in DNA binding and recognition, serving as model for the develop of highly affinitive and selective ionophores for fluorescent sensors. Zinc ions are also associated with the regulation of gene expression through metalloregulatory proteins and contained in hydrolytic enzymes in the active site, since zinc-bound water or hydroxide are excellent nucleophilic agents. Neurological roles of zinc have attracted much attention in recent years after postulating that synaptically released Zn^{2+} modulates the excitability of the brain through the accommodation of amino acid receptor. For this reason, a disorder of zinc metabolism is closely associated with many neurological diseases, such as Alzheimer's disease, amyotrophic lateral sclerosis, Guam ALS-Parkinsonism dementia, Parkinson's disease, hypoxia-ischemia and epilepsy [1].

Studies have also demonstrated much larger amounts of zinc in the pancreatic islets of Langerhans (β-cells), where insulin is stored within the secretory granules in the form of crystals containing hexamers of insulin and two or more zinc atoms (see figure 1.1a). When pancreatic cells are stimulated by elevate glucose concentration, insulin is coreleased with zinc through exocytosis, with spontaneous dissociation of the insulin-zinc complex as a result of exposure to extracellular pH (see figure 1.1 b). Then insulin monomers are formed as biologically active form of insulin and have a better diffusion in blood [2]. Abnormally low levels of zinc have been found in many diabetes

patients. In fact another major role for more loosely bound zinc is in physiological suppression of apoptosis; this may have important implications for some types of diabetes mellitus, in which there is progressive death of normally very-long living β-cells on a background of tissue zinc deficiency [3].

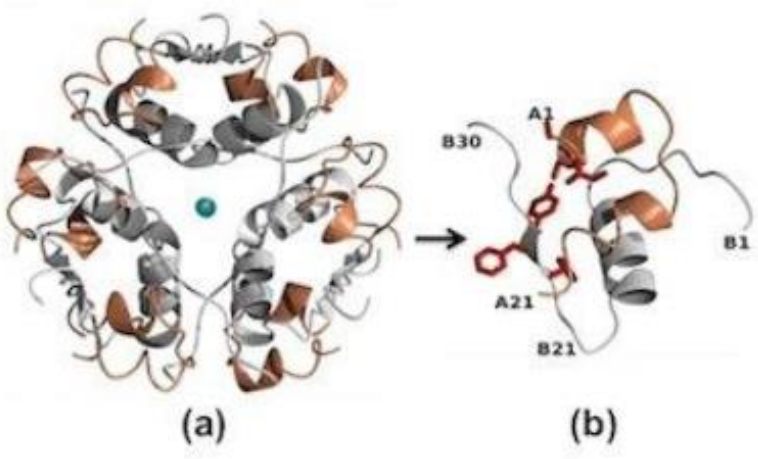

Fig. 1.1: (a) insulin hexamers coordinated with a central zinc ion (blue); (b) insulin active monomer derived from hexamers through exposure to extracellular pH.

Concentration of zinc involved in human body appears to be in the picomolar to nanomolar range; additionally these concentrations are not constant and varies with high speed in time and space [4]. For this reason it has become urgent to develop new zinc sensors to allow sensitive dynamic quantitative measurement in liquid medium. In this work some host-guest systems have been developed and tested to obtain a reversible dynamic fluorescent sensor with high selectivity for zinc ion. The conventional zinc imaging [5] provides the addition of hydrosulfuric acid that reacts with free zinc divalent ions to produce zinc sulfide; the following addition of 1,4-benzenediol and silver ions in presence of zinc sulfide bring to obtain metal silver as staining compound and 1,4-benzoquinone radical ion as by product. The reaction are showed in figure 1.2. This system is invasive, possesses poor selectivity and gives high risk of cell death.

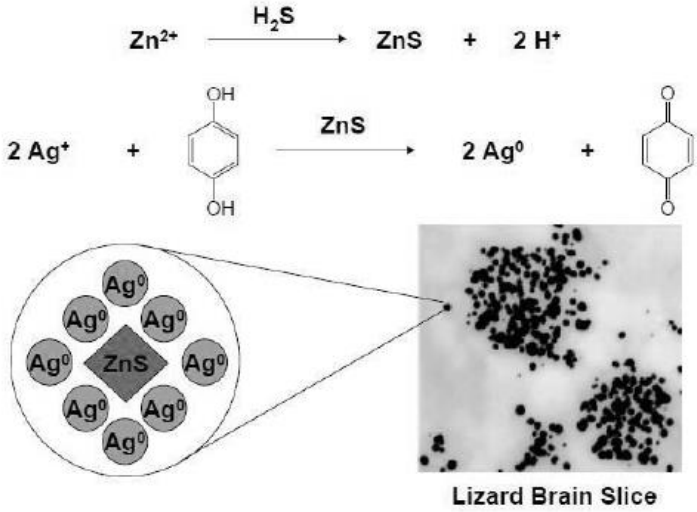

Fig. 1.2: conventional zinc ion imaging, using hydrosulfuric acid, silver ions and 1,4-benzenediol. Under, a zooming of a lizard brain slice from [5].

Later develop in zinc ions staining for biological application comprise the use of zinc selective fluorescent molecules (exposed in the following paragraph) as non-invasive sensing technique with a high sensitivity. An example of application is given from Kennedy et al. [6] for the detection of zinc secretion from single pancreatic β-cells using confocal microscopy. In this latter reference Zinquin is used as specific fluorogenic zinc ion indicator to spatially and temporally resolved measurement of Zn^{2+} efflux, incubating living cells in buffer containing a certain concentration of Zinquin. The high cost of this and other fluorophores suggests that under flow measurements are not an economic zinc staining technique. For this reason in this work are reported some attempts to synthesize an innovative optical based reversible sensors integrating a reduced quantity of fluorophore as guest molecule in an host hybrid organic-inorganic matrix, in order to reduce the operative cost and grantee the continuous measurement of both increase and decrease of free zinc ions concentration.

1.2 Zn^{2+} fluorescent sensors in liquid media

Owing to its $3d^{10}4s^0$ electronic configuration, spectroscopic or magnetic signals do not occur for Zn^{2+} contrary to what is observed for other biological transition metal ions such as Fe^{2+}, Mn^{2+}, Cu^{2+}. Therefore, the common analytic techniques such as UV-visible spectroscopy, nuclear magnetic resonance (NMR) and electron paramagnetic resonance (EPR) spectroscopy cannot be applied and fluorescence spectroscopy stands out as a method of choice.

Fluorescent sensors answer to a request of sensitive and non-invasive technique to accomplish real-time, local and reversible detection of specific analytes. They combine a metal chelating or binding moiety and at least one fluorophore which can absorb and emit light.

Upon binding to Zn^{2+}, the responsive moiety termed as zinc fluorescent probe forms a fluorescent complex, which can be used to stain and image free zinc ions; to function as a sensor, its electronic or molecular structure, has to be altered as a consequence of metal binding. A change in the intensity or wavelength of light absorbtion or emission occurs in the first case, while in the latter a variation of the distance or orientation between a pair of fluorophore that serve as donor-acceptor is expected.

A fluorescent Zn^{2+} sensor that operates in biological samples, should satisfy many requests: it must be selective for Zn over all other constituents, and provide Zn^{2+} detection with spatial and temporal resolution in a reversible way. The probe affinity, measured by its dissociation constant (Kd), should approach the median concentration of Zn^{2+} in the sample for monitoring its flux. Other advisable requirements include rapid and reversible Zn^{2+} coordination, excitation and emission wavelengths in the visible/near-IR/IR regions for single photon excitation, a bright ($\Phi \times \varepsilon$) signal, water-solubility, nontoxicity, and photostability [7].

Fluorescent sensors can be classified into two major groups according to the responsive moieties for the analytes [8]: chemosensors and biosensors. These sensors can also be divided into three classes based on their difference in ion sequestering pathways and fluorescence mechanism [9]:

1. Fluorogenic chelating agents: based on Chelation Enhancement of Fluorescence (CEF).

After absorbing energy, an electron may jump from the ground state to a higher energy excited state, whose lifetime defines the extent to which fluorescence.

The resultant excited state's lifetime determines the extent to which fluorescence accompanies the return of the electron to the ground state. If the excited state is sufficiently long-lived for some of its energy to be dissipated into molecular vibrational modes, the excited electron will drop to a lower excited state energy level before emitting a photon (of lower energy than that which it absorbed initially) and returning to the ground state. As a consequence, the light wavelength absorbed is of shorter wavelength than that emitted which represents the fluorescence of the molecule. Often the lifetime of the excited state molecule is shortened so that little if any dissipation of energy is possible before the excited electron falls back to the ground state, emitting a photon of the same wavelength as that absorbed. Under these circumstances the molecule is weakly fluorescent at best and its fluorescence is said to be 'quenched'. If Zn^{2+} binds to such a molecule and disables the process which quenches its fluorescence, the mol e cul e will s igna l the Zn^{2+} binding by fluorescing and thereby act as a sensor.

Among the fluorescent sensors based on this mechanism and used for this study are TSQ (6-methoxy-8-p-toluenesulphonamido-quinoline) and Zinquin, both quinolone based fluorophores.

The exposed mechanism is illustrated in fig. 1.3.

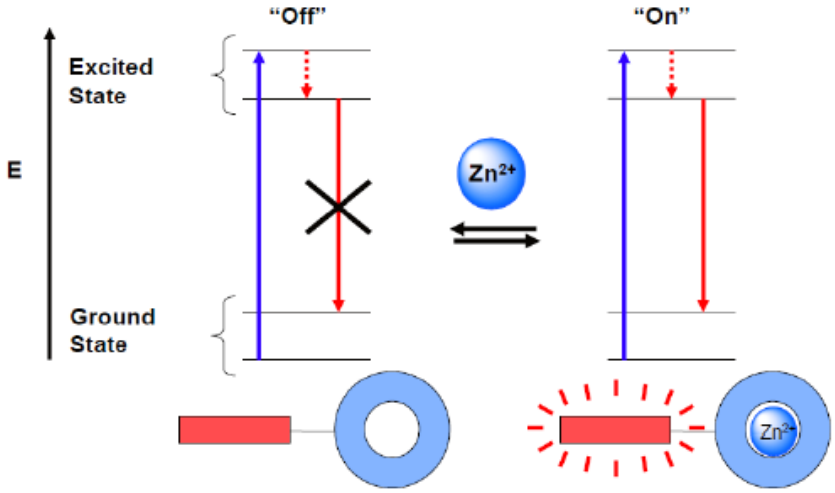

Fig. 1.3: CEF mechanism of fluorescence: quenching of fluorescence when zinc ion is absent, fluorescence with higher wavelength emission in presence of zinc-binding.

Examples of fluorescent sensors based on this mechanism are TSQ and Zinquin, both quinoline based fluorophores. 6-methoxy-8-p-toluenesulphonamido-quinoline, TSQ, is one of the first fluorescent probes developed for zinc ions sensing in 1987 and applied for its in vitro imaging. TSQ chemical structure is reported in fig. 1.4; it is a pH-indipendent, selective and non-toxic fluorescent sensor widely used to localize zinc pools in the central nervous system and to stain pancreatic islet cells rich in zinc. The complexation of TSQ with free zinc ions probably occurs not only in a stoichiometry of 2:1 TSQ/Zn^{2+}, but also in a 1:1 complex that may equilibrate with protein binding.

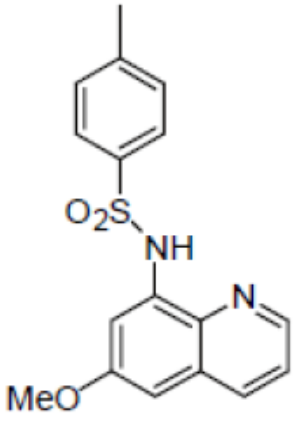

Fig. 1.4: TSQ chemical structure (6-methoxy-8-p-toluenesulphonamido-quinoline).

However, this probe suffers several limitations including poor water solubility and low membrane-permeability, which were then overcome with the synthesis of Zinquin probe by Zalewski et al. [10]. An ester group was incorporated at 6-position so that after the neutral lipophilic probe

permeates into the cell, the ester would be hydrolyzed to a carboxylate anionic form by intracellular esterase to stay within the cell [7]. Zinquin, whose chemical structure is reported in figure 1.6 in ester form (a) and acid form (b), allows to monitor loosely bound, labile intracellular zinc ions by fluorescence video image analysis or fluorimetric spectroscopy. Under physiological conditions (pH 7.2) the two forms of Zinquin (E and A) bind to Zn^{2+} to form 2:1 complexes with similar overall binding constants. Selectivity of Zinquin is demonstrated with the presence of other biologically relevant metal ions that do not affect the zinc-dependent fluorescence (as Ca^{2+}, Mg^{2+}, Cu^{2+}, $Fe^{2+}/^{3+}$, Mn^{2+},Co^{2+}, etc.), as demonstrated from results of fluorescence intensity reported in table 1.5. Additionally, fig. 1.6 shows zinc ions co-stored in pancreatic β-cells and its release by exocytosis with a consequent increase in fluorescence intensity due to the formation of a fluorescent complex composed of zinc ions and Zinquin acid with the exposed mechanism of complexation, after dissociation of insulin hexamers.

Metals[a]	Fluorescence Intensity (mean ± SD)
None	10.0 ± 0.1
Zn^{2+}	357.8 ± 30.9
Ca^{2+}	9.5 ± 1.8
Mg^{2+}	8.5 ± 0.7
Mn^{2+}	8.2 ± 0.3
Cd^{2+}	96.3 ± 10.8
Cu^{2+}	10.9 ± 0.6
Ni^{2+}	10.3 ± 1.3
Hg^{2+}	9.9 ± 1.5
Co^{2+}	9.8 ± 0.8
Ag^{+}	9.6 ± 1.0
Li^{+}	9.4 ± 3.6
Pb^{2+}	8.8 ± 1.2
Fe^{2+}	8.6 ± 0.5
Fe^{3+}	8.7 ± 0.4
Ba^{2+}	8.1 ± 0.3
Au^{2+}	8.0 ± 0.5

[a] Metal ions were added as salts to a final concentration of 1 μM to 2 ml of HBSS containing 1.25 μM Zinquin in cuvettes. Fluorescence was determined immediately. Figure indicates mean fluorescence in arbitrary units for samples in triplicate ± SD.

Table 1.5: mean fluorescence intensity for Zinquin in presence of different meta ions [3]; Cadmium ions give weakly enhanced fluorescence but this metal is not a normal constituent of biological tissues and environment because of its known high toxicity.

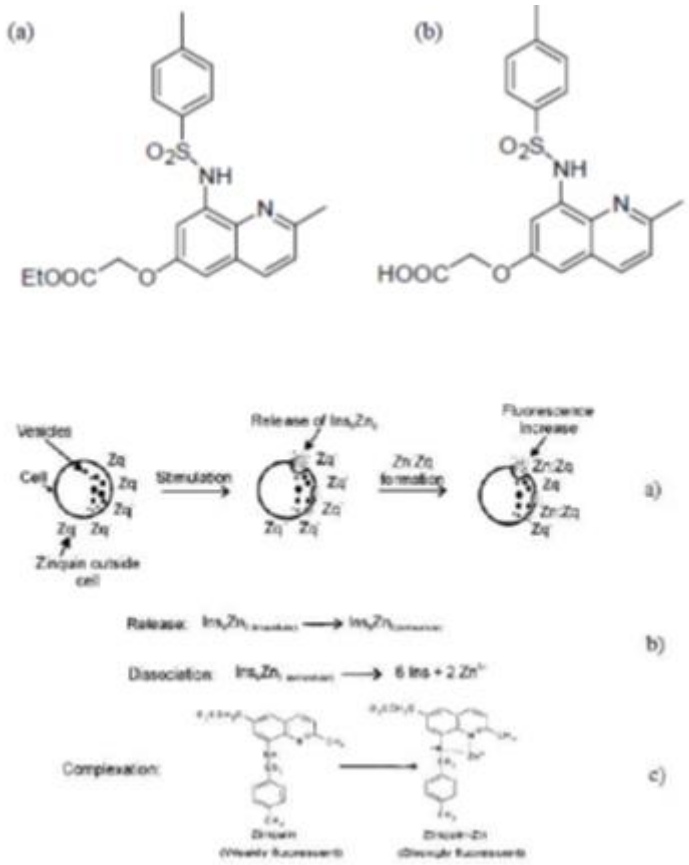

Fig. 1.6: release of insulin hexamers from pancreatic β-cells vesicles with consequent increasing of fluorescence (a) due to formation of Zn-Zinquin complex(c) and dissociation of the same hexamers in 6 insulin monomers and 2 zinc ions (b).

An important limitation of the quinoline-based sensor is the requirement of UV excitation, which may cause damage to living cells and bring artefacts to the dynamic activities of zinc(II) ions. Useful solutions consist in shifting the excitation wavelength toward visible region or developing sensors that can measure quantitatively zinc ions in flow and could be positioned far enough from cells.

2. Fluoroionophore: are molecules with separate fluorophore and ionophore linked with or without a spacer. According to the photo-induced process, they are further divided into systems based on a Photo-induced Electron Transfer (PET) or a Photo-induced Charge Transfer (PCT) [11].

-Photo-induced Electron Transfer (PET): in this type of sensors the metal ion receptor is an electron donor (often an amine or other nitrogen donor group) and the fluorophore acts as an electron acceptor. In the absence of Zn^{2+}, upon excitation by photons the electron of the Highest Occupied Molecular Orbital (HOMO) of the fluorophore is promoted to the local Lowest Unoccupied Molecular Orbital (LUMO). This leaves an electronic vacancy in the fluorophore HOMO, which is filled by transfer of an electron from the higher energy HOMO of the electron donor and causing

fluorescence quenching. Upon binding Zn^{2+}, the energy gap between these two HOMO orbitals is changed from positive to negative, so the quenching process does not occur. PET mechanism descripted above is illustrated in fig.1.7.

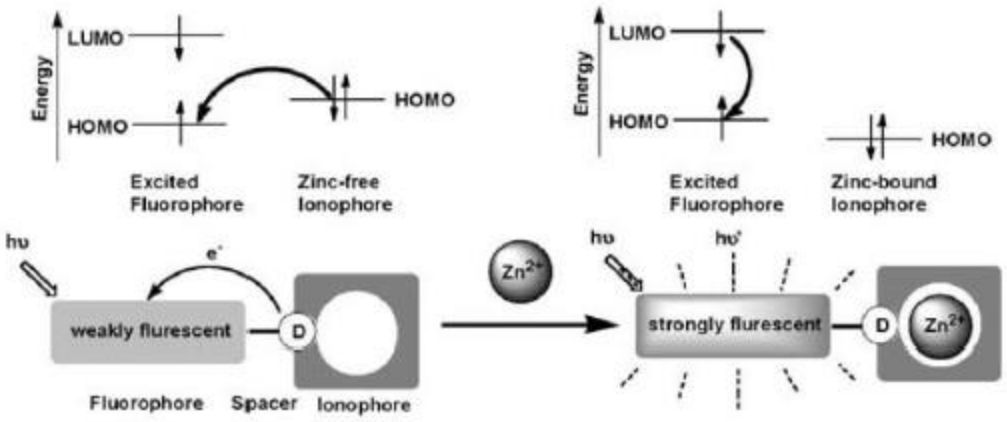

Fig. 1.7: operation of PET Zn2+-selective fluorescent sensors [9].

Examples of PET fluorescent sensors for zinc ions are Zinpyr family, ZnAF, FluoZin, RhodZin and anthracene derivatives having chelating moieties as Cage 2 [12] used in tested systems; some of their chemical structures are reported in fig. 1.8.

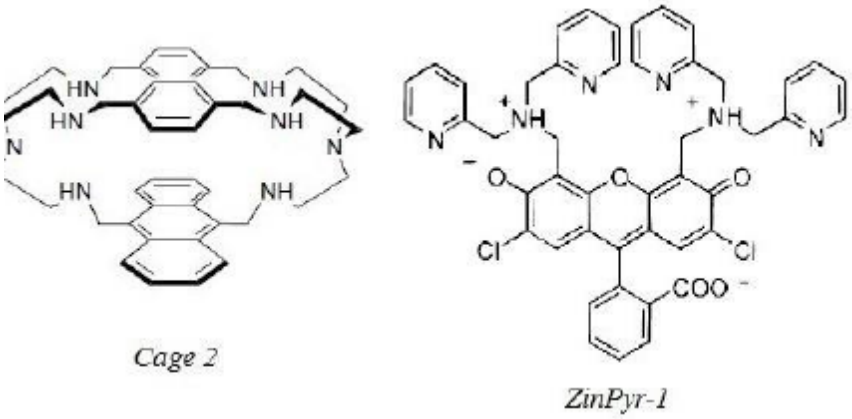

Fig. 1.8: some chemical structures of fluorophores cited above and used in this work as fluorescent Zn-ion selective molecules.

Lippard, Tsien et al. [13] synthesized ZinPyr-1 to solve problems of quinolinebased probes that give a difficult distinction between chelatable and free zinc ions due to the fact that these dyes can form mixed complexes, sensing also Zn^{2+} that is already partially coordinated. The resulting molecule of ZinPyr-1 is a membrane-permeable fluorophore containing dipicolylamine as Zn^{2+} chelator, with

highly zinc ions selective response with a maximum excitation wavelength of 515 nm in absence of Zn^{2+}, shifted to 507 nm with saturating zinc ions. ZinPyr-1 molecule undergoes protonation of electron donor amino groups in solution and a consequent deprotonation of the same group with zinc ions binding. ZinPyr-1 exhibits also a pH-dependent fluorescence, with maximal fluorescence at pH 5.5 and essentially no fluorescence for pH>12. The crystal structure of complex of ZinPyr-1 and Zn^{2+} with trigonal bipyramid geometry is reported in following fig. 1.9

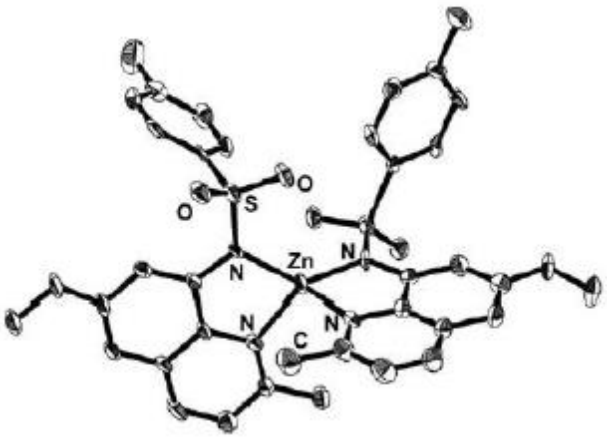

Fig. 1.9: crystal structure of complex ZinPyr-1 and Zn^{2+}.

ZinPyr-4, synthesized from Lippard et al. [14], is a membrane impermeable fluorescent probe which forms a 1:1 complex with Zn^{2+} with a dissociation constant in the sub-nanomolar range, two order of magnitude lower than that of ZinPyr-1 and enhanced affinity for bivalent zinc. ZinPyr-4 coordinates in aqueous solution to Zn^{2+} as a pentadentate ligand with a bound water. Fabbrizzi et al. [12] synthesized a cage composed of two tren compartments connected through spacers, in which one is represented from the strongly fluorescent 9,10-anthracenyl fragment. Zn^{2+} forms with cage 2 stable complexes with amine ligands and, being redox inactive and having filled 3d level, cannot be involved in quenching of cage fluorescence.

- Photo-induced Charge Transfer (PCT): in this sensors the fluorophore group is fluorescent and contains an electron donating group conjugated to an electron acceptor group such that internal charge transfer (ICT) from the donor to the acceptor occurs. When Zn^{2+} binds to the electron donor group, the light absorbance wavelength decreases (blue shift), as fluorescence wavelength does, because the energy gap between the HOMO and LUMO orbitals increases as a consequence of a decreased donation of electrons into the conjugated π system of the fluorophore. If Zn^{2+} binds to the electron acceptor group, the HOMO/LUMO energy gap will decrease as the electron withdrawing

character of the acceptor increases and the wavelength of both absorption and fluorescence will increase (red shift). This mechanism is illustrated in fig. 1.10.

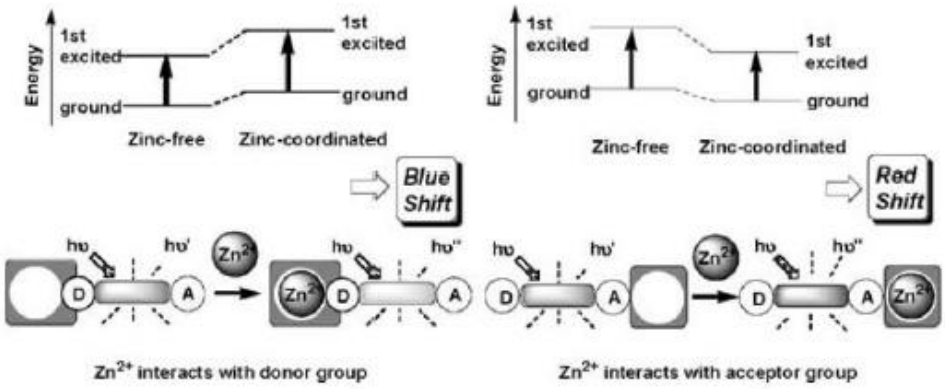

Fig. 1.10: PCT mechanism in fluorescent sensors for zinc ions.

Fluorescent probes that work using this mechanism are ZnAF-R1 and ZnAFR2 where the fluorescence of benzofuran-based fluorophores are not quenched by the amine group [15]. The four nitrogen atoms bind Zn^{2+} and a blue shift occurs for the absorption wavelength with a lesser shift for the fluorescence wavelength because the positive charge repulsion between the cation and nitrogen keep them apart. Between the two compounds, ZnAF-R2 is more soluble and fluorescent in aqueous solution and for this reason could be a better candidate for biological zinc ions detection. As a result, the most prominent features of PET and PCT sensors are the distinction between the fluorescence changes upon cation binding: fluorescence enhancement exhibited by PET, while obvious spectroscopic band shifts appear in PCT.

3. Fluorescence Resonance Energy Transfer (FRET): these sensors are based on dipolar long-range spatial interaction in which energy transfer between two adjacent fluorophores in the same molecule occurs. Excited by short wavelength light, the donor transfers energy to spatially adjacent acceptor through dipole-dipole interaction. The acceptor may be either a fluorophore or a quencher leading to two different sorts of CEF application: if the acceptor is a fluorophore, the fluorescent ligand should chelate the analyte to draw the donor-acceptor pair closer and thereby to allow stronger energy transfer. Whereas, if the acceptor is a quencher, the sensor is based on chelation-induced release of the fluorophore which then emits. An example of fluorophore based on FRET mechanism has been designed from Berg et al. [16]; it is a peptide probe based on zinc-finger consensus sequence. Zinc-fingers are proteins that possess a zinc binding amino acid motif with high affinity

toward zinc ions and this characteristic has been a model for the development of highly affinitive and selective ionophore for Zn^{2+} in fluorescent sensors. In peptide ligand developed from Berg et al., presented in fig. 1.11, two strong fluorescent fluorophores, lissamine (acceptor group) and fluorescein (donor group), and an amino acids motif are employed and allow to achieve picomolar level affinity for zinc ions. This visible-light-excitable biosensor exhibits two distinct emission bands at 521 and 596 nm. Upon zinc addition, the former band remains unchanged, whereas the latter gives a large fluorescence enhancement.

In the present study, the technique employs a probe molecule that selectively binds Zn^{2+} ions, determining either an enhanced emission or a quenching of fluorescence light. This mechanism allows real-time and in-situ sensing, even in the presence of living cells without damaging them (e.g. with UV radiation).

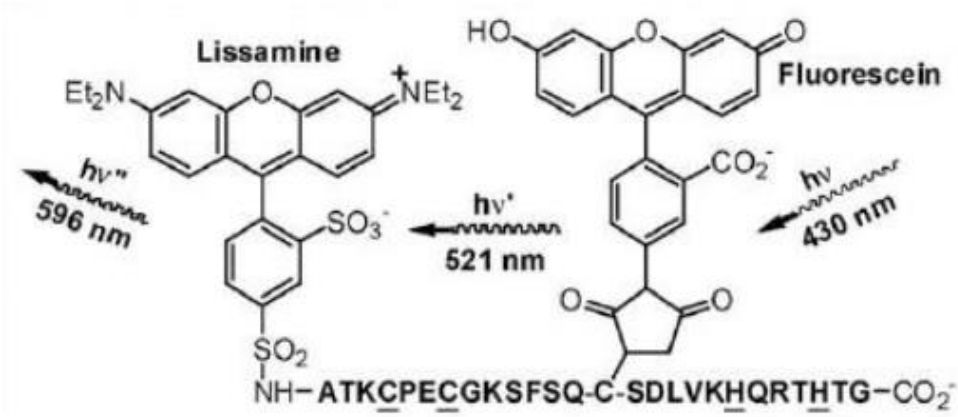

Fig.1.11: chemical structure of FRET sensor synthesized by Berg et al. [14].

A particular photophysical mechanism, that is not similar to all discussed above, is possessed by 3HF (3-Hydroxyflavone, also known as flavonol). 3HF is one of the simplest flavonoids with photophysical properties related to the Excited State Intra-molecular Proton Transfer (ESIPT) that occurs at its singlet excited state 1N*. This transfer leads to an excited tautomer 1T* of the molecule characterized by an emission wavelength in the range 500-560 nm whose precise position depends on the surrounding environment. Then the resulting ground-state tautomer T undergoes a non-radiative back proton transfer to give 3HF in its fundamental state indicated as N; a weaker broad emission could be also observed at 400-420 nm due to the radiative decay from the singlet excited state 1N*. Fig. 1.12 exposes this mechanism with respective chemical structures.

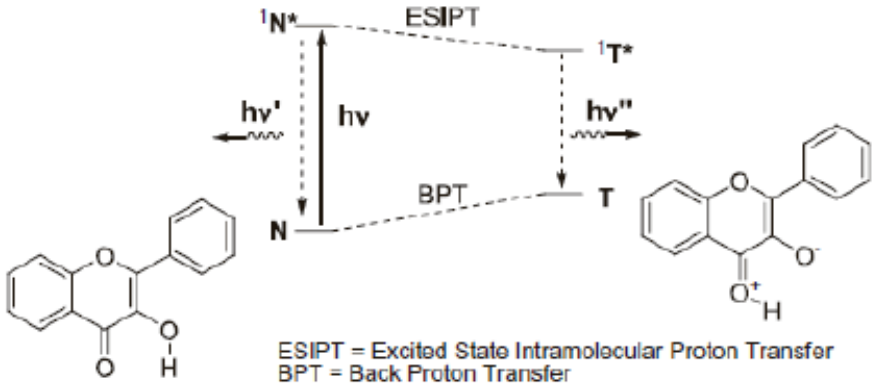

Fig. 1.12: ESIPT mechanism in 3HF molecule and chemical structures of tautomers and 3HF.

Studies revealed that 3HF molecule could be used as molecular fluorescent probe, especially because of its large Stokes' shift of about 180 nm, or to improve the sensitivity in the UV range of standard photodetectors. For this latter application, Mezzetti et al. have tested a wavelength shifting system encapsulating 3HF in SiO_2 matrices by post-doping of xerogel matrix [17]. Considering the influence of surrounding environment on 3HF emission properties it is useful to understand the nature of the interactions between dye and silica molecular cage; anyway, post-doping procedure should ensure that there is very little interaction between dopant molecules and residual organic solvents or ligands, ensuring also more stability for this systems than for ones obtained by direct sol-doping. Mezzetti et al. studies also emission of post-doped xerogels that leads to observe the absence of expected emission band at about 410 nm, characteristic of N* state, coherently with the interpretation that at the interior of the gel 3HF finds an apolar environment.

In the end, it is useful to remember that the perfect molecular fluorescent probe for any application does not exist, because every application and environment has its ideal condition and range in which analyte has to be considered. The concentration of interest is not the same in any application, and for this reason the appropriate fluorophore has to be chosen in order to reach the right sensitivity for a specific concentration range. In particular, to detect both concentration increases and concentration decreases, dissociation constant Kd of chosen selective sensor has to be near the median concentration of the analyte at physiological pH [7]. In this work, the main aim is to synthesize a new host-guest system by sol-gel synthesis doped with selective fluorophores for zinc ions, in order to research a selective dynamic reversible sensor for zinc ion in liquid medium, expecially in a proper buffer for pancreatic β-cells living.

Chapter 2

Experimental: materials and methods

2.1 The sol-gel process: general features

The sol-gel process allows to obtain homogeneous, high-purity inorganic oxide glasses at ambient temperatures in contrast with very high temperatures required in conventional approaches.

Even if it was known earlier, sol-gel chemistry has been widely investigated since the mid-1970's, when it was shown that it made it possible to produce a variety of inorganic networks that can be formed from metal alkoxide solutions. [1, 2].

In sol-gel processing the precursors consist of a metal or metalloid element surrounded by different reactive ligands. Among metal alkoxides, aluminates, titanates and zirconates are the most popular precursors thanks to their high reactivity towards water; Alkoxylanes, including tetramethoxysilane and tetraethoxysilane, are most widely used non metal alkoxides.

The reaction scheme of the sol-gel process, which consists of a series of hydrolysis and condensation reactons of an ankoxide, is reported in fig. 2.1.

Here, we are referring to alkoxysilanes but all the metal alkoxides react analogously. Hydrolysis is initiated by the addition of water to the silane solution under acidic, neutral, or basic conditions.

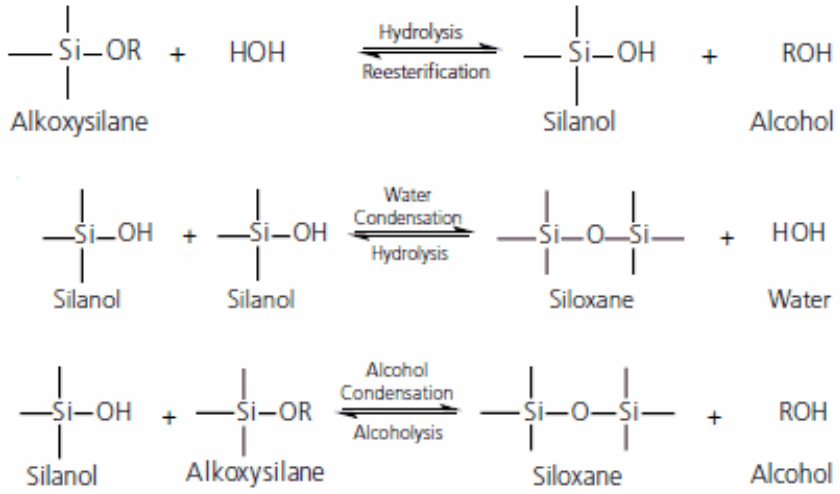

Fig. 2.1. Sol-gel reaction scheme

Hydrolysis and condensation reactions can be carried out without catalyst in the case of several metal alkoxides due to the extremely fast rate of reaction, whereas alkoxysilanes require the addition of either an acidic or basic catalyst as they react much more slowly.

Different theories have been proposed to provide an explanation about the mechanisms which drive the hydrolysis reaction under acidic conditions.

Studies conducted on TEOS, have revealed that under acidic conditions alkoxide groups are rapidly protonated in a first step, so that silicon is more electrophilic and thus more susceptible to attack by water.

Water molecule attacks from the rear and acquires a partial positive charge, reducing protonated alkoxide charge, making alcohol a better leaving group. The transition state decays by displacement of alcohol accompanied by inversion of the silicon tetrahedron [3], with mechanism presented in fig. 2.2.

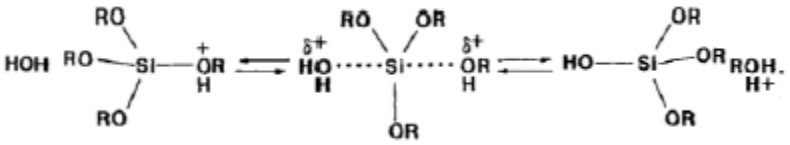

Fig. 2.2. Hydrolysis mechanism in presence of acid catalyst.

Another hypothesis proposed by Timms [4] suggests that protonation of an alkoxide group occurs, followed by a slower step in which a siliconium ion (≡Si+) is formed by the removal of alcohol, shown in fig. 2.3. Water then reacts with the siliconium ion to form a silanol group with regeneration of proton.

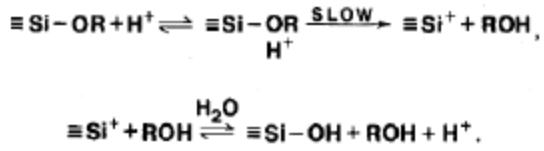

Fig. 2.3: acid-catalyzed hydrolysis mechanism from Timms' theory.

Concerning the base-catalyzed hydrolysis, water dissociates to produce nucleophilic hydroxyl anions that attack the silicon atom displacing OR- with inversion of the silicon tetrahedron, as can be seen in fig. 2.4.

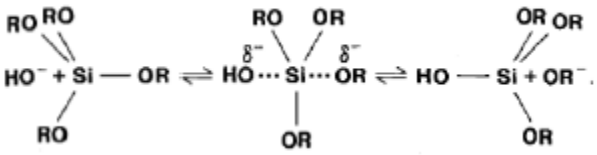

Fig. 2.4: base-catalyzed hydrolysis mechanism.

Acidic and basic conditions are both affected by steric and inductive effects.

The steric effect causes the decrease of hydrolysis rate as a function of the complexity and of the degree of branching alkoxide groups. The H_2O:Si ratio values influence as well the hydrolysis rate; in particular, an increase of this ratio results in a reduction of the number of unhydrolyzed monomers which remain after a reaction time of few hours.

In the condensation step hydrolyzed monomers react each other (see fig. 2.5) to form silicate polymers and gels in a liquid medium, generating water and alcohol as products. The condensation step may start before the end of hydrolysis step, as it happens in case of acidic catalysis, leading to a linear polymeric structure in the final gel product. Under basic conditions a 3D condensed structure with high branched and less linear chains is formed, ideal to obtain nanoparticles as in the Stöber process [5]. Depolymerization reactions could affect the condensation rate, but in alcoholic solution, especially at low pH, the depolymerization rate is very low.

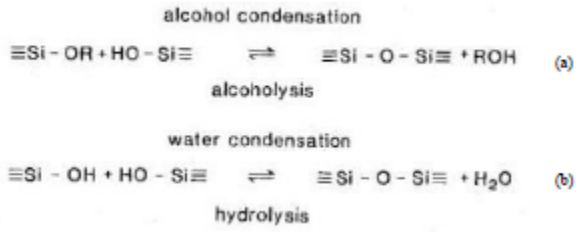

Fig. 2.5: alcohol condensation (a) and water condensation (b) reactions for silane monomers.

At a certain stage of of the condensation reaction, a sol is obtained, which is a dispersion of colloidal particles in a liquid due to condensation reactions between hydrolyzed silane groups. When formed particles bound together to get a network, the sol-gel transition occurs and a gel is obtained, that is an interconnected rigid network with pores of submicrometer dimensions and polymeric chains. This transition is accompanied by a sharp increase in viscosity due to the freezing in a particular polymer structure. The gel can elastically support a stress, defining in this way its own gelation point or gelation time. All subsequent stages of processing depend on the initial

structure of the wet gel formed in the reaction bath during gelation. With time, change of temperature, solvent and pH conditions the formed structure can change appreciably.

Casting: since the sol is a low-viscosity liquid (before gelation point in most cases), it can be cast into a mold or used to coat substrates and form thin films. A common process used to obtain thin films is spin coating, also used in experiments conducted in this work. Spin coating process is composed of four stages: deposition, spin-up, spinoff and evaporation (see fig. 2.6). In the first stage an excess of liquid solution is dispensed on the surface of chosen substrate; in spin-up stage the liquid flows radially outward due to centripetal forces; in spin-off, excess of liquid flows to the borders of the sample and leaves it as droplets; in the evaporation stage, that may overlap spin-up and spin-off stages, evaporation of template takeovers. During all these stages, film thinning and increase of resistance to flow accompany a rising of viscosity that in case of sol-gel process bring to gelation point. In this way, it can be possible to obtain a thin film composed of gel, that in successive times can be aged or if necessary dried. Often thin films produced with this technique have a flatter area in the center of the substrate and a higher and uneven thickness on edges.

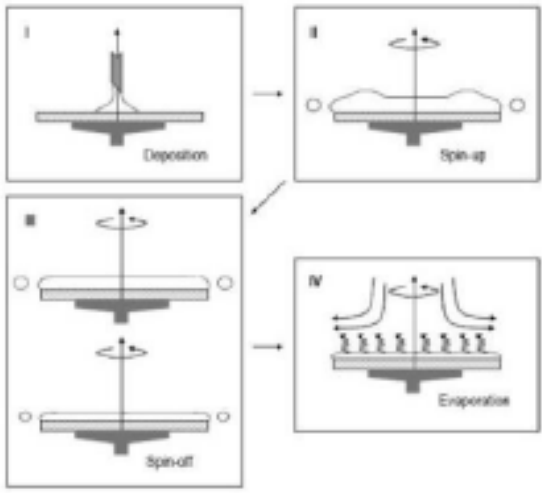

Figure 2.6: spin coating stages: I. Deposition; II: Spin-up; III: Spin-off; IV: Evaporation.

4. Aging: this optional step, called also syneresis, provides to maintain the gel in its liquid, leading to a continuous change of structure and properties. During aging, polycondensation continues increasing connectivity of the network with localized solution and reprecipitation of the gel due to large concentration of labile hydroxyl groups. These changes continue also for months at room temperature and they are affected from concentration and pH of the solution. New bridging bonds created in this step lead to an increase of stiffness and strength of the network, with a shrinkage (from which the name syneresis) as consequence of expulsion of liquid from pores. This may be

accompanied by a reduction in pores' size. This step allow to obtain a more homogeneous condensed network with less hydrolyzed labile silane that could react with other compounds.

5. Drying: this step is useful to control gel-structure modification until a dried solid material is obtained. During this stage the remaining liquid is removed from the interconnected pore network using spontaneous evaporation of solvent at room temperature or by heating of the gel. Large capillary stresses can develop during drying when the pores are small (e.g., <20 nm) that could cause catastrophically crack of gel. Cracks and ruptures of gel can be avoided by control of drying conditions and pores size, also with minimal shrinkage if dried by hypercritical evaporation. If drying occurs by heating at high temperature it can be called densification, with at most elimination of pores and density equivalent to bulk material.

2.2 Porous sol-gel systems

In sol-gel process, porosity develops when, due to additional crosslinking or neck formation, the gel network becomes sufficiently strengthened to resist the compressive forces of surface tension. Porosity can be classified into three different dimensional ranges: micropores (with diameter < 2 nm), mesopores (2-50 nm), macropores (> 50 nm). In general, sol-gel synthesis leads to a material with a network composed of solid skeletal and interconnected porous phase, whose structure can be modulated tuning conditions and times of each step described above. In host-guest systems pore size is fundamental to develop a great integration of guest molecules in host matrix; for this reason is important to understand how porosity can develop in sol-gel systems and how it evolve during synthesis and consequent drying. To maintain gel porosity also in bulk dried material is useful to dry the gel by hypercritical evaporation, leading to aerogels. The removal of a solvent above its critical point occurs with no capillary pressure because there are no liquid-vapor interfaces, resulting in a reduced driving force for shrinkage. If the gel is dried at room temperature or in general without hypercritical evaporation the product obtained is called xerogel. These materials are highfree-energy compared to their dense oxide counterparts, with surface areas in the range from 100 to 1000 m^2/g. Dried xerogel structure will be a contracted and distorted version of the structure originally formed in solution. The relationship between structure of the gel and xerogel has been studied in function of grade of branching in gel structure. The most weakly branched systems, generally formed with low condensation rate, tend to be overlapped at the gel point. The structure in this case can freely interpenetrate and shrink in response to solvent removal, while the condensation

rate remains low. Possible presence of tiny pores may bring a further compaction in the structure due to capillary forces developed in the final stage of drying.

More highly branched structures are prevented from interpenetrating and collapse due to strong intercluster and steric screening effects. When solvent is removed individual clusters undergo shrinkage and rearrangement to achieve higher coordination numbers. Shrinkage is lower compared to weakly branched structures, and it stops at an earlier stage of drying due to the stiffness of the packed clusters. This results in larger pores, so that the maximum capillary pressure is reduced compared to previous structure. Resulting xerogel is characterized by a globular structure similar to a compacted version of previous gel structure with porosity that often exists on two length of scales: microporosity within clusters and mesoporosity between clusters. This results also in lower capillary pressure and lower risk of cracking during gel drying.

For all categories of gels, aging prior to solvent extraction can alter the porosity of the dried product. For example, aging a gel under conditions with appreciable solubility of its skeletal phase allows reorganization of the structure by dissolution and reprecipitation. Often this has the effect of strengthening the gel so that it stops shrinking earlier in the drying process, resulting in a larger pore volume. In this work xerogels in form of thin films, bulk materials or powders have been synthesized for different applications, integrating in the interconnected porosity of different molecules with particular optical properties. For thin films obtained via spin-coating the overlap of deposition and drying stages establishes a competition between evaporation and continuous condensation reactions, accompanied by a stiffening of the film with a higher resistance to compaction. In this case the porosity of the film depends on relative rates of condensation and evaporation.

2.3 Bridged silsesquioxanes

Bridged polysilsesquioxanes are a class of hybrid organic−inorganic materials prepared by sol−gel polymerization of monomers with a variable organic fragment and two or more trialkoxysilyl groups.

The result is an hybrid material with organic and inorganic domains dispersed at the molecular level. Some examples of monomers are reported in following fig. 3.8. This intimate association of organic and inorganic phase coupled with the variability of the organic component permits engineering of both chemical and physical properties of the material, resulting in a true molecular composite. Reduction in domain size accesses the molecular level by incorporating the polymerizable inorganic group and an organic constituent in the same molecule. Therefore it is possible to obtain an homogeneous amorphous material via sol-gel chemistry, with a completely

uniform distribution of organic groups and inorganic oxides at the molecular level [6]. The organic group remains an integral component of the material network providing an opportunity to modulate bulk properties such as porosity, thermal stability, refractive index, optical clarity, chemical resistance, hydrophobicity and dielectric constant [7]. Bridged PSQ polymerization is a sol-gel process with a single step, which runs in the presence of templates to produce materials with uniform nanosized pores in the final products. It is generally acid or base catalyzed often with hydrochloric acid or ammonium hydroxide respectively. The resulting degree of condensation is directly related to the number of residual silanol and alkoxide groups at silicon, that also contributes to the overall polarity of the material. This synthesis allows rapid formation of polymers that irreversibly form gels also in few minutes, with the organic group that is an integral part of the network architecture. Upon drying, formed materials afford amorphous xerogels or aerogels (see fig. 2.7) whose surface area can be tailored through selection of the organic spacer. The same xerogels are brittle glassy materials that do not expand or dissolve in either water or organic solvents.

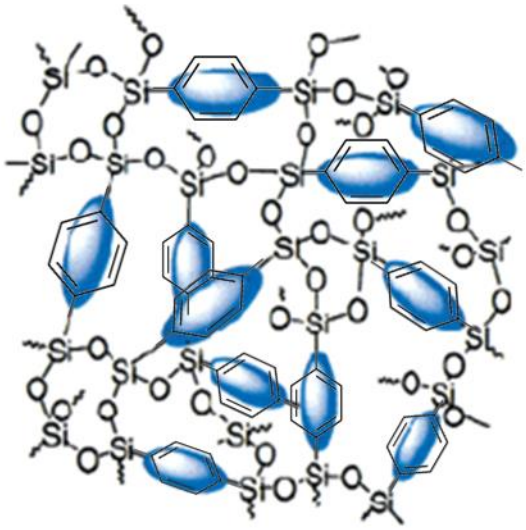

Fig. 2.7: amorphous gel network from bridged PSQ sol-gel polymerization. [8]

Porosity is a key property of materials used in this work, in order to improve integration between guest fluorophore molecules and host bridged PSQ matrix. The bridging group provides an opportunity to vary the size, shape, geometry and functionality of a molecular building block in order to investigate how bulk structural properties are affected. Important factors contributing to the porosity in these bridged PSQ materials include the compliance of the network, that is a function of the degree of condensation at the silicon, and the flexibility of the bridging group. It has to be considered also that sol-gel process has a high sensitivity to factors such as pH, catalyst,

temperature, solvent and aging time, factors that must be carefully controlled to permit a definite and reproducible effect of the bridging group on the xerogel structural properties. Studies on base-catalyzed arylene and ethenylene bridged polysilsesquioxanes by Shea et al.[9-14] observed in these materials a high surface area contains large contributions form micropores with mean pore diameter < 20 Å; alkylene bridged PSQ with bridging groups up to 10 carbons in length are in the form of mesoporous xerogels with a mean pore diameter included between 20 Å and 500 Å[15,16]. From these results, the mean pore diameter is shown to be approximately proportional to the length of organic bridging group. Another useful property of these hybrid materials is their excellent thermal stability in inert atmospheres and in air, also up to 500°C for phenylene bridged polysilsesquioxanes. This is very useful in case of manufacturing processes in which boiling water or in general high temperatures are involved, maintaining stability and original structure. Applications of bridged PSQ materials comprises different fields; for example bridged PSQ coatings can also be used as protective layers for metals, microelectronic applications (e.g. photoresist for lithography[17-19]). Incorporating dyes in sol-gel bridged PSQ matrix is a good strategy to produce waveguides [20], lasers, sensors [21,22], LED and nonlinear optical materials. The use of dye molecules as bridging groups leads to high loading of chromophores and no leaching or phase separation.

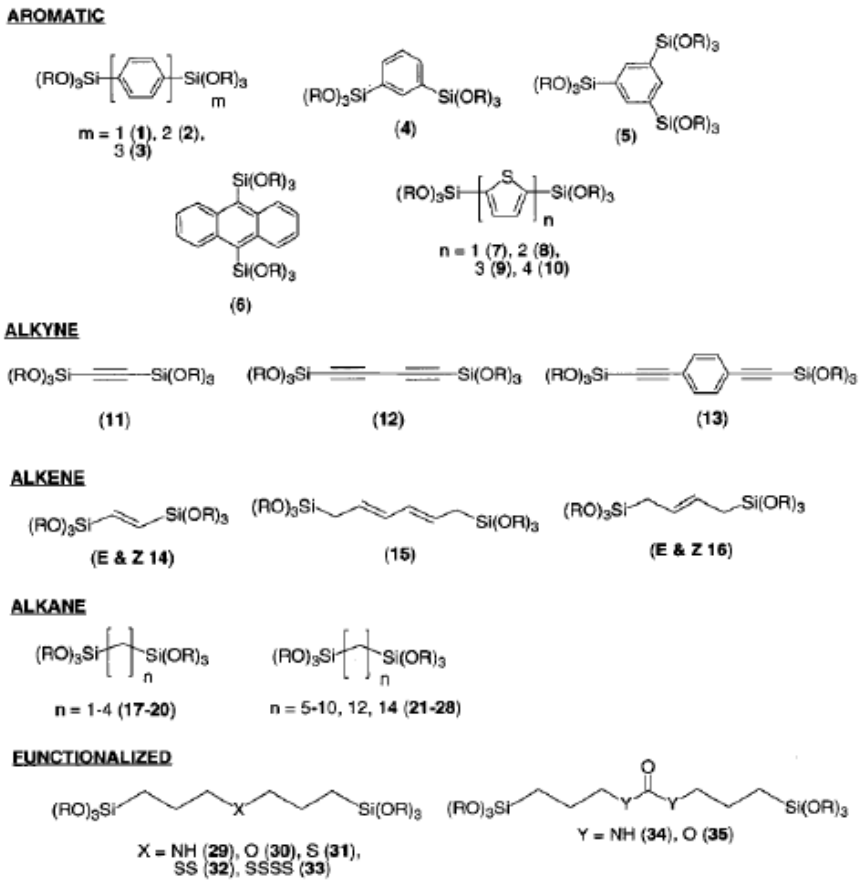

Fig. 2.8: examples of bridged PSQ monomers with different organic bridging group; (1)-(10) aromatic organic group; (11)-(28) alkyl bridged; functionalized groups as amine (29), ether (30), sulfides (31)-(33), urea (34) and carbonate (35).

The first developed host-guest systems consisted of a hybrid organic-inorganic material, synthesized starting from bridged silsesquioxane precursors (Fig.2.9) presenting different organic fragments, selected to obtain suitable properties to host fluorescent molecules. All matrices were obtained via a sol-gel method and functionalized by sol-doping; thin film depositions were achieved through spin coating. The most promising results were obtained employing phenyl-bridged polysilsesquioxanes (ph-PSQ) and Zinpyr-1 (ZP1) as fluorophore.

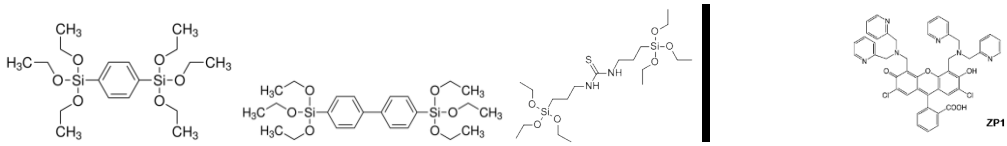

Fig. 2.9 Examples of employed bridged monomers; from left to right: 1,4-Bis(triethoxysilyl)benzene; 4,4′-Bis(triethoxysilyl)-1,1′-biphenyl; propylthiourea and the ZP1 fluorophore.

A solution of 1,4- bis(triethoxysilyl)benzene, ethanol (EtOH) and bi-distilled water was mixed in a monomer/H_2O = 1/6 molar ratio, using hydrochloric acid (HCl) 1 M as catalyst. The Si–C bonds linking two ethoxysilanes to the bridging benzene ring are hydrolytically stable. As hydrolysis and condensation progress, a three dimensional SiOx network, incorporating benzene rings as network formers, grows and the solution becomes more viscous. Before spinning, the obtained sol and ZP1 fluoprophore were mixed together. The films were then deposited by spin coating on the substrates, tuning the solution concentration in EtOH and/or the spin coating speed in order to obtain, after a thermal treatment at 80 ◦C for 30 min, a thickness of about 200 nm. A postdeposition bake was performed to promote solvent evaporation and to reach a stable cross-linking degree.

2.4 Mesoporous hybrid organic-inorganic SiO_2

Later, micro/nano-structured sinusoidal films made of mesoporous hybrid organic-inorganic SiO_2 doped with a fluorophore were synthesized. Hierarchical structures were obtained by the combination of top-down and bottom-up fabrication techniques. Mesoporous hybrid organic-inorganic films were synthesized through sol-gel chemistry. Tetraethylortosilicate (TEOS) was used as SiO_2 precursor, ZP1 was used as fluorophore and hydrochloric acid (HCl) as catalyzer. Cetyltrimethylammonium bromide (CTAB) was used as a mesoporous template (5 wt%). Films were deposited on the substrates by spin-coating. Soft-lithography was employed to induce the formation of a SiO_2 sinusoidal grating, while surfactants self-assembling were exploited to induce the formation of periodically ordered mesopores within the SiO_2 structure after a thermal extraction step.

Sinusoidal gratings were fabricated through soft lithographic techniques, starting from sinusoidal patterns, realized by LIL on Photoresist films deposited on silicon. The fabrication process consists in the realization of a negative replica made of polydimethylsiloxane (PDMS) of the nanostructured masters, and in the pattern transfer by soft NIL on films coating fused silica slabs or silicon wafers. A metal layer was evaporated on the nanostructured films, and selective probes were covalently linked to the metal, as a sensitive interface.

PDMS preparation was done using the Sylgard 184 Silicone Elastomer Kit (Dow Corning), which comes in two parts: a prepolymer and a curing agent. A mixture of the two components was prepared in 1:10, curing agent to prepolymer, weight ratio and outgassed inside a desiccator connected to a vacuum pump for about 1 hour. Then, the PDMS mixture was poured on the nanostructured masters, and thermally cured at 70° C in an oven for about 1 hour to promote polymerization, before peeling the elastomeric replica off the masters.

The presence of surface nanostructures on films allowed to increase the specific detection area, compared to flat films. The film thickness, around 400 nm, was determined by spectroscopic ellipsometry.

2.5 Characterization techniques.

UV-visible spectroscopy: Optical absorbance spectra were recorded by Jasco V-570 or Jasco V-650 spectrometers in the range 200-1500 nm or 200-900 nm respectively. For spectrum of liquid samples, a quartz cuvette has been used containing 3 ml of analyte.

FT-IR spectroscopy: Infrared absorption spectra were recorded in the range 4000–400 cm^{-1} by 620 JASCO Fourier Transfer InfraRed spectrometer with a resolution of 4 cm^{-1} averaging over 64 scans. These parameters have been used or thin films samples deposited on silicon wafer substrates.
Ellipsometric measurements: Variable angle spectroscopic ellipsometer J. A. Woollam VVASE was used to obtain Ψ and Δ values and total normal-incidence transmittance for different incidence angles (60°-65°-70° for fused silica substrates and 65°-70°-75° for silicon wafer substrates) in 300-1500 nm range of wavelength. All measures were with dynamic averaging enabled and comprised 20 revs/mean. Optical constants n and k and films' thicknesses have been fitted on experimental results using WVASE32 software and Cauchy model.

The fabricated sinusoidal patterns were imaged through an AFM (NT MDT) in non-contact mode.
The peak-to-valley height of the profiles was estimated from the Abbot curve as the height variation between the values corresponding to the 3% and 97% of the bearing area. The period was calculated from the position of the peak in the Fourier spectrum of the grating profile obtained by averaging over the horizontal scanned lines in an AFM image.

CV and EIS mesurements were carried out with Metrohm AUTOLAB potentiostat/galvanostat PGSTAT302N managed by software Nova 1.6. Reference electrode and counter electrode used were respectively saturated calomel electrode (SCE) and Pt electrode. Supporting electrolyte used was PBS 1X (pH=7.4) and redox probe used was 1 mM potassium hexacyanoferrate.

TEM, DLS, XRD analyses were carried out by the group of Prof. Fayna Mammeri in Paris.

2.6 Sensing techniques: confocal microscopy, fluorescence microscopy

First sensing tests were performed by confocal microscope analysis: all samples were excited by femtoseconds pulsed laser at 380 nm of wavelength; the maximum power measured after filters was36 mW and power applied for measures was 1.3 or 8 mW. The excited beam was reflected from a dichroic filter with λ_{cut} of 490 nm and then focused on the sample with a 20X microscope objective. The sample emission was focused on confocal opening having a diameter of 100 μm and then revealed by the detector for wavelengths over 510 nm. Collected pictures had a resolution of 8 or 12 bit and the resulting fluorescence values were mediated among 3 or 4 scans for every sample.

Later spectrofluorimetry techniques was considered for sensing tests on the samples. Emission spectra were recorded in focused ranges of wavelength for every case by Jasco FP-6300 with excitation and emission bandwidth of 5 nm, data pitch 1 nm and scanning speed of 200 nm/min. In order to exclude reflected radiation from resulting intensity detected, films were positioned in the cuvette containing the medium tilted of about 30°.

Chapter 3

Results and discussion

The most promising developed host-guest systems, here reported, are the result of a deep investigation based on several considerations, including the compatibility of the fluorophore with the matrix and the immobilization technique, the minimization of leaching, support matrix features such as high permeability and porosity to guarantee accessibility and interaction of the analyte with the fluorescent probe.

Fluorescent probes have been entrapped in suitable matrices synthesized via sol-gel method; the versatility of the process facilitated tailoring of the physicochemical film properties (e.g porosity) to optimize sensor performances; precursor type, nature of catalyst, ageing time, ageing temperature, dry time and dry temperature are a few examples of parameters on which depend final microstructure and properties of the sensor film.

The first tested fluorescent probe was TSQ.

TSQ, among other aryl sulfonamides of 8-aminoquinoline is one of the most widely applied membrane permeant probes for cellular zinc.

This fluorophore was synthesized and silane functionalized, therefore allowing to directly link it to a silicon alkoxide, thanks to a collaboration with the group of Prof. F. Mancin (department of Chemistry of the University of Padua). A scheme of the followed synthesis procedure is shown below (Fig. 3.1).

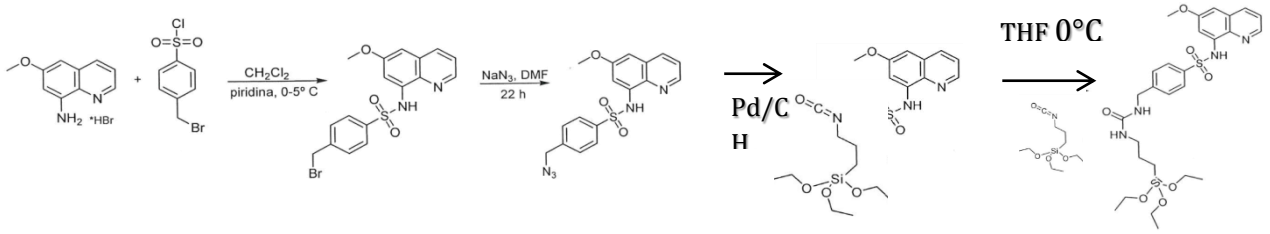

Fig.3.1 Scheme of the silane-functionalized TSQ synthesis procedure.

This modification in TSQ chemical structure allowed to obtain a thin film, by simply spin-coating this molecule (3000 rpm for 30 s). Sensing effectiveness and reversibility of the obtained thin film

was analyzed by confocal microscope with an excitation source at 380 nm and revealing fluorescence emission at wavelength higher than 510 nm.

The first measurement was set to know base fluorescence of the TSQ not bound to zinc, giving an average fluorescence of 25 (fig. 3.2 a); after immersion of the film for 10 minutes in an aqueous solution of zinc acetate at a concentration of 100 nM, the fluorescence almost tripled to a final average value of 77 (fig. 3.2 b). A decrease of the fluorescence signal was not observed after washing the sample in a buffer solution for 10 minute (average value of 71), therefore indicating that the fluorophore was not reversible at the desired operative dynamic conditions.

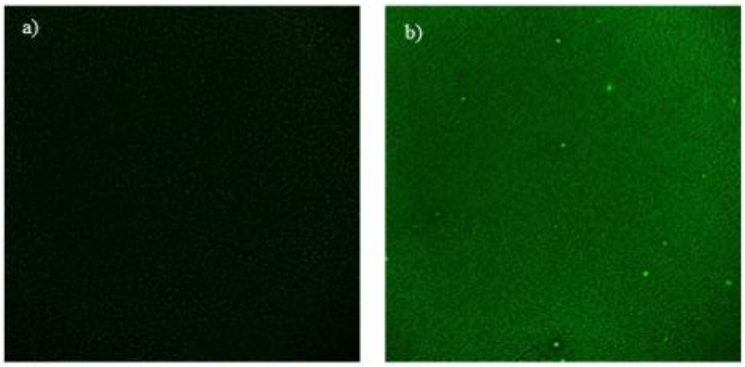

Fig. 3.2: a) confocal microscope's image of base fluorescence of silane-functionalized TSQ and b) fluorescence signlal after immersion for 10 minutes in aqueous zinc acetate solution 100 nM.

Although immobilization of the fluorohore was possible, as it was properly chemically modified to allow a better integration in hybrid matrices and the registered signal to noise ratio of the performed measurements was high, TSQ molecule was not adapt for our application due to its irreversibility at the requested operative conditions.
For this reason another fluorescent molecule was then considered.

Zinquin is an intracellular fluorescent probe for cellular Zn^{2+} status in the nanomolar range employed in this study. It was entrapped in thiourea bridged-PSQ matrix, which was optimized to avoid host-guest interactions. To reach an high degree of condensation with minimized residual unreacted Si-OH and alkoxide groups, FT-IR spectroscopy analyses were conducted on the films therefore allowing to compare different catalysis conditions.
Three different synthesis procedure were adopted:
1. Thiourea in acidic conditions was synthesized in presence of HCl. The obtained sol was deposited via spin-coating on fused silica and silicon wafer substrates at a speed of 3000 rpm for 30

s, after dilution to a final concentration of 50 g/l by adding of ethanol to reduce sol viscosity and in order to reach a better processability. A lower concentration allow in this case a higher hydrolysis rate and a better condensation of hydrolyzed groups.

In 1 ml of sol, reagents volumes used were: 0.762 ml of pure ethanol; 0.193 ml of bis(triethoxysilylpropyl)thiourea; 0.028 ml of bidistilled water; 0.017 ml of HCl 0,1 N.

2. Thiourea in basic conditions was synthesized by introducing tetrabutylammonium fluoride (TBAF) as basic catalyst and tetrahydrofuran (THF) as homogenizing agent. A first hydrolysis step consisted in mechanical mixing of THF, thiourea-bridged monomer (reported in fig. 3.3) and bidistilled water for 15 minutes. Then TBAF dissolved in THF is added and Then TBAF dissolved in THF is added and let be mechanical mixed for additional 15 minutes to allow the progress of the chemical reaction. Precursor, homogenizing agent and catalyst were added in molar ratios 1 : 3 : 0.01; for an overall final volume of 1 ml of sol 0.324 ml of THF, 0.154 ml of bis(triethoxysilylpropyl)thiourea, 0.018 ml of bidistilled water and 0.0009 g of TBAF solved in 0.503 ml of THF were used.

Concentration of monomer in the sol was 40 g/l; however its further dilution (20 g/l), reached by adding 1.000 ml of THF, was necessary in order to reduce viscosity and therefore getting better quality and uniformity of the thin films. Film deposition was achieved via spin-coating on fused silica and silicon wafer substrates at a speed of 3000 rpm for 30 s.

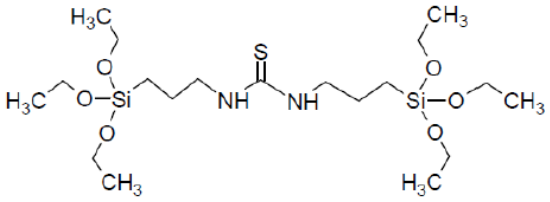

Fig. 3.3 : Bis(triethoxysilylpropyl)thiourea monomer

3. Thiourea in acidic-basic conditions was synthesized following a double step catalyst procedure, which implied the inversion of pH from an acid range to a basic one; this strategy allowed to increase the hydrolysis rate in the first acidic step in order to reduce unreacted alkoxide groups, and to get an higher condensation rate in the second basic step, leading to an larger number of condensated silanol groups.

The result was a saturated network, with fewer unreacted alkoxide groups and an higher stability of the material. The first hydrolysis step consists in the addition of pure ethanol as homogenizing agent, thiourea-bridged monomer and bidistilled water, mechanical mixed for 15 minutes.

Then with the addition of HCl 0.1 N the acidic catalysis step starts, lasting 30 minutes. Pyridine is added before the addition of TBAF dissolved in ethanol to decrease the pH at the end of the first catalysis step, so avoiding an abrupt inversion of the pH. For a total volume of 1 ml of sol 0.452 ml of pure ethanol, 0.115 ml of bis(triethoxysilylpropyl)thiourea, 0.017 ml of bidistilled water; 0.010 ml of HCl 0.1 N, 0.010 ml of pyridine and 0.0007 g of TBAF dissolved in 0.396 ml of pure ethanol were used.

As done in the other two previous cases, thin films were deposited on fused silica and silicon wafer substrate at a speed of 3000 rpm for 30.

FT-IR analysis of all the synthesized matrices were carried out in order to identify the best condition for an high condensation degree and for a stable material. The obtained spectra are reported in fig. 3.4, while information about the most relevant peaks are resumed in table 3.5.

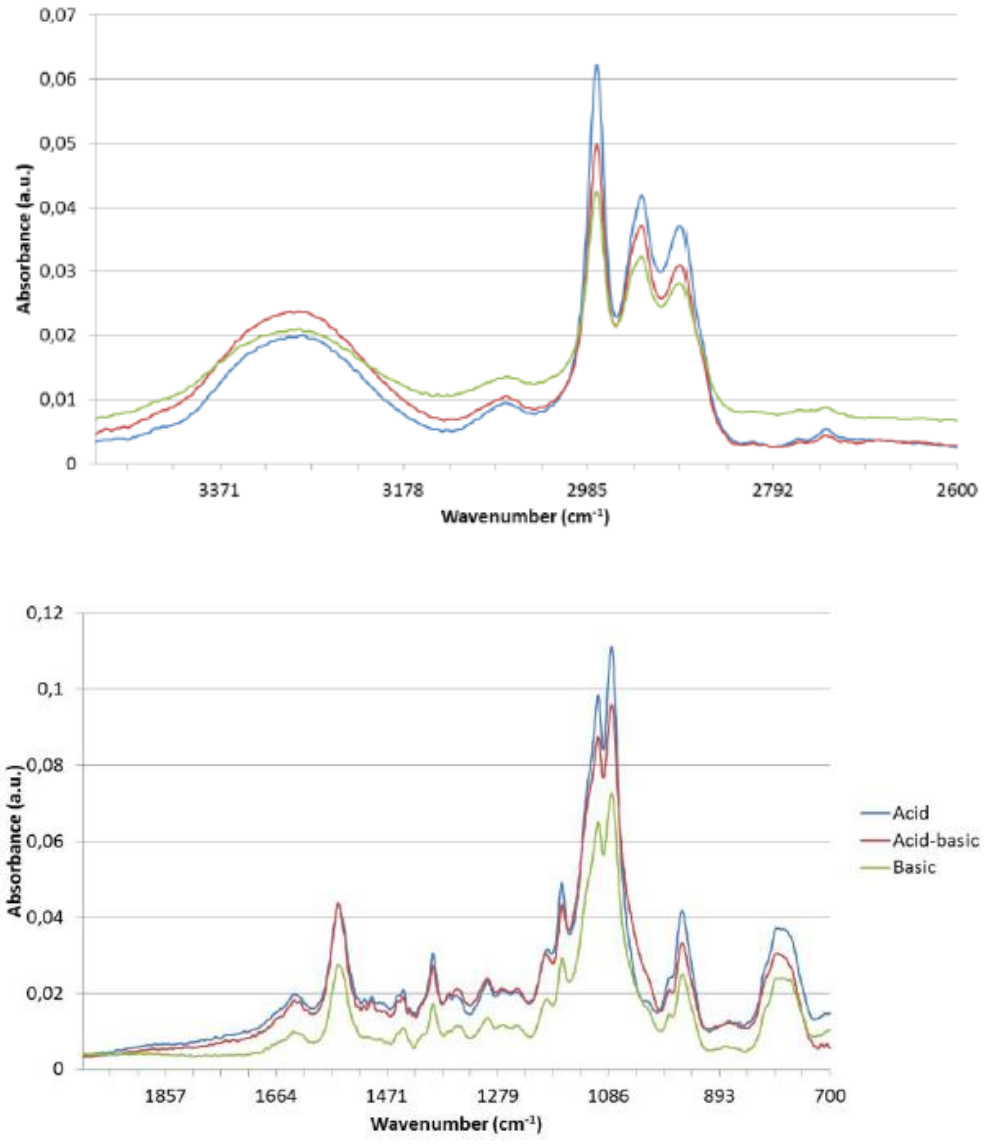

Fig. 3.4 FT-IR spectra of thiourea-bridged PSQ thin films in acidic catalysis (blue line), double acidic-basic catalysis (red line) and basic catalysis (green line) conditions.

Range	*Group and vibrational mode*
3600-3100 cm^{-1}	-OH stretching
3000-2850 cm^{-1}	-CH stretching (alkyl groups)
1650-1550 cm^{-1}	N-H bending (secondary amines)
1350-1000 cm^{-1}	C-C stretching (alkyl chains)
1470-1450 cm^{-1}	-CH bending (alkyl groups)
~1440 cm^{-1}	C=S stretching
1320-1000 cm^{-1}	-CO stretching
1190-1130 cm^{-1}	C-N stretching (secondary amines)
1130-1000 cm^{-1}	Si-O-Si
1170-1160 e 1100-1075 cm^{-1}	Si-O-CH_2-CH_3
950-910 cm^{-1}	-OH bending
950-810 cm^{-1}	Si-OH

Table 3.5. Significant peaks of thiourea-bridged PSQ in FT-IR spectroscopy; the peaks useful to evaluate condensation grade of the network are highlighted in grey colour.

As it can be observed from fig. 3.6, the acidic catalysis condition leads to a narrow peak, corresponding to Si-O-Si bond, at about 1080 cm^{-1}, but at the same time an high number of unreacted alkoxide groups and non-condensated silanols are found compared to the others catalysis. Basic conditions allow to obtain few residual alkoxides and silanols, however with a minor contribution of the Si-O-Si peak. Acidic-basic catalysis seems to be a good compromise as it allows to get few residual alkoxides and silanols corresponding to an high grade of condensation and an increased Si-O-Si bonds peak, indicated by a broader shoulder.

An analogous study was then conducted on the same matrices thermal treated at different temperatures in an inert nitrogen atmosphere for 1 h; the obtained FT-IR spectra are reported in figures 3.6, 3.7 and 3.8. It can be seen that an increase in temperature leads to an higher condensation grade, suggested by the appearance of a peak at about 1025 cm^{-1} corresponding to the increasing of Si-O-Si bonds number.

Furthermore the decrease of the OH stretching absorption band is evidence of a loss of the residual template contained in the pores.

As a conclusion of this investigation it was decided to carry out double step acidic-basic catalysis sol-gel synthesis, followed by a post-deposition thermal treatment at high temperatures to get a more condensed final network. However, it has to be kept in mind that over about 300°C some

organic bonds break and may lead to an unwanted depolymerization of the hybrid network or to structure modifications of guest molecules.

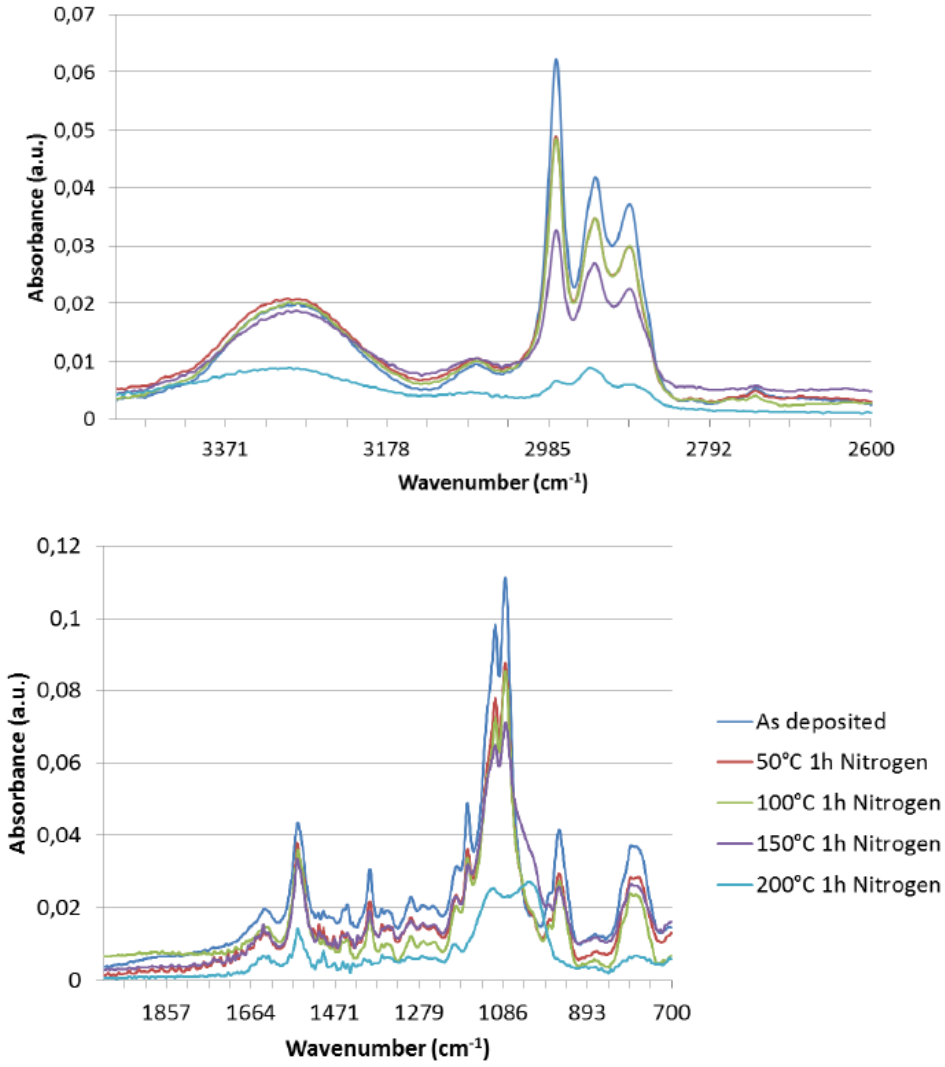

Fig. 3.6: FT-IR spectra of thiourea-bridged PSQ thin films synthesized in presence of an acid catalyst (HCl) and subsequently thermal treated in nitrogen atmosphere for 1 h at different temperatures.

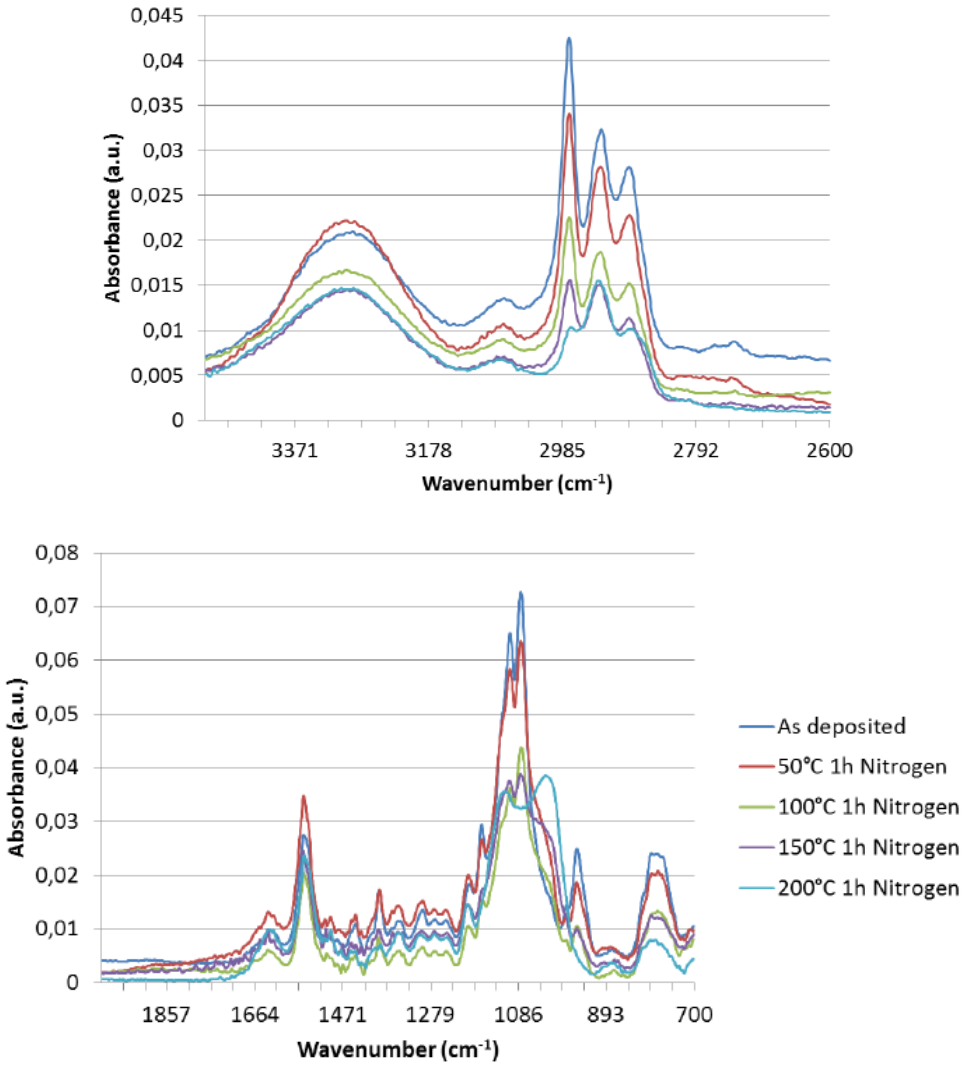

Fig. 3.7: FT-IR spectra of thiourea-bridged PSQ thin films synthesized in presence of a basic catalyst (TBAF) and subsequently thermaln treated in nitrogen atmosphere for 1 h at different temperatures.

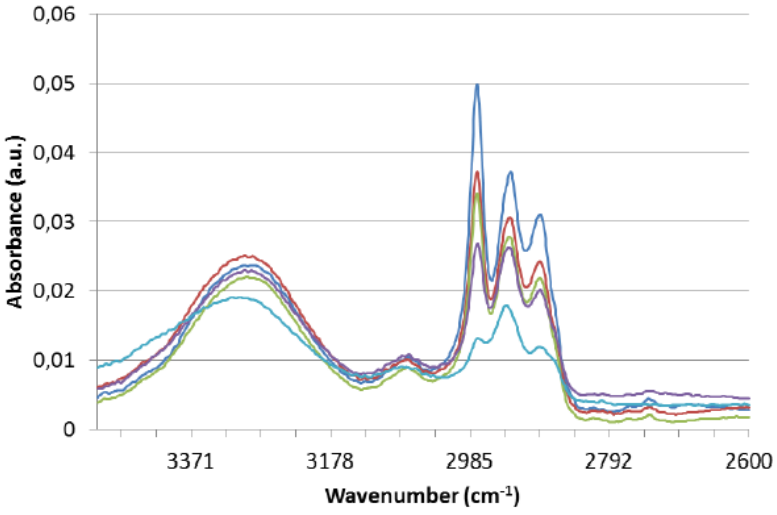

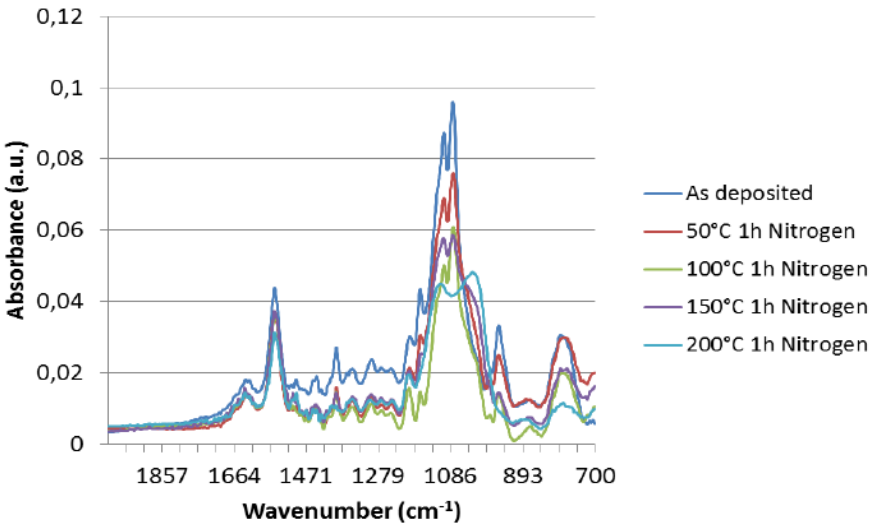

Fig. 3.8: FT-IR spectra for thiourea-bridged PSQ thin films synthesized in acidic-basic catalysis condition and subsequently thermal treated in nitrogen atmosphere for 1 h at different temperatures.

An increase of the condensation degree results in shrinkage, revealed by a film thickness reduction, due to the drying process of the material. Thicknesses of the films, thermal treated at different temperatures for 1 hour in nitrogen atmosphere and deposited via spin coating (3000 rpm for 30 s), were evaluated by ellipsometric measuments and the corrisponding data are reported in fig. 3.9. It can be noticed that increasing the temperature led to a progressive film thickness reduction.

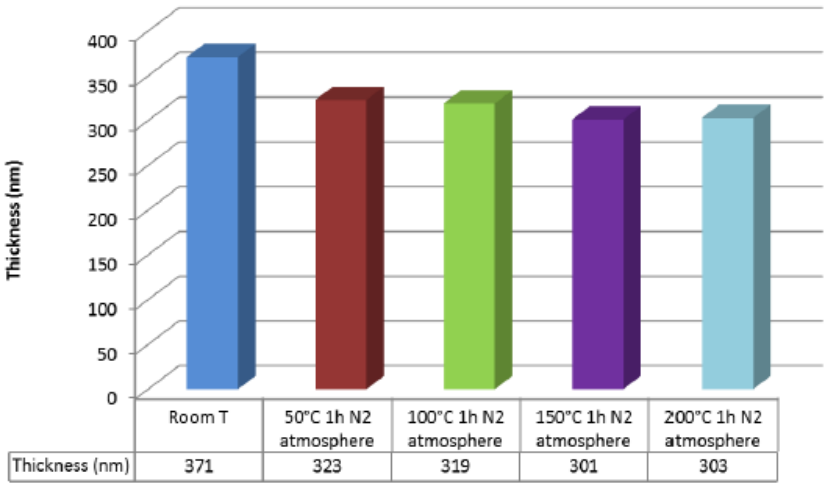

Fig. 3.9: film thicknesses of thiourea-bridged PSQ samples synthesized in acidic-basic catalysis condition after thermal treatment at different temperatures for 1 hour in nitrogen atmosphere.

Thiourea synthesized following the acidic-basic procedure was therefore selected to be the matrix in which entrap Zinquin; confocal microscope analysis were conducted on the samples to investigate

the response and reversibility of the fluorescent molecule. The samples were thermal treated for 1 hour in nitrogen atmosphere at 150°C and 200°C.

The film thermal treated at 150°C gave a base fluorescence of about 20, which increased to a value of 33 after its immersion in a zinc acetate aqueous solution 100 nM for 10 minutes. Washing the film for 10 minutes in bidistilled water caused an increase of the fluorescence signal to 41 and to 47 after immersion in the same medium for 10 additional minutes.

Zinquin, therefore, showed no reversibility in the requested conditions.

The sensing test was then carried out, in the same conditions, on the sample thermal treated at 200°C. An increase of the fluorescence signal from 98 to 123 was observed after immersion for 20 minutes in the solution containing zinc ions, 100 nm (fig. 3.10) followed by an initial decrease to 116 after washing the film for 10 minutes; however, keeping the sample in the washing medium for 16 hours, raised the value to 120.

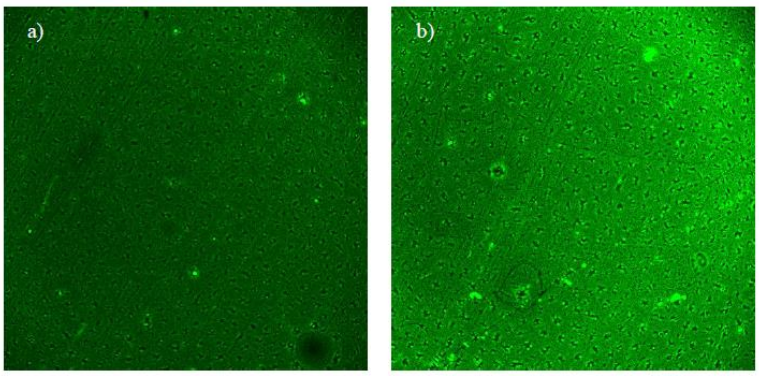

Fig. 3.10: confocal microscope images of a) base fluorescence of thiourea synthesized in acidic-basic condition and 2% mol/mol Zinquin sample and b) fluorescence after immersion for 20 minutes in aqueous zinc acetate solution 100 nM.

Fluorescence measurements were also performed on a control sample made of thiourea synthesized in acidic-basic condition in absence of the fluorescent molecule and thermal treated at 150° for 1 hour in nitrogen atmosphere.

Its fluorescence signal was low: a value o 14 was registered for the film as deposited; after immersion for 10 minutes in the aqueous zinc acetate solution (100 nM), the sample showed an increase of fluorescence to 19 that could be caused by interactions between zinc ions and amine groups that are part of organic bridges. However even the presence of donors group such as OH in non-condensated silanols could be responsible to some extent for the intrinsic fluorescence of thiourea-bridged PSQ.

To further investigate this aspect a second matrix synthesized starting from bis-(triethoxysilyl)-biphenyl (see fig. 3.11) monomer was chosen and studied; a stable material with a less reactive organic bridge was obtained.

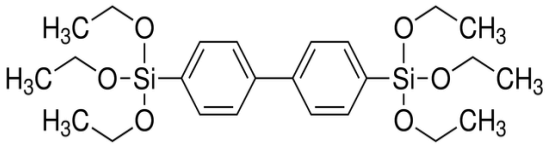

Fig. 3.11 bis-(triethoxysilyl)-biphenyl monomer.

The synthesis procedure is the same used for systems containing ZinPyr-1 as guest molecule, with acid catalyst; thin films were deposited on fused silica and silicon wafer substrates at a speed of 3000 rpm for 30 s. Zinquin was solved in pure methanol and added to the sol, before the deposition through spin-coating, in a molar percentage of 2% as regards to silica moles contained in the precursor. Confocal microscope analysis revealed a reduction in fluorescence after immersion for 10 minutes in aqueous zinc acetate solution 100 nM, from 51 (base fluorescence of the film) to 40.
In these conditions Zinquin did not show reversibility which could be ascribed to the fact that the environment somehow influnces the bind capacity of the fluorophore.
Ellipsometric analysis provided an estimation of film thicknesses was obtained, given Y,Δ and transmittance values through an experimental fitting based on Cauchy model; the results are reported in fig. 3.12.

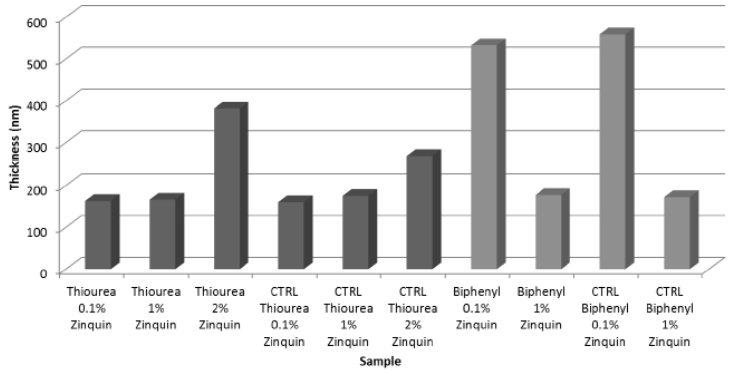

Fig. 3.12: films thicknesses of thiourea-bridged PSQ samples synthesized in acidic-base double step catalysis condition and of biphenyl-bridged PSQ samples, both doped with Zinquin. For comparison the obtained data of the control samples are also reported.

Comparing the thicknesses of the control sample with those of the same matrices embedding the fluorophore, it can be concluded that introducing a certain percentage of Zinquin as guest molecule in an hybrid organic-inorganic PSQ film leads to thicker films; in particular for thiourea-bridged PQ systems a significant increase in thickness for Zinquin percentages over 2% molar was observed. The difference between the thicknesses of the control sample and of the doped film in the

case of biphenyl-bridged PSQ systems was less notable compared to the previous matrix, but in general it allow to obtain thicker films at a fixed percentage of fluorophore.

Zinquin molecule did not showed reversibility as demonstrated by the confocal microscope's analysis performed. Varying pH of the buffer and increasing its temperature were considered as possible solutions to reach the reversibility of the system; however the requested operative conditions compatible with living pancreatic β-cells impose a pH in the range 7-7.5 and a temperature betweeen 34-37°C and changements within intervals were not sufficient to decrease the fluorescence of the film after washing with buffer.

As TSQ and Zinquin didn't satisfy the condition of reversibility, the attention was focused on a third fluorophore.
A fluorescent molecule with a supramolecular structure was synthesized in collaboration with the group of prof. V. Amendola (University of Pavia).
Host-guest systems with an hybrid organic-inorganic matrix composed of phenyl-bridged PSQ and cage 2 as guest fluorescent molecule were developed. Chemical structure of phenylbridged monomer is reported in fig. 3.13.

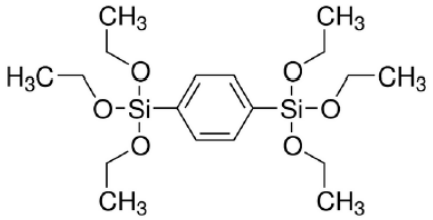

Fig. 3.13 phenylbridged monomer

This matrix was selected thanks to its low reactivity and high stability of the organic bridge, that avoids interactions between zinc ions and the organic fragment. As for the other systems, thin films were deposited on sodalime glass substrates via spin-coating, at a speed of 3000 rpm for 30 s. Fig. 3.14 reports the UV-visible spectrum of phenyl-bridged PSQ film with 3% molar of cage 2 and of corresponding control sample (the matrix without fluorophore); when cage 2 is embedded within the matrix threee broad absorption peaks appear at around 359, 378 and 400 nm.

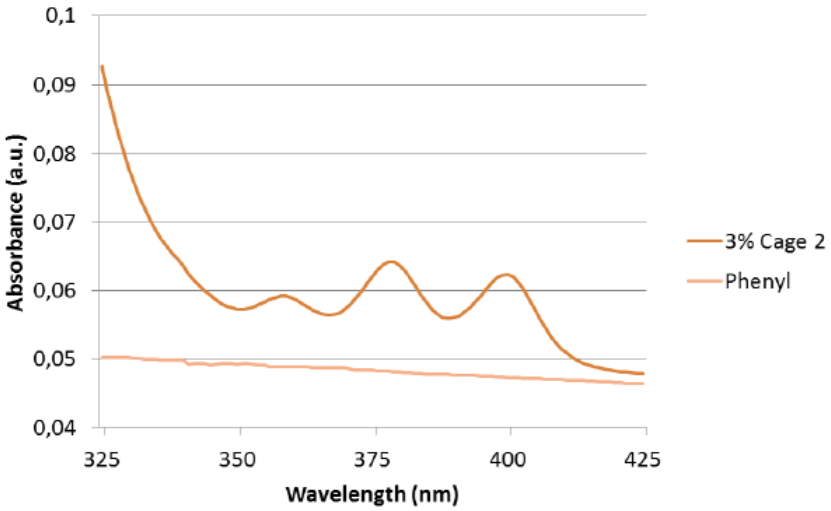

Fig. 3.14: UV-visible spectrua of phenyl-bridged PSQ films with 3% of cage 2 (dark orange line) and of the pure matrix (light orange line).

Two samples containing 2% and 3% mol/mol of cage 2 were synthesized, thermal treated at 100°C for 1.5 hours in nitrogen atmosphere and tested and finally tested through alternated immersions in aqueous zinc acetate solution 100 nM and washing buffer.

At each step of the test, a fluorescence spectrum was acquired with an excitation wavelength of 400 nm. The collected results are reported in fig. 3.15.

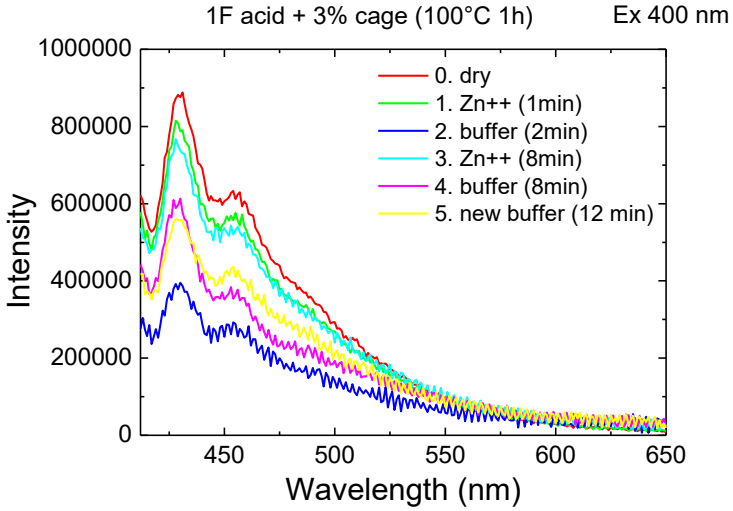

Fig. 3.15. fluorescence spectra of phenyl-bridged PSQ thin films doped with 3% mol/mol of cage 2.

From the plot of the calculated areas corresponding to the two main peaks, it seems that the system responds to 100 nM Zn^{2+} in buffer solution, and regenerates after immersion in pure buffer (fig.3.16).

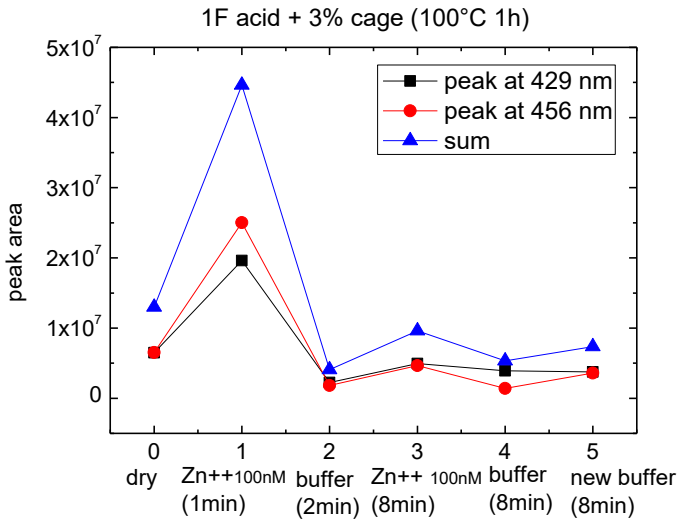

Fig. 3.16 Peak areas trend for the emission peak at 429 nm (black line) and of the peak at 456 nm (red line).

Excluding the interaction within zinc ions and organic bridge of the matrix (for its high stability), another possible explanation that justify the behaviour of the system is that fluorophore's leaching occurs during the washing step, with a consequent decrease of the fluorescence signal. In order to verify this hypothesis, absorption spectra of the film and emission spectra of washing buffer were collected at different times of immersion, and then reported in fig. 3.17.

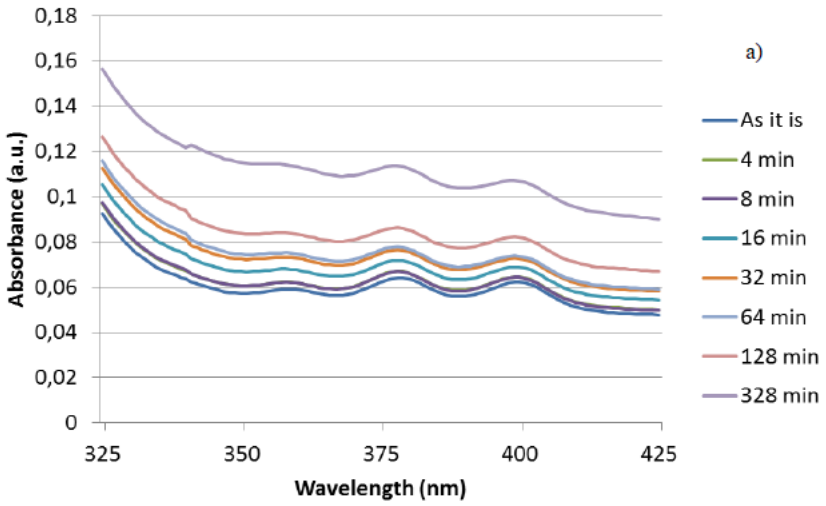

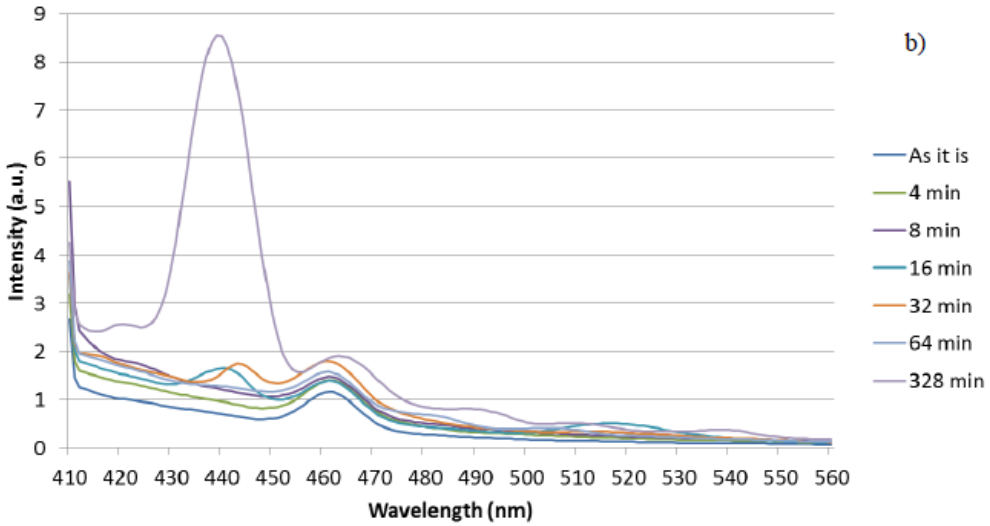

Fig. 3.17: a) absorption spectrum of phenyl-bridged PSQ doped with 3% mol/mol of cage 2 after different immersion time in washing buffer; b) emission spectra of washing buffer.

From fig. 3.17 a, it can be observed that there is no relevant change in the absorption spectrum of the film at different times of immersion; on the other hand, the emission spectrum of washing buffer (fig. 3.17 b), with excitation at 400nm, reveals an intrinsic fluorescence indicated by an emission peak at 461 nm.

Flurophore leaching becomes significant as a function of the immersion time in agreement with the appearance of an absorption peak in the range 440-445 nm. After 328 minutes, this fluorescence signal becomes strong indicating an important diffusion of fluorophore molecules from the system toward washing buffer.

The influence of thermal treatments on film thickness, measured by ellipsometry spectroscopy, was investigated and the obtained results are here reported (fig. 3.18).

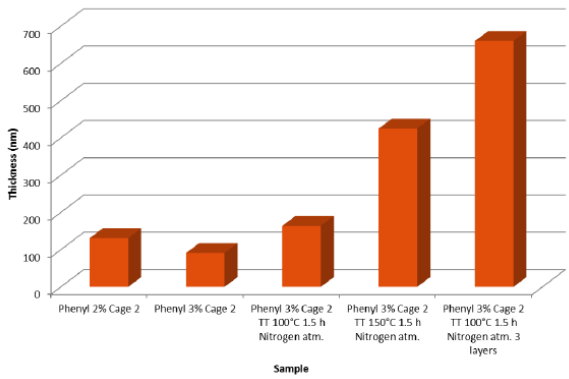

Fig. 3.18 Films thickness data for phenyl-bridged PSQ doped with different percentages of Cage 2, treated at different temperatures for 1.5 hours in nitrogen atmosphere. On the right, a multilayer sample composed of 3 layers has a film thickness of 660 nm.

Cage 2, the synthesized fluorescent molecule with a supramolecular structure, showed reversibility and selectivity overall other ions in the medium; however it was evident that the Zn^{2+} sensing measurements were negatively affected by the occurred leaching process, giving unreliable data.
Therefore Zinpyr 1 was selected as the next fluorescent molecule to be employed.

Two different systems were synthesized employing Zinpyr 1 as fluorophore.
The first one was synthesized starting from ph-PSQ precursor as follows.
A solution of 1,4- bis(triethoxysilyl)benzene, ethanol (EtOH) and bi-distilled water was mixed in a monomer/H_2O = 1/6 molar ratio, using hydrochloric acid (HCl) 1 M as catalyst. The Si–C bonds linking two ethoxysilanes to the bridging benzene ring are hydrolytically stable. As hydrolysis and condensation progress, a three dimensional SiO_x network, incorporating benzene rings as network formers, grows and the solution becomes more viscous. Before spinning, the obtained sol and ZP1 fluoprophore were mixed together. The films were then deposited by spin coating on the substrates, tuning the solution concentration in EtOH and/or the spin coating speed in order to obtain, after a thermal treatment at 80 ◦C for 30 min, a thickness of about 200 nm. A postdeposition bake was performed to promote solvent evaporation and to reach a stable cross-linking degree.
Micro/nano-structured sinusoidal films made of mesoporous hybrid organic-inorganic SiO_2 doped with a fluorophore were obtained through sol-gel chemistry starting from tetraethylortosilicate (TEOS) as SiO_2 precursor and employing ZP1 as flurophore and hydrochloric acid (HCl) as catalyzer. Long-range ordered periodic nanostructures were produced within the films through the self-assembly of the ionic surfactant CetylTrimethylAmmoniumBromide at the critical micellar concentration. The templating agents were removed by soft thermal treatments in oxygen atmosphere at by washing the samples in an ethanol/HCl solution at 50°C for 12 hours.
Well defined sinusoidal nanometric and micrometric structures were obtained in the films through the soft-lithography patterning method.
Zn^{2+} sensing was performed by fluorescence spectroscopy both in water and in buffer solution in order to confirm the selectivity of the fluorophore against other ions.
Emission spectra were recorded in focused ranges of wavelength by Jasco FP-6300 with excitation and emission bandwidth of 5 nm, data pitch 1 nm and scanning speed of 200 nm/min. In order to exclude reflected radiation from resulting Intensity detected, films were positioned in the cuvette containing the medium tilted of about 30°.
Preliminary leaching tests were firstly performed through fluorescence spectroscopy (fig. 3.19). They showed that the fluorescence emission was stable after immersion of the film in liquid for one

hour, as a consequence of the removal of the percentage of the dye that was just adsorbed to the film surface.

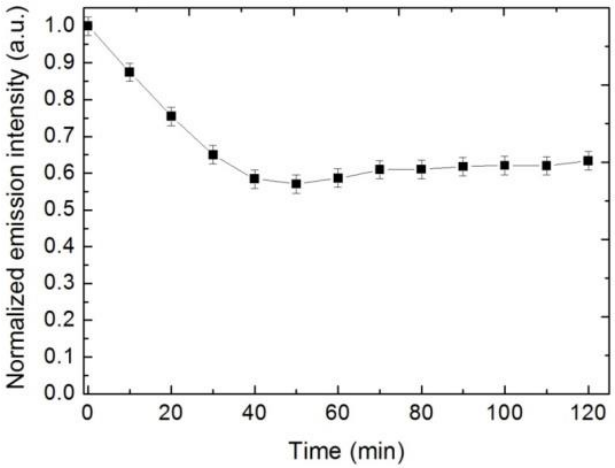

Fig. 3.19. Leaching test performed on micro/nano-structured sinusoidal films made of mesoporous hybrid organic-inorganic SiO_2 doped with ZP1 fluorophores.

Zn^{2+} sensing was then performed both in water and in buffer solution (1L of deionized water, 2,603 g of HEPES, 6,954 g of NaCl, 0,35g of KCl, 0,105 g of $MgCl_2 \cdot 7H_2O$, 0,163 g of KH_2PO_4, 2,603 g of $NaHCO_3$, 0,547 of $CaCl_2 \cdot 2H_2O$) in order to confirm the selectivity of the fluorophore against other ions.

The obtained results for flat ph-PSQ films and for mesoporous hybrid organic-inorganic SiO_2 structured films are shown below (fig. 3.20-3.21). The plots show the variation of the maximum intensity emission of the fluorophore, before and after immersion of the film in media containing different concentrations of Zn^{2+} ions.

The detection limit of ph-PSQ films is 1 mM in water, and 10 mM in buffer solution. The system showed response and recovery times in the order of few tens of seconds and reversibility while in the case of the long range ordered periodic structures is 100 nM in water, and 10 mM in a buffer solution, maintaining analogue fast and reversible response.

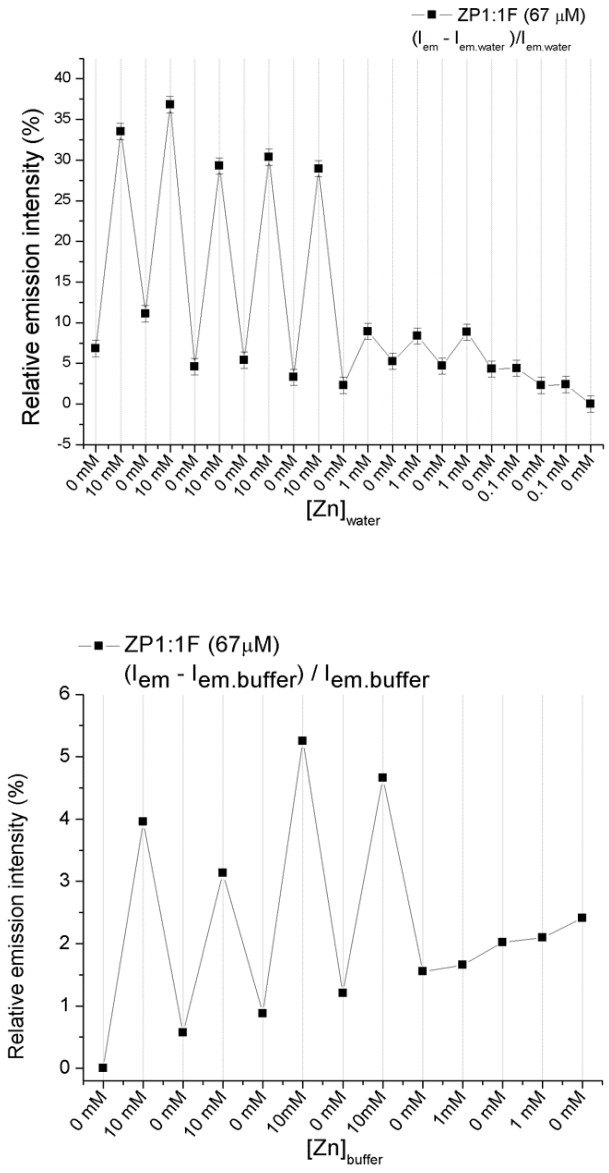

Fig. 3.20. Zn^{2+} sensing on ph-PSQ films (1F) in water (up) and in buffer solution (down). $\lambda_{excitation}$ = 492 nm, $\lambda_{mission}$= 536 nm; Zn ions source: zinc acetate.

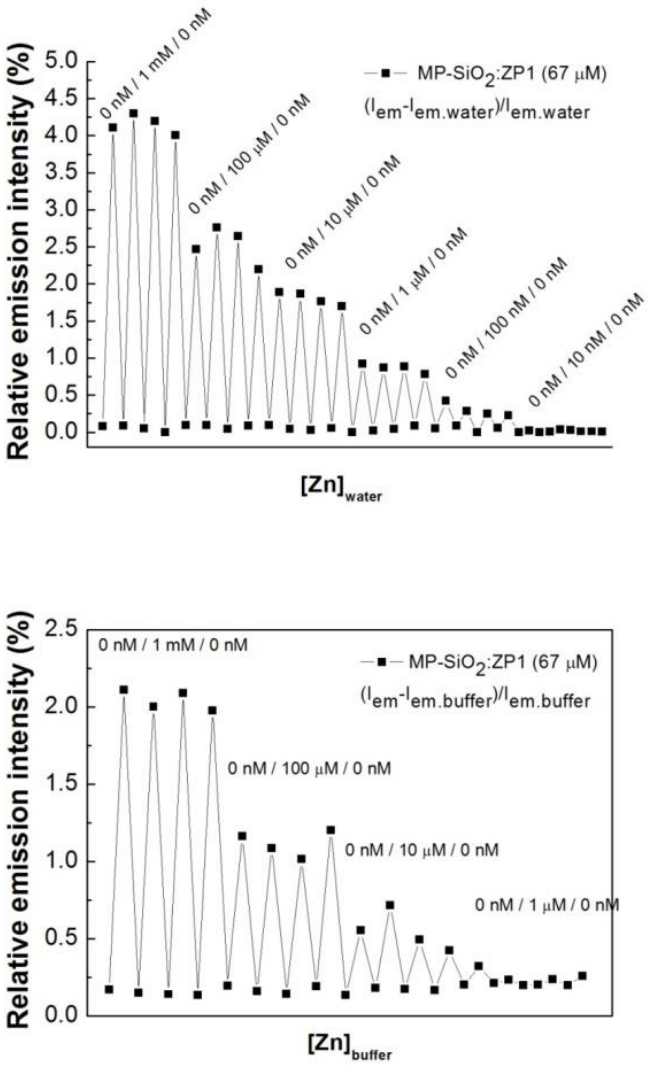

Fig. 3.21. Zn^{2+} sensing on mesoporous hybrid organic-inorganic SiO_2 (MP-SiO_2) mesoporous films in water at variable Zn^{2+} concentrations (up) and at 100 nM (down). $\lambda_{excitation}$ = 492 nm, $\lambda_{emission}$= 536 nm; Zn ions source: zinc acetate.

Flat films and structured films are both able to detect Zn^{2+} ions in a fast and reversible way in water and in buffer solution. Nanostructured mesoporous silica-based films are more sensitive, having a detection limit of 100 nM, which falls into the concentration range of biological interest.

However, this result is obtained in water while in buffer solution the detection limit is higher; therefore the selectivity of the fluorophore is still not optimal.

It has to be noticed that the regeneration step brings back to the base emission intensity very efficiently.

The sensor systems synthesized employing Zinpyr 1 as fluorophore are able to detect Zn^{2+} down to the nanomolar range and they allow to detect dynamic concentrations in time, showing selectivity

overall other ions, stability provided by covalent binding of the fluorophore, and most relevantly reversibility.
All these requirements were not concurrently satisfied by no one of the previous combination of fluorophore and matrix.

Fluorescence microscopy measurements were carried out on sensors films integrated in microfluidic devices (Fig. 3.22); however photobleaching of the fluorophore occurred. For this reason, further tests are still in progress considering higher sensitivity measurement systems.

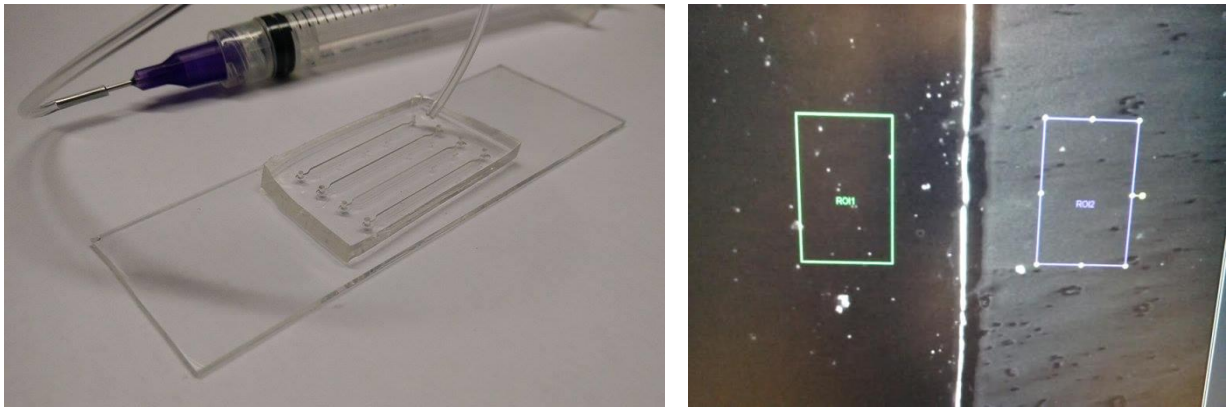

Fig. 3.22 Microfluidic setup (left) and fluorescence microscopy measurements when zinc is present and absent (right).

CHAPTER 4

Antibiotic residues detection in milk: industrial and scientific background

4.1 Contaminants of milk and dairy products

The concern for food safety in milk industry has determined the definition levels of residues of veterinary medicinal products, of which antibiotics represent a significant part, by the EC Regulation (no. 2377/90).

However, despite the obvious demand for quantitative multiresidue detection methods that can be carried on a routine basis, there is currently an evident lack in the development of such systems.

In particular, a multianalyte detection device able to simultaneously quantify different antibiotics within minutes is needed.

A series of four antibiotic families are of particular interest due to their routine use for treatment in bacterial infection and prophylactic purposes: fluoroquinolones, sulfonamides, ß-lactams and tetracyclines. The Maximum Residue Limits (MRLs) are 100 µg/L for fluoroquinolones, sulfonamides, tetracyclines and 4 µg/L for ß-lactams. The study until now has been focused on ampicillin (fig. 4.2), that belongs to the ß-lactam family. Their excessive use in dairy cow diet has given rise to stronger bacterial resistance, which represents a serious problem in the efficiency of classic anti-bacterial treatment in humans [1].

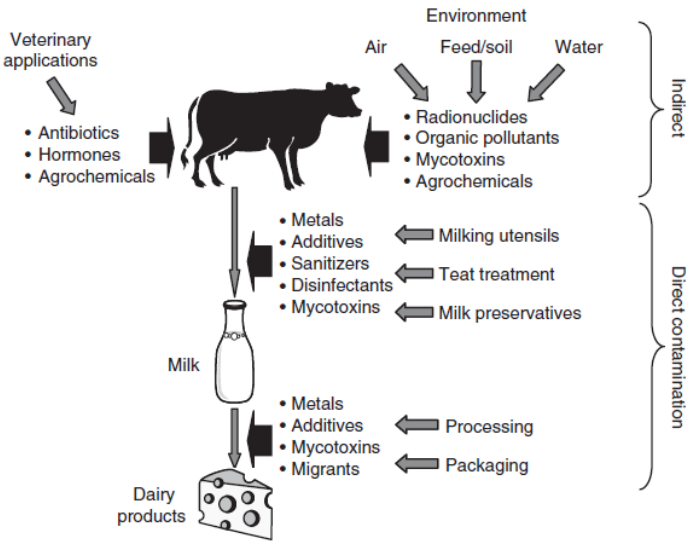

Fig. 4.1 Contaminants of milk and dairy products and their respective sources. 'Migrants' refers to indirect food additives and polymerization residues and polymerization residues. [1]

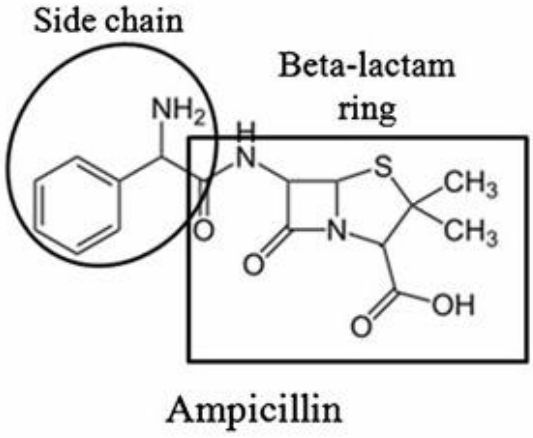

Fig. 4.2 Ampicillin belongs to the family of B-lactams and its MRL is 4 μg/L.

4.2 Risks associated with drug residues in milk

The control of drug residues in milk is performed for three main reasons:

1) Ethical aspects: consumers should be guaranteed non-contaminated products free from antibiotic substances. The consumers' confidence in milk and dairy products as safe and wholesome food is of utmost importance to the dairy industry.

2) Health aspects: hypersensitive consumers may be subject to allergic reactions. The β-lactam antibiotics are not toxic to humans but there may be adverse effects due to the occurrence of drug residues in food. Allergy and hypersensitivity may lead to severe reactions in humans and up to about 10% of humans are diagnosed to be hypersensitive or allergic to β-lactams. However, very few cases of allergic reactions caused by consumption of residue contaminated food have been reported.

3) Technological aspects: many starter cultures used in the manufacture of fermented products, e.g. yoghurt and cheese, may be inhibited by β-lactams and other antimicrobial substances. If the fermentation is incomplete, the product quality will be impaired and occasionally milk may even have to be discarded, in both cases causing the dairy substantial economic losses. The concentration of β-lactams needed for this type of inhibition is, however, rather high.

4.3 Biosensors in food analysis

A biosensor consists of a biological sensing element (ligand) that interacts with the analyte and is in close contact with a physical transducer that senses the physicochemical change that follows the

interaction, e.g. change in mass or electrical potential. The transducer converts the biological response into an electrical signal that is amplified, stored and quantified by a processor.

There are many different types of biosensors and they may be classified according to the biological element used, e.g. enzymatic or immunological, or to the transducing system applied, e.g. optical, amperometric, potentiometric or thermal.

Standard test methods for antibiotics detection are based on chromatographic techniques such as high performance liquid chromatography (HPLC) coupled with UV spectroscopy or mass spectroscopy. Despite efficiency and high screening capability, those techniques require time-comsuming sample preparation and have to be run by skilled technicians. Other protocols for antibiotic detection in milk are based on microbial inhibition assay [2] which require several hours before a result, and might report false positives. Immunoassay tests for the detection of antibiotics have been developed based on enzyme-linked immunosorbent assay (ELISA) [3], parallel affinity sensor array (PASA) [4], or radio-labelled immune receptors. Those tests are reliable and present a high screening capability, but they are laborious, have to be run in a laboratory and require at least a few hours for the assay time.

In response to the demand for rapid and cheap detection protocols, a few tests based on lateral flow immunochromatography has recently been commercialized (Beta star) [5] where the sample mixed with labelled immune-reagents is absorption-driven by lateral flow through a nitrocellulose strip. The response tests are fast (less than 10 min), easy to perform, cheap, sensitive and specific, but are not able to parallel detect multiple antibiotics.

4.4 Fundamentals of surface plasmon resonance biosensors

A surface plasmon polariton (SPP) is an electromagnetic wave coupled to collective electron oscillations, propagating along the dielectric-metal boundary and exponentially decaying away from it.

The electromagnetic field of an SPP at a dielectric–metal interface is obtained from the solution of Maxwell's equations in each medium, and the associated boundary conditions. An SPP is a transverse-magnetic wave characterized by two main parameters which are the propagation constant and the electromagnetic field distribution.

The propagation constant of an SPP, β, can be expressed as follows:

$$\beta = \frac{\omega}{c}\sqrt{\frac{\varepsilon_M\,\varepsilon_D}{\varepsilon_M + \varepsilon_D}}$$

where ω is the angular frequency, c is the speed of light in vacuum, and ε_M and ε_D are the dielectric constant of the metal and dielectric, respectively.

The reported equation describes an SPP if the real part of ε_M is negative and its absolute value is smaller than $\varepsilon_{D.}$

Several metals fulfill this condition at optical wavelengths, including gold which is commonly employed in SPR sensors.

Spatial periodicity and attenuation of an SPP in the direction of propagation are respectively described by the real and imaginary parts of the propagation constant. [6]

In principle, SPR sensors can be considered thin-films refactometers that measure variations in the refractive index occurring at the surface of a metal film supporting a surface plasmon.

The field confinement and enhancement at the interfaces makes surface plasmons extremely sensitive to changes in the dielectric properties of metal and dielectric. Such an effect is exploited in these sensors: the coupling conditions for plasmon excitation change when a target molecule binds to the surface, due to local refractive index variations. [7]

4.5 Plasmonic architectures for antibiotic detection

The presented research work aims to the development of an innovative plasmonic-microfluidic platform for performing high-sensitive, quantitative, selective and cost-effective detection of residual antibiotics in milk.

The ground-breaking ambition of this proposal is the integration of state-of-the-art technologies in multilayer microfluidic sample preparation and plasmonic biosensing in one miniaturized system that achieve antibiotic detection from milk in a cost-effective and time-effective way.

Commonly used technologies show major similar drawbacks: requirement of substantial amount of sample and reagents, time-consuming sample preparation and need of ad hoc separate analysis for different targets. Altogether these drawbacks give rise to unfeasible costs for high-throughpuut milk analysis monitoring.

Sensors based on plasmonics provide a significant advance beyond the state of the art, because of the one-step label-free direct interaction on the metal surface, whose resonance monitoring allows a fast, in situ detection of a wide range of biological targets, without amplification or purification stages. The proposed plasmonic detection systems combine magnetic extraction with plasmonic detection in a unique system. Few examples of biosensors based on localized SPR are present in the

market (BiaCORE) [8] neither exploit magnetic–core metal-shell nanoparticles or plasmonic gratings, nor are integrated on a chip for multiplex test.

Regarding microfluidics, the combination of compact multilayer actuation and detection to directly analyse antibiotics in serum, or with limited pretreatment, will lead to a truly innovative and cost effective approach towards in situ-applications.

In the project two key characteristics of the plasmonic detection, high sensitivity and straightforwardness of integration, will be exploited and engineered on chip, arranged in a multiplex platform for simultaneous and real time detection of different antibiotics.

Two different plasmonic architectures for antibiotic detection were developed, exploiting Surface Plasmon Resonance (SPR) of functionalized magnetic-core metal-shell nanoparticles (Fig. 4.3-4.4), or Long Range and Short Range Surface Plasmon Polaritons (LRSPP and SRSPP) of plasmonic gratings.

4.6 Innovative adopted approaches

An original and innovative SPR-based sensing strategy was proposed. It consists in combining resonant optical and magnetic properties in a single nanostructure, consisting of a superparamagnetic-core gold shell nanoparticels, exploiting a magnetic separation process combined to an optical (plasmonic) readout. The use of nanoparticles guarantees a high sensitivity, cheapness of fabrication and easy integration on chip. Core-shell nanostructures have gained great interest in the past decades as they allow to combine multiple functions or properties not obtainable in individual materials. Concerning our developed system, magnetic extraction is ensured by the superparamagnetic iron oxide core while the Au shell layer provide a strong plasmon resonant optical response to the nanoparticle, with a resonant frequency determined by geometry, the dielectric properties of the nanoparticle core, and the surrounding medium of the nanoparticle. Furthermore, it provides a relatively chemically inert surface layer that can be functionalized with complementary aptamers selective for specific antibiotics.

Detection is based on surface plasmon resonance, an optical phenomenon that occurs at the interface of two transparent media of different refractive index. A light beam coming from the side of the higher refractive index will be partly reflected and partly refracted, but above a certain critical angle of incidence no light will be refracted and total internal reflection is observed. However, a component of the light, the evanescent wave, will propagate towards the media with the lower refractive index and if the interface between the media is covered with a metal film, e.g. gold, the evanescent wave will interact with free electrons in the metal. Light energy will thereby be lost

to the metal and the intensity of the reflected light will decrease. This phenomenon is referred to as surface plasmon resonance (SPR) and only takes place at a sharply defined angle of incidence, the SPR angle [9].
Magnetic-core metal-shell nanoparticles were synthesized through the growth of a continuous, uniform Au layer on a magnetite nanoparticle. Amine-functionalized magnetite nanoparticles were first decorated with gold nuclei (few nm diameter), separately prepared, through electrostatic interaction between gold colloids and the functional groups of the nanoparticles. The small gold nanoparticles successively acted as nucleation sites for the final reduction of a plating solution through a reductive agent, with formation of the metal shell. [10][11]

To prevent unspecific recognitions, selective probes directly coupled with plasmonic signals will be exploited, functionalizing the metal surfaces with complementary aptamers as probes. Concerning the detection, core-shell sensors will be trapped on the sensing region through a magnet placed under the waveguide layer, in order to establish a proper out-of-plane magnetic gradient in the sensing area.
Limitations impeding the sensitivity of SPR biosensors for antibiotics might be related to the small refracrive index contrast of the analyte bound to the surface, slow diffusion from a sample to the sensor surface, and insufficient depth probed by SPs.

The second plasmonic structure consists of a thin metal films embedded in a refractive-index symmetrical layer architecture with a sinusoidal grating coupling, supporting the propagation Long Range Surface Plasmon Polaritons (LRSPPs). This idea was already considered by our group to develop gas sensors [12] and a similar strategy was exploited for the detection of analytes in complex solution, e.g in milk.
A planar structure consisting of a thick metal film sandwiched between two semi-infinite dielectrics supports two independent surface plasmons at the opposite boundaries of the metal film. When metal film is thin, coupling between these surface plasmons can occur, giving rise to mixed modes of electromagnetic fields-symmetric and antisymmetric surface plasmons. [7]
The developed metal slab waveguide exhibits two SPP modes with different profiles and dispersion characteristics, resulting from the superposition of the SPPs at its two metal–dielectric interfaces. These modes are classified with respect to their magnetic field profile inside the structure as symmetric and antisymmetric modes. The symmetric mode is also called long range SPP (LRSPP), since it exhibits lower confinement and greater propagation distance, while the antisymmetric mode

is called short range SPP (SRSPP) and presents greater confinement and attenuation [12]. The interrogation of LRSPs allows increasing the biosensor figure of merit with respect to SPR.

Functionalizaton of the metal surfaces with complementary aptamers needs to be carried out. The dielectric parameters and the geometry of the multilayer structure (substrate, dielectric-metal grating) were desgined in order to achieve matching conditions for the plasmonic mode.

Fig. 4.3 Scheme of superparamagnetic-core gold-shell nanoparticles, exploiting a magnetic separation process combined to a plasmonic readout.

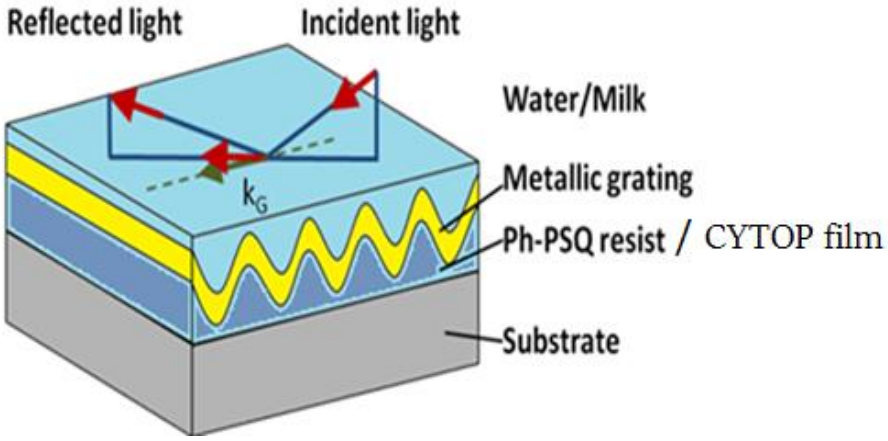

Fig. 6ì4.4 Scheme of sinusoidal surface plasmon metallic gratings embedded in a refractive index symmetrical architecture.

4.7 Sensor surface functionalization

SPR biosensors are devices consisting of a biorecognition element, able to recognize and to interact with a selected analyte, and an SPR transducer, that convert the binding event into an output signal. The biorecognition element needs to be immobilized in the proximity of the surface of a metal film supporting a surface plasmon.

Although many methods for covalent binding have been developed, amine coupling is the favourite choice due to its ease of use. Even if the method is straightforward, some critical issues arise with the procedure. These difficulties are usually related with the pH of the buffer, the molecular properties of ligand or analyte, the effectiveness of the regeneration after binding, steric problems.

The adopted ligand attachment protocol to the surface via primary amine groups is here reported. [13].

Carboxyl groups previously generated on a metal surface via interaction with 3-mercaptopropionic acid, are activated by injection of a mixture of N-hydroxysuccinimide (NHS) and N-ethyl-N'-(dimethylaminopropyl) carbodiimide hydrochloride (EDC). Formed active esters may readily react with amine groups of the aptamers. Ethanolamine is subsequently added in order to deactivate the remaining unreacted active esters.

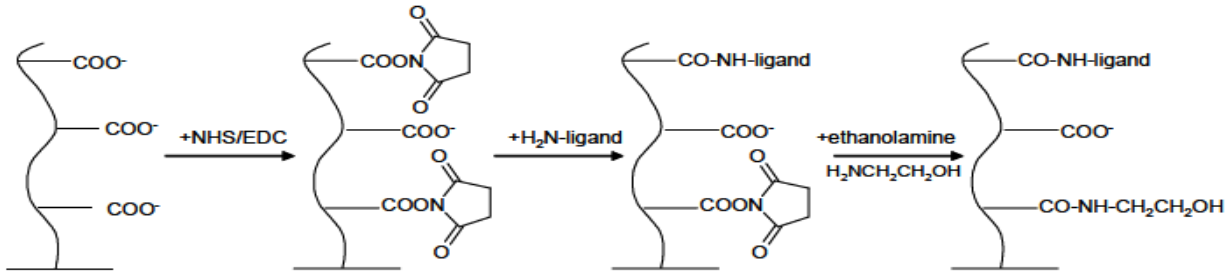

Fig. 4.5 Scheme of the amine coupling of aptamers to a sensor surface procedure.

Ampicillin binding aptamer (aptamer 5E01 #284, 40 DNA nucleotide bases, molecular weight: 12.239 g/mol) was purchased from Base Pair Biotechnologies. The aptamer was selected from a randomized 40-mer DNA library against the target Ampicillin sodium salt with proprietary methods. For usage, a centrifugation of the purchased aptamer was performed to ensure that the dried aptamer pellet was at the bottom of the tube. The aptamer pellet was resuspended in a TE buffer (10 mM Tris HCl, 0.1 mM EDTA, pH 7.5) to achieve a 100 µM concentration. The aptamer

solution was incubated at room temperature for 30 min, then briefly vortexed. Aliquots of 20 μL were prepared and stored at -20 °C.

Chapter 5
Materials, methods and results

Parallel development of two plasmonic architectures exploiting different but promising approaches was performed aiming to high resolution detection of residual antibiotics in liquid.

5.1 Magnetic plasmonic Fe_3O_4 core-Au shell nanoparticles synthesis

Commercial superparamagnetic amine-functionalized magnetite nanoparticles, FluidMAG-Amine, were purchased by Chemicell. FluidMAG-Amine nanoparticles are ferrofluids consisting of an aqueous dispersion of magnetic iron oxides with a diameter of 75 nm. The terminal amine group (-NH_2) allows covalent binding of specifically functionalized molecules or biomolecules.

Different strategies were considered and several synthetic protocols were tested to find optimal conditions. Those who led to the most promising results are described below:

1. The purchased commercial magnetic Fe_3O_4 nanoparticles (20 mg) were dissolved in 20 mL of deionized water and the pH value was adjusted to 4.0-5.0 by addition of 2 M HCl solution. A 5 mL sample of 1 g/L L-cysteine was added dropwise into the Fe_3O_4 NPs suspension. The mixture was then sonicated for 30 min, followed by addition of 5 mL of chloroauric acid ($3 \cdot 10^{-3}$ M $HAuCl_4 \cdot 3H_2O$), and the mixed solution was vigorous stirring for another 30 min. Then 5 mL of 1.0 wt % L-ascorbic acid was quickly added and reaction was allowed for 3 h under rapid stirring. At last, the products were separated magnetically and washed with deionized water and ethanol several times to eliminate organic and inorganic impurities.
L-cysteine, used to modify the magnetic core, was bound to the surface of the Fe_3O_4 spheres by the condension reaction between the COOH group of L-cysteine and OH groups on the surface of Fe_3O_4 spheres. The chloroauric acid ions ($AuCl_4^-$) were successfully adsorbed on the surface of Fe_3O_4 due to electrostatic interaction between positively charged L-cysteine-functionalized Fe3O4 and negatively charged chloroauric acid ions. L-ascorbic acid was used as a reductive agent to obtain Au NPs.

2. The purchased commercial magnetic Fe_3O_4 nanoparticles (20 mg) were dissolved in 25 mL of deionized water. 350 uL of chloroauric acid ($20 \cdot 10^{-3}$ M $HAuCl_4 \cdot 3H_2O$) and 300 uL of trisoudium citrate ($100 \cdot 10^{-3}$ M) were added and the mixed solution was vigorous stirring for 15 min. At last, the products were separated magnetically and washed with deionized water and ethanol several times to eliminate organic and inorganic impurities.

The colloidal samples were characterized through UV-Vis absorption spectroscopy and dynamic light scattering (DLS). The UV-Vis spectra of Fig. 5.1 show a plasmonic resonance peaked at 390 nm and at 550 nm for the nanosystem synthesized following respectively the first and the second protocol. These data suggest the possible formation of seeding Au nanoparticles around the magnetic core in the first case and of a shell in the other one. From the DLS measurements no significant data were obtained as particle aggregation took place.

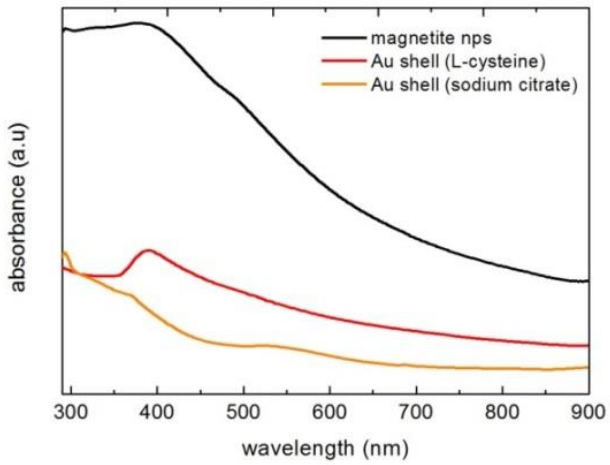

Fig.5.1 UV-Vis spectra of the starting magnetite nanoparticles (black line), of final core-shell particles obtained from the first described synthesis (red line) and from the second one (orange line).

TEM images of the purchased magnetite nps revealed that they are single iron oxide crystals with an average diameter of 8-14 nm of aggregated particles. Processing these clusters caused their decomposition in the particles they are composed; therefore all these facts represented a limit for the creation of other structures on them: the nanoparticles show just a few and limited more electrodense areas. The results of TEM characterization of bare magnetite nanoparticles and of on of the attempts done for the creation of the shell on them are reported in Fig. 5.2.

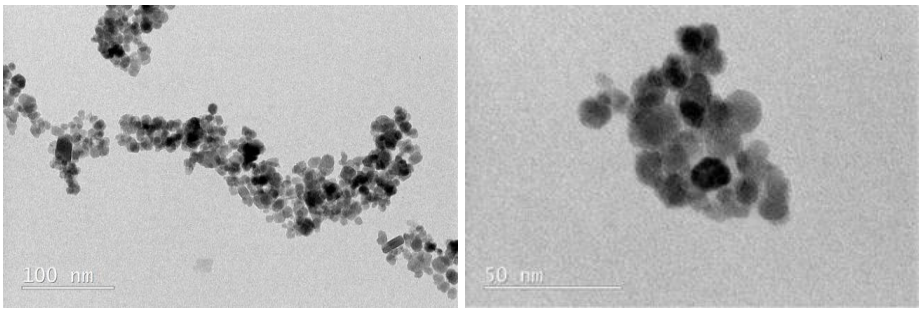

Fig. 5.2 TEM images of the purchased magnetite nanoparticles (single iron oxide crystals with an average diameter of 8-14 nm of aggregated particles) and of one of our sample after an attempt of creation of the gold shell on the nanoparticles.

We then decided to sinthesized both the iron oxide nanoparticles and the gold shell in collaboration with the group of Prof. Mammeri (Université Paris Diderot).

Fe_3O_4-core Au-shell nanoparticles were synthesized through the growth of a continuous, uniform Au layer on amine-functionalized magnetite nanoparticles, prepared using the polyol route, through a multistep process.

Fe_3O_4 nanoparticles, having a diameter of around 180nm, were synthesized starting from 2g of PEG, 5.8g of Na(Ac), 2.5g of FeCl3, 80ml of ethylenglycol. The mixture was then stirred and heated up to 200^0 C for 16h. The obtained powder was washed with ethanol and dried in oven at 60^0C overnight.

The obtained nanoparticles were subsequently functionalized by sonicating for 30 minutes 225 mg of Fe_3O_4 nanoparticles with 500 ml of ethanol and 2ml of APTES. 2ml of NH_4OH were then added and the mixture was continuously stirred for 6 hours. The obtained powder was washed with ethanol and dried in oven at 60^0C overnight.

The growth of an Au layer on the magnetic nanoparticle starts with self-assembly of gold colloids on the magnetite nanoparticles, previously functionalized with APTES. The small gold nanoparticles of a few nm diameter act as nucleation sites for the final reduction of plating solution with formation of the metal shell. For the synthesis of the gold seeds 3 ml of sodium citrate and 0,4 ml of NaOH were added to 42 ml of deionized water. Then 1 ml of THPC and 2 ml of $HAuCl_4$ were introduced in the solution and the resulting solution was stirred for 10min. The gold seeds were stored in a refrigerator (4^0C) prior to use.

The small gold seeds (1-3mn) and gold NPs (15nm) were attached to the amino groups on the surface of Fe_3O_4 nanoparticles through the electrostatic bond. The excess of gold seeds was then removed by centrifugation three times, and these particles were redispersed in water.

The K-gold solution was prepared as follows: 0.05 g of K_2CO_3 were dissolved in 200 ml of deionized water under magnetic stirring for 10 min. 3ml of the $HAuCl_4$ (1%) solution were then

added and the mixture was stirred for 2 hour. The resulting K-gold solution was stored in a refrigerator (4^0C) prior to use.

For the creation of the gold shell on magnetite nanoparticles the volume amounts of K-gold solution were fixed (10 ml), while the volume of Fe_3O_4-Au seeds was changed at different values. The reducing agent (formaldehyde) was added to the mixture of K-gold solution and Fe_3O_4-Au seeds. A color change was observed. The samples were stirred for 10 min to complete reaction.

The colloidal samples were characterized through UV-Vis absorption spectroscopy and dynamic light scattering (DLS), XRD, SEM and TEM analysis to obtain information about dimension, composition and morphology of the synthesized system. The obtained data are reported in the figures 5.3-5.7.

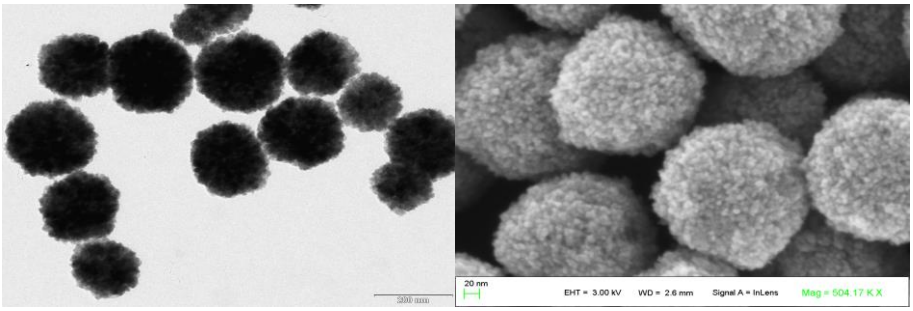

Fig. 5.3 TEM and SEM images of Fe_3O_4 and amine-functionalized Fe_3O_4 NPs

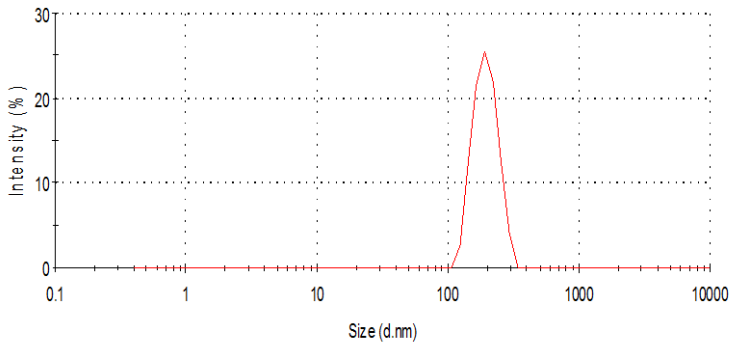

Sample	Size (TEM)	Size (DLS)	PdI
NT56-NH2	180nm	189 nm	0.107

Fig. 5.4 DLS data of the amine-functionalize magnetite nanoparticles.

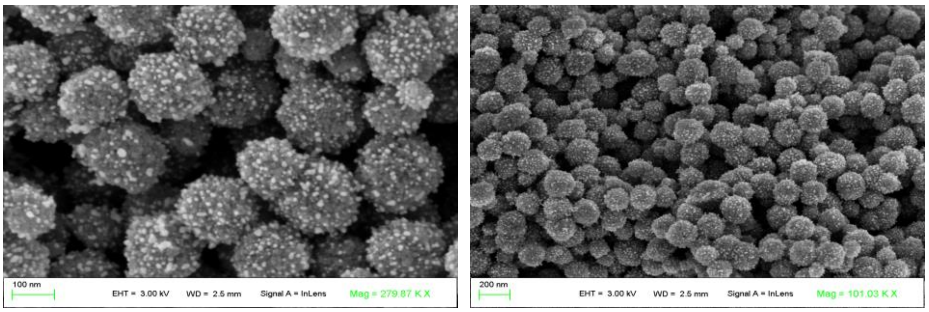

Fig. 5.5 SEM images of Fe_3O_4 – Au core-shell NPs.

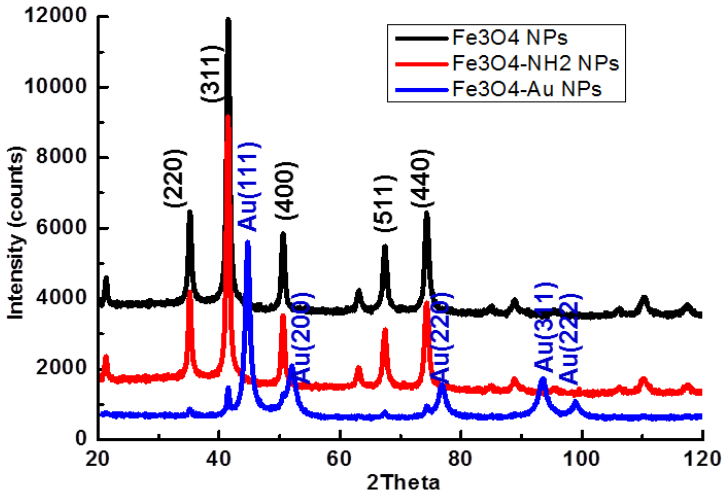

Fig. 5.6 XRD of Fe_3O_4, Fe_3O_4 amine functionalized and of Fe_3O_4 – Au core-shell NPs.

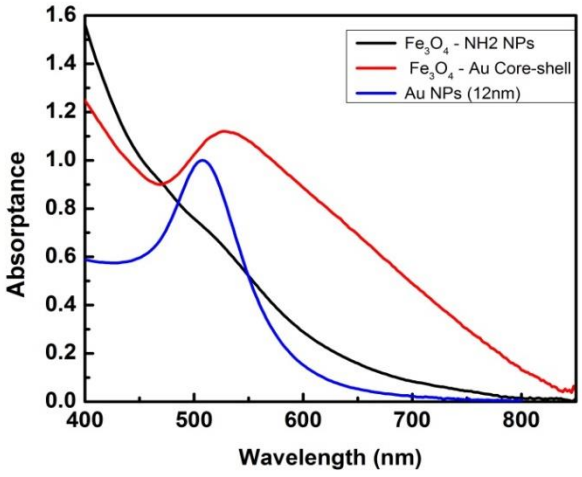

Fig. 5.7 UV-Vis spectra of Fe_3O_4, Fe_3O_4 amine functionalized and of Fe_3O_4 – Au core-shell NPs.

Attempts for the aptamer functionalization of the obtained Fe_3O_4 – Au core-shell system are now in progress.

5.2 Symmetric plasmonic gratings fabrication

Nanostructured plasmonic sensors were fabricated as sinusoidal surface plasmon metallic gratings deposited on a functional and porous hybrid sol–gel material, phenyl-bridged polysilsesquioxane (ph-PSQ). The upper surface of the metal layer is in contact with the liquid environment. Through a specific functionalization of the metal surface, the upper interface will work as sensitive element, changing its dielectric properties upon interaction with the analyte.

The sinusoidal surface plasmon metallic gratings (fig. 5.8) is a thin metal slab waveguide, in which the surface plasmon polaritons (SPPs) at the two metal–dielectric interfaces (metal/ph-PSQ and metal/water) superpose, resulting in two physical coupled modes: the long range SPPs (LRSPPs) and the short range SPPs (SRSPPs).

The combination of patternability, with tuneable composition and optical properties offered by organic-inorganic hybrid ph-PSQs gives the possibility to fabricate innovative optical sensors with straightforward processes. In order to obtain *symmetric* plasmonic gratings, the requirement to satisfy is the fabrication of a sinusoidal pattern in a material of refractive index close 1.33, that is water refractive index. The dielectric parameters and the geometry of the multilayer structure were designed in order to achieve specific optical properties.

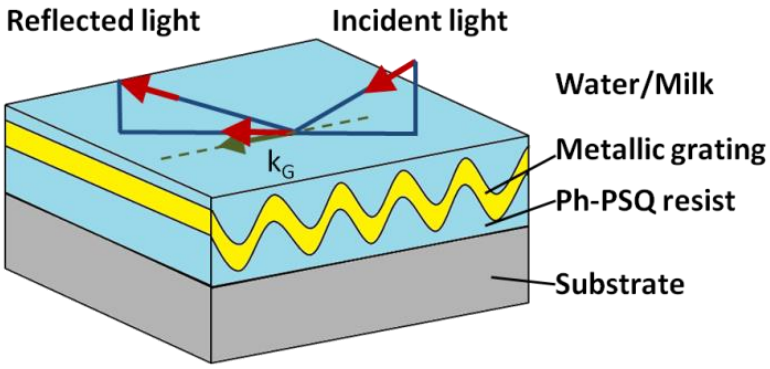

Fig. 5.8 Sketch of the multilayer structure of the symmetric plasmonic grating for the excitation of LRSPPs.

Ph-PSQ is an organic–inorganic hybrid sol–gel material synthesized via a sol–gel process using the 1,4-bis(triethoxysilyl)benzene monomer (96% purity, Sigma-Aldrich) at room temperature. A solution of 1,4-bis(triethoxysilyl)benzene, ethanol (EtOH) and bi-distilled water was mixed in a monomer/H_2O=1/6 molar ratio, using hydrochloric acid (HCl) as catalyst. The Si–C bonds linking two ethoxysilanes to the bridging benzene ring are hydrolytically stable. As hydrolysis and

condensation progress, a three dimensional SiO_x network, incorporating benzene rings as network formers, grows and the solution becomes more viscous.

The sol–gel films were deposited on silicon substrates or on fused silica slides, using a solution of 30 g/l SiO_2 concentration, by spin coating at 4500 rpm for 60 s. Variable thermal treatments on films were tested in order to modify film composition and optical properties, while preserving nanostructures fabricated on them, to reach refractive indices close to 1.33.

Samples were thermal treated as reported in Table 1.

	Thermal treatment	
Sample	**Temperature**	**Dwell Time**
1a	300°C	30 min
1b	300°C	60 min
2a	500°C	30 min
2b	500°C	60 min
3a	600°C	30 min
3b	600°C	60 min
4a	700°C	30 min
4b	700°C	60 min
5a	700°C	ramp=10°C/min 20 min
5b	700°C	10 min
5c	700°C	20 min

Table 1. Summary of the prepared samples and their respective thermal treatment conditions.

The refractive index and thickness of the films were estimated using a spectroscopic ellipsometry data and fits based on a Cauchy model, in the range of 300-1500 nm. Infrared absorption spectra were recorded in the 4500–400 cm^{-1} range by 620 JASCO FT-IR spectrometer with a resolution of 4 cm^{-1} averaging over 64 scans.

Data reported in Figure 5.9 show that the refractive index decreases for increasing temperature, from room temperature up to 700°C, as there is a complete solvent evaporation and the progressive elimination of the organic component of the film. The refractive index increases for higher treatment times, as condensation reactions and film densification are promoted. The lowest refractive index (1.40) is reached for thermal treatments on films at a fixed temperature of 700 °C for dwell times up to 20 min.

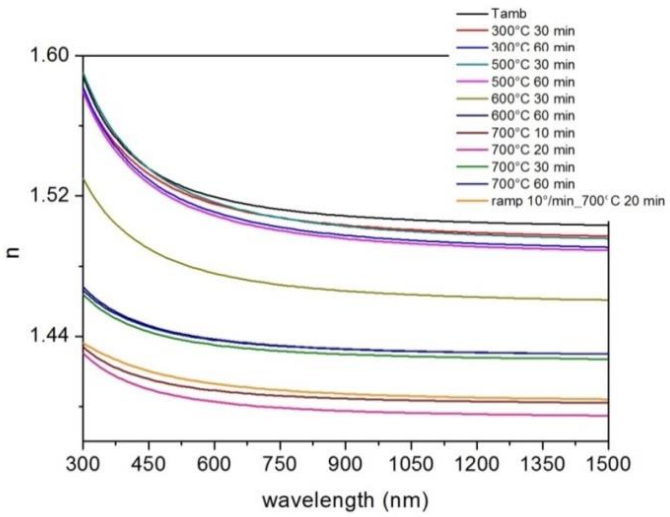

Figure 5.9 Refractive index of ph-PSQ films as a function of the wavelength, after different thermal treatments, measured by spectroscopic ellipsometry.

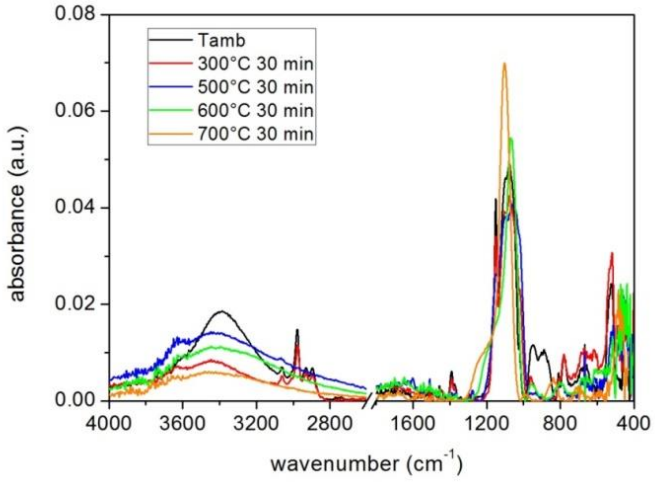

Figure 5.10 FT-IR absorption spectra of ph-PSQ flat films after different thermal treatments.

FT-IR absorption spectra of ph-PSQ films (Figure 5.10) confirm that increasing the temperature for a fixed dwell time determines gradual aromatic ring elimination. In particular, the peak intensity of the aromatic absorptions are reduced for increasing temperatures: C-H stretching at 3100-300 cm^{-1}, the sharp band at 1150 cm^{-1} typical of p-substituted sylphenylene groups, and C–H out-of-plane bending at 705 and 525 cm^{-1}. As regards film hydrolysis, methyl and methylene C–H stretching modes in the region 3000–2850 cm^{-1}, due to the presence of unreacted ethoxy groups ($–OCH_2CH_3$), continuously decrease to zero.

An increase in temperature leads to an higher condensation grade, indicated by the peak at about 1070 cm^{-1} corresponding to the increasing of Si-O-Si bonds number. Furthermore the decreasing of -OH stretching absorption band suggests that condensation becomes significant.

FT-IR absorption spectra of ph-PSQ films thermal treated at 700 °C (Figure 5.11) only slightly change as a function of the dwell time. The films are completely inorganic and porous. The Si-O-Si asymmetric stretching is revealed at relative low wavenumber (~1060 cm^{-1}) if compared to an inorganic silica-based sol-gel: this effect is related to the presence of porosity and to larger Si-O-Si bond angles compared to those found in pure dense silica.

The initial thickness is of 236 nm. A reduction in thickness of about 20%, 37%, 64% and 67% is observed for the samples respectively thermal treated at 300°C, 500°C, 600°C and 700°C (Figure 5.12).

As a conclusion of these investigations, we decided to perform thermal treatments at 700°C for 20 min to prepare low refractive index nanostructured surfaces with ph-PSQ.

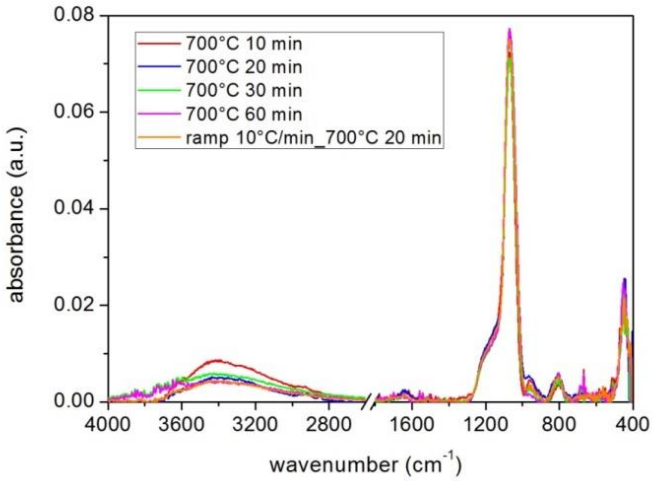

Figure 5.11. FT-IR absorption spectra of ph-PSQ flat films after thermal treatments at 700°C and variable dwell times.

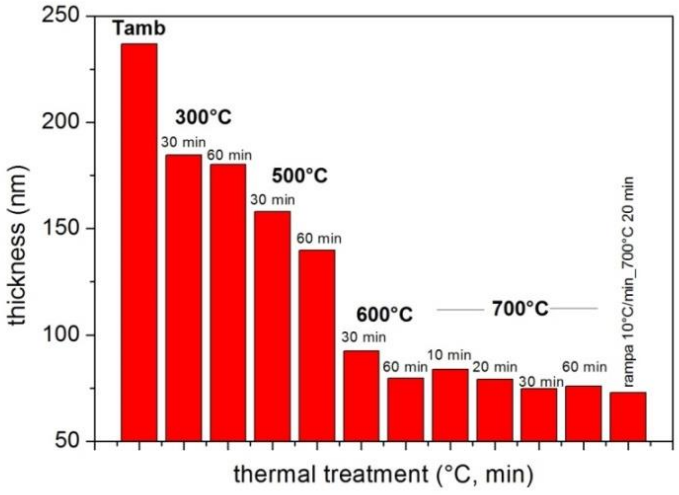

Figure 5.12 Thickness of ph-PSQ films after thermal treatment.

SPGs were fabricated through soft lithographic techniques, starting from sinusoidal patterns, realized by LIL on a Photoresist deposited on silicon.

Available masters are listed in Table 2, and selected images of AFM characterization are shown in Figure 8. The peak-to-valley height of the profiles was estimated from the Abbot curve as the height variation between the values corresponding to the 3% and 97% of the bearing area. The period is calculated from the position of the peak in the Fourier spectrum of the grating profile obtained by averaging over the horizontal scanned lines in an AFM image.

Master	Period	Peak to valley height
L1*	478 nm	30 nm
L2*	475 nm	23 nm
L3	476 nm	29 nm
7	588 nm	170 nm
8	584 nm	148 nm
10	582 nm	155 nm

Table 2. List of available sinusoidal masters and estimates of their morphological properties from AFM measurements.

Ph-PSQ works as a thermoset resist for NIL.

The sol–gel films were deposited on portions of silicon wafers or on fused silica slides by spin coating at 4500 rpm for 60 s. PDMS replica were gently pressed with a finger on fresh-deposited ph-PSQ films, and the assembly was cured with a 30 min thermal treatment at 80°C in an oven, before delicately peeling the mould off the sample. The fabricated sinusoidal patterns, positive replicas of the master structures, were imaged through an AFM (NT MDT) in non-contact mode for a morphological characterization, before applying annealing steps. Fabricated samples are listed in Table 3, and selected images of AFM characterization are shown in Fig. 5.13.

Sample	Substrate	Period	Peak to valley height
Laura 1*	silicon	478 nm	10 nm
L3	silicon	473 nm	21 nm
L1*	fused silica	459 nm	12 nm
L2*	fused silica	459 nm	10 nm
7a	silicon	575 nm	131 nm
7b	fused silica	560 nm	37 nm
7c	silicon	575 nm	139 nm
7d	fused silica	566 nm	140 nm
8a	silicon	575 nm	124 nm
8c	silicon	575 nm	124 nm

8d	fused silica	559 nm	131 nm
10a	fused silica	566 nm	93 nm
10b	silicon	579 nm	64 nm
10c	silicon	574 nm	128 nm
10d	fused silica	562 nm	101 nm

Table 3. List of patterned samples, and estimates of their morphological properties from AFM measurements.

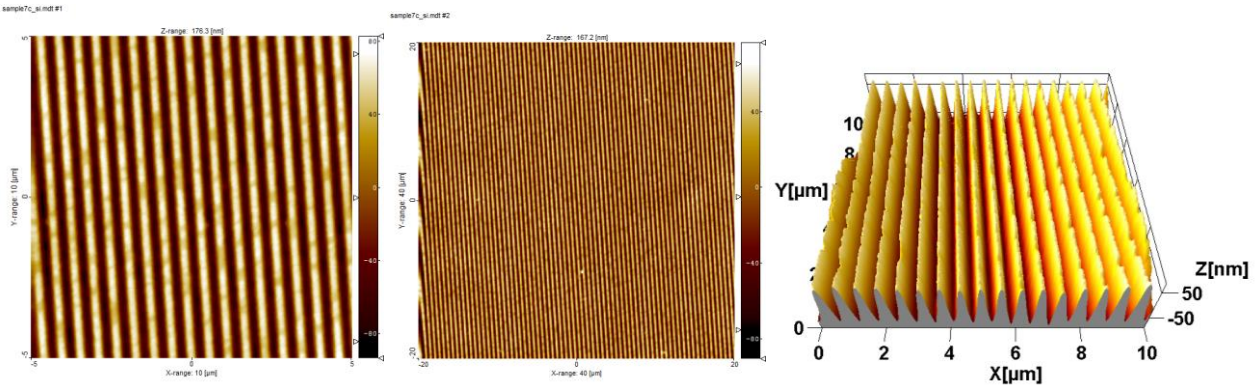

Figure 5.13. Sample (7C on silicon) AFM recordings of imprinted films before applying thermal annealing steps.

Thermal treatments at 700°C for 20 min were applied on the fabricated sinusoidal patterns with the aim of obtaining low refractive index nanostructures, as shown from previously reported investigations.

The AFM had z-calibration problems, thus were not able to provide a precise estimate of pattern geometry for these last hard-baked samples, still they visibly diffract light, and sinusoidal structures were imaged (see Fig. 5.14).

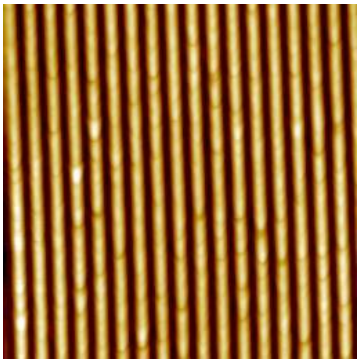

Fig. 5.14. Sample 7C AFM recording of imprinted film after applying thermal annealing step at 700°C for 20 minutes.

A metallic trilayer made of 7 nm of gold (Au) on top of 40 nm of silver (Ag) and a 5 nm Cr adhesion layer was deposited in vacuum onto the sinusoidal ph-PSQ gratings. The very thin Au

coating is necessary to avoid Ag oxidization in contact with air, which would create an oxide layer at the interface with the sensitive layer, compromising the SPP excitation; Cr is for adhesion promotion on oxides.

As the lowest reached refractive index for this sol-gel material was 1.40, the transfer of sinusoidal gratings on an commercial amorphous fluoropolymer (CYTOP) having a refractive index of 1.34, was optimized (fig. 5.15).

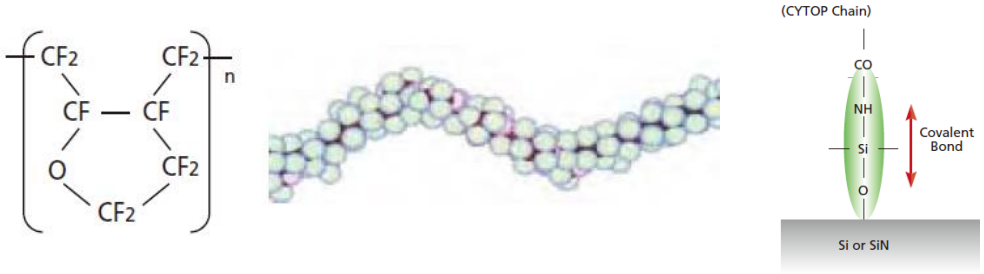

Fig. 5.15 Commercial amorphous fluoropolymer (CYTOP)

The CYTOP films were deposited on fused silica slides by spin coating at 4500 rpm for 60s (CYTOP/solvent=3/1) The fabricated sinusoidal patterns, positive replicas of the master structures, were imaged through an AFM (NT MDT) in non-contact mode for a morphological characterization. The types of fabricated samples are listed in the table 4, refractive indices and layer thicknesses of the CYTOP films are reported in Fig. 7.16 and selected images of AFM characterization are shown in Fig. 5.17-5.18-5.19.

Sample	Substrate	Period	Peak to valley height
G4	fused silica	1um	109 nm
1	fused silica	1.9 um	174 nm
2	fused silica	1 um	83 nm

Table 4. List of three typologies of patterned samples, and estimates of their morphological properties from AFM measurements.

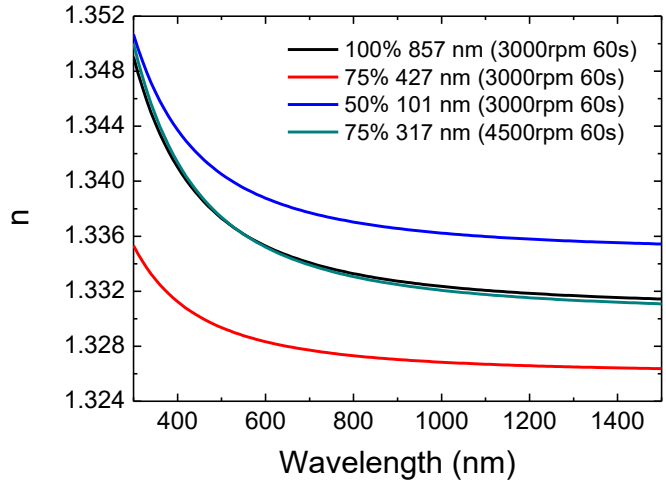

Fig. 5.16 Refractive indices and layer thicknesses of the CYTOP films obtained at different fluoropolymer/solvent dilutions.

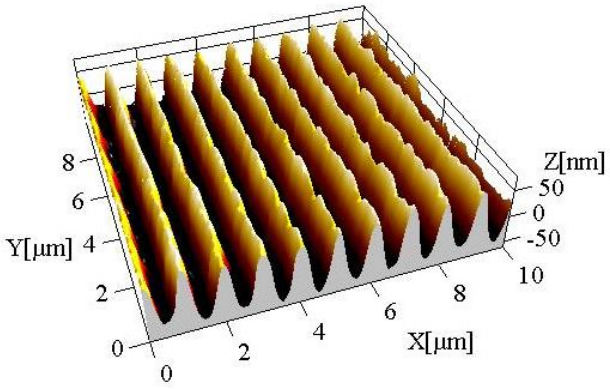

Fig.5.17 Sample 1: prebake for 1 min at 80°C and thermal treatment for30 min at 180 °C.

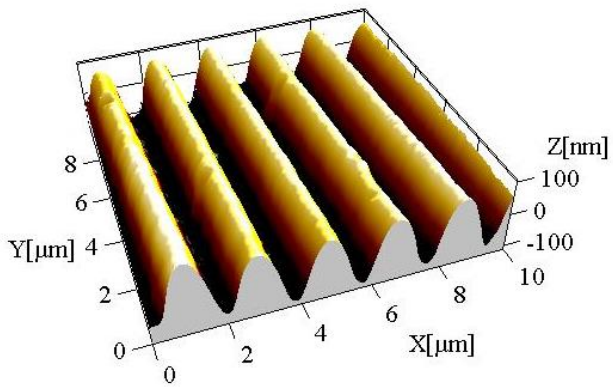

Fig.5.18 Sample 1: prebake for 1 min at 80°C and thermal treatment for30 min at 180 °C.

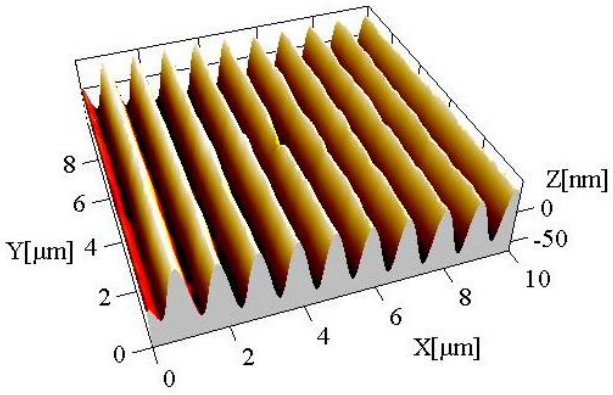

Fig.5.19 Sample 2: prebake for 1 min at 80°C and thermal treatment for 30min at 180 °C

The films were deposited on sodalime or on fused silica slides by spin coating at 4500 rpm for 60 s. A prebake step (1 min at 80°C) was carried out for some samples, to test whether film reological properties were further improved or not. Then PDMS replica were gently pressed with a finger on deposited CYTOP films, and the assembly was cured with thermal treatments at 180°C, before delicately peeling the mould off the sample. The fabricated sinusoidal patterns, positive replicas of the master structures, were imaged through an AFM (NT MDT) in non-contact mode for a morphological characterization. A metallic bilayer made of 7 nm of gold (Au) on top of 40 nm of silver (Ag) was deposited onto the sinusoidal CYTOP gratings.

5.3 The aptamer and metal surface functionalization: amine coupling.

For surface functionalization, ligand attachment to the surface via primary amine groups was adopted. In amine coupling, the carboxyl groups previously generated on a metal surface via interaction with 3-mercaptopropionic acid, are activated by injection of a mixture of N-hydroxysuccinimide (NHS) and N-ethyl-N'-(dimethylaminopropyl) carbodiimide hydrochloride (EDC). Formed active esters may readily react with amine groups of the aptamers. Ethanolamine is subsequently added in order to deactivate the remaining unreacted active esters.

Ampicillin binding aptamer (aptamer 5E01 #284, 40 DNA nucleotide bases, molecular weight: 12.239 g/mol) was purched from Base Pair Biotechnologies. The aptamer was selected from a randomized 40-mer DNA library against the target Ampicillin sodium salt with proprietary methods. For usage, a centrifugation of the purchased aptamer was performed to ensure that the dried aptamer pellet was at the bottom of the tube. The aptamer pellet was resuspended in a TE buffer (10 mM Tris HCl, 0.1 mM EDTA, pH 7.5) to achieve a 100 µM concentration. The aptamer

solution was incubated at room temperature for 30 min, then briefly vortexed. Aliquots of 20 μL were prepared and stored at -20 °C.

For surface functionalization, one aptamer solution aliquote was diluted in 180 μL of folding buffer (2 mM MgCl, 1xPBS, pH 7.4), to reach a concentration of 10 μM (150 μg/mL). Then, the solution was heated to 85-95 ºC for 5 min, and cooled to room temperature for 15 min before use.

Functionalization tests were performed on flat samples consisting of fused silica slabs with a Au coating.
The protocol developed during the first six months of reaserch activity, was further optimized as follows:
1. two different molecules with a carboxyl termination, 3-mercaptopropionic acid and lipoic acid, were dissolved in aprotic solvents at different concentrations. Among these, dimethylsulfoxide and dymethylformamide were tested but excluded as they are high boiling point solvents and plasticizers; acetonitrile and acetone didn't opacized, therefore negatively affecting, the gold surface. The most promising results were reached for samples that were immersed in a solution of 3-mercaptopropionic acid or lipoic acid (2mM) in acetonitrile for 2 hours.

2. Surface carboxylic acid groups were transformed into activated NHS esters by immersing the samples in a solution of 200 mM NHS in PBS solution and 200 mM EDC in H_2O. The addition of the aptamer to the mentioned solution finally allowed it to be covalently bound to the gold surface.

At each functionalization step, samples were rinsed with PBS.
A characterization of the functionalized samples was performed by cyclic voltammetry (CV) and electrochemical impedance spectroscopy (EIS) thanks to a collaboration with the group of Prof. C. Durante (University of Padua). CV is the most popular electrochemical technique used to study redox processes at SAM-modified electrodes. The terminal groups of SAMs have a great impact on the redox response and electron transfer resistance of redox probes in aqueous solutions, due to the electrostatic interaction between the terminal groups and ionic redox species.
CV mesurements were carried out with Metrohm AUTOLAB potentiostat/galvanostat PGSTAT302N managed by software Nova 1.6. Reference electrode and counter electrode used were respectively saturated calomel electrode (SCE) and Pt electrode. Supporting electrolyte used was PBS 1X (pH=7.4) and redox probe used was 1 mM potassium hexacyanoferrate.

In a CV experiment the working electrode potential is ramped linearly versus time. After the set potential is reached, the working electrode's potential is ramped in the opposite direction to return to the initial potential. These cycles of ramps in potential were repeated 5 times for each functionalization step. The current at the working electrode is plotted versus the applied voltage (i.e., the working electrode's potential) to give the cyclic voltammogram trace. By analysing the variation of peak current position as a function of scan rate it is possible to gain an estimate for the electron transfer rate constants.

At first the influence of two different solvents, acetonitrile and acetone, in the surface carboxylation step, was investigated while keeping constant all the other test conditions (Fig.5.20).

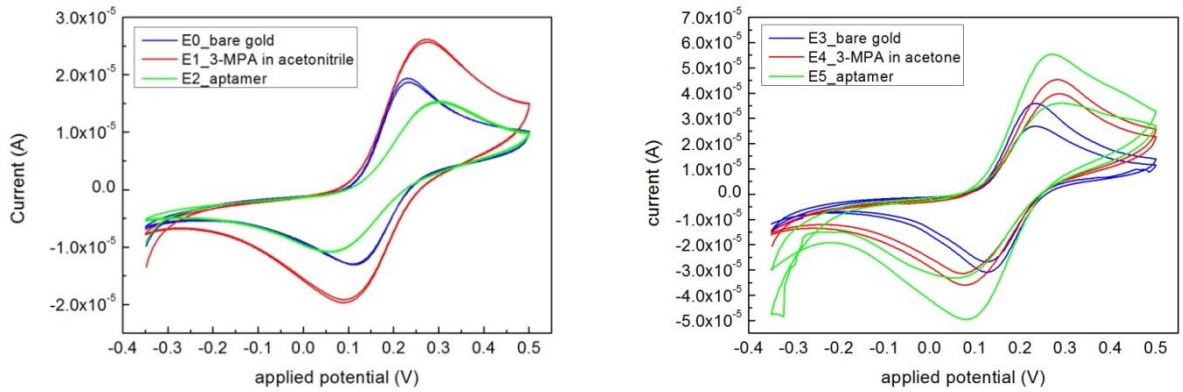

Fig. 5.20. Cyclic voltamogramms of the bare gold electrode (blue line), following modification of 3MPA in acetonitrile or in acetone (red line), 3-MPA +NHS/EDC solution + aptamer (green line).

Qualitatively a variation of the curves was observed at every functionalization step in both cases.

However acetone lowered the adhesion of the insulating tape used in the electrochemical measurements, modifying the selected active area and therefore giving falsified data compared to the others.

CV measurements were then carried out on another set of samples, choosing acetonitrile as solvent and comparing the effect of 3-MPA and lipoic acid (Fig. 5.21).

The use of these two different molecules affected the way the curves changed after the carboxylation step.

In this test it was not possible to lead the last step of the experiment, therefore bind the aptamer to the functionalized surface, as the PBS solution used to rinse the samples seemed to damaged them.

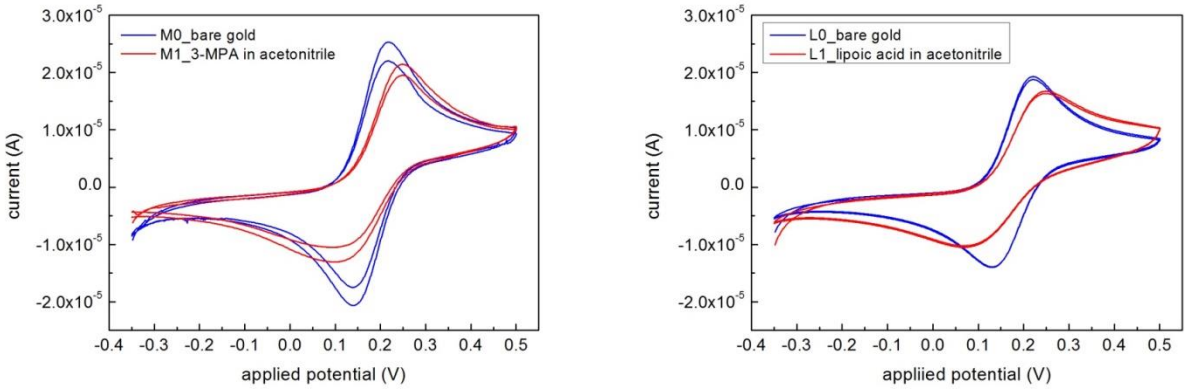

Fig. 5.21 Cyclic voltamogramms of the bare gold electrode (blue line), following modification of 3MPA or lipoic acid in acetonitrile (red line).

The tests were repeated on other samples. And electrochemical impedence spectroscopy was performed to quantatively characterize the sample biofunctionalization (Fig. 5.22-5.23).

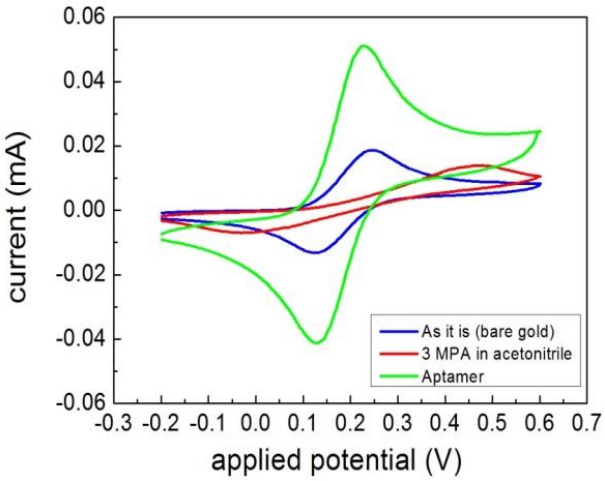

Fig. 5.22 Cyclic voltamogramms of the bare gold electrode (blue line), following modification of 3MPA in acetonitrile (red line), 3-MPA +NHS/EDC solution + aptamer (green line).

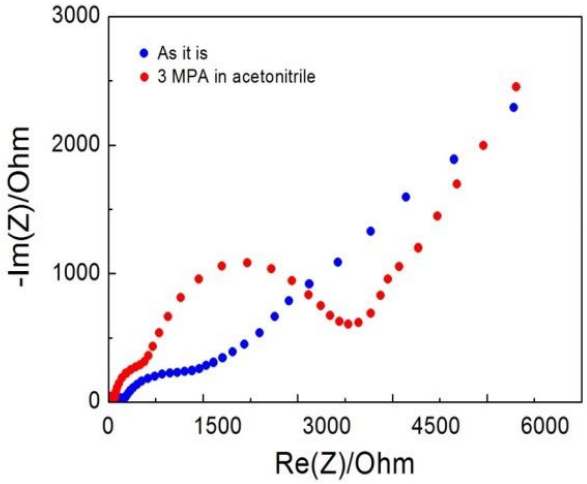

Fig. 5.23 EIS characterization of the bare gold electrode (blue line), following modification of 3MPA in acetonitrile (red line), 3-MPA +NHS/EDC solution + aptamer (green line).

Evidence of surface carboxylation was demonstrated by the shift and the lower current of the cathodic and anodic peaks compared to the bare gold , according to the fact that the surface was chemically modified. Furthermore, this result was confirmed by an increase of the resistance as shown by the impedence collected data. However aptamer binding to the surface was not possible due to the fact that the immersion of the sample in PBS solution somehow seemed to damage them. The functionalization procedure and characterization tests to verify its effectiveness are now being further investigated.

5.4 Simulations.

Simulations for grating-coupled plasmonic sensors were performed in collaboration with Dr. Enrico Gazzola (University of Padova, Physics and Astronomy Department). The previously reported refractive indices and layer thicknesses of the CYTOP films and grating period values of 750 and 1000 nm were considered. The plot of Fig. 5.24 relates to the theoretical plasmon moments at the upper and lower interface: the best symmetry condition for the structure occurs at the point where the two curves meet which correspond to a wavelength of about 670 nm. Considering a period of 750 nm, this plasmon can be excited at azimuth 0° with an incidence angle of about 31°, or with an azimuth-incidence pairs defined by the curve reported in Fig. 5.25.

Chandezon simulations were performed in the condition of back side illumination. In Fig. 5.26 are reported the angular scans at azimuth 0° for wavelength close to 670 nm. The peak to valley height is 60 nm and the period is of 750 nm. A resonance split is observed: for a wavelength of 670 nm,

the two plasmonic dip can be found close to 31°. For 40 nm shifted wavelength, the resonance split is still observed but dips start to appear distorted. Similarly, the spectral scansion is reported for a fixed angle of 31° in Fig. 7.27. Considering a grating a period of 1000 nm, similar graphs are obtained, but plasmonic dips are shifted at higher angles, close to 50°.

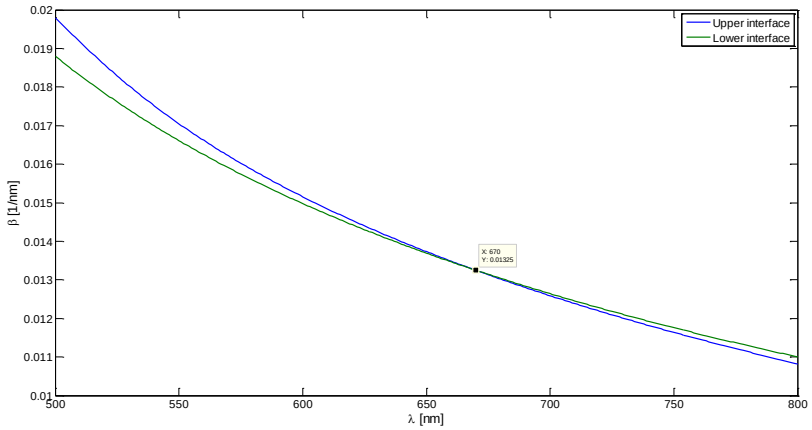

Fig. 5.24 Best symmetry conditions for structures with grating period values of 750 and 1000 nm.

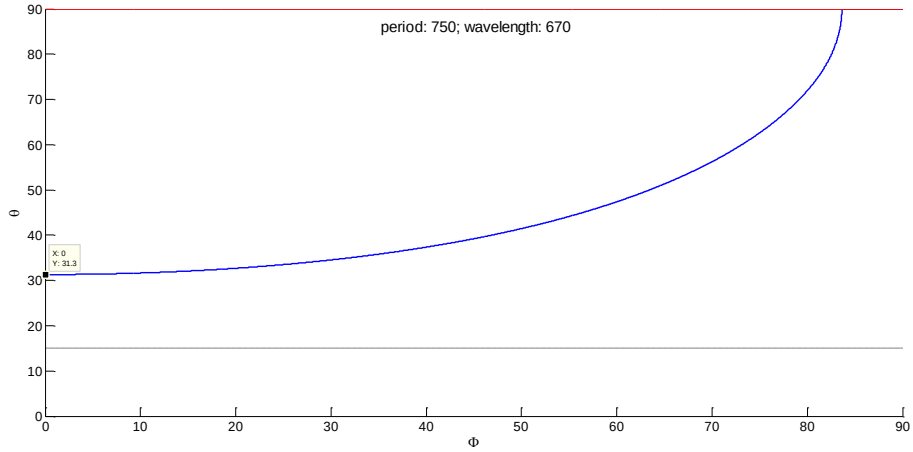

Fig. 5.25 Azimuth-incidence angle pairs for structures with a period value of 750 nm.

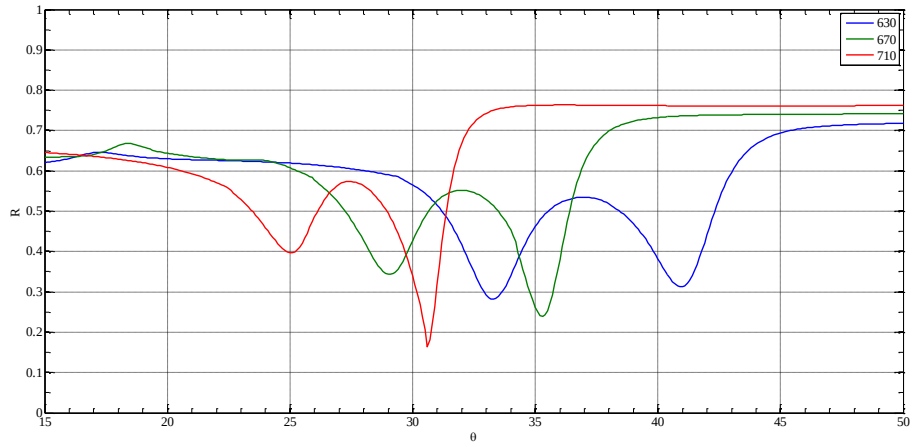

Fig. 5.26 Reflectance versus incidence angle for gratings with a period value of 750 nm.

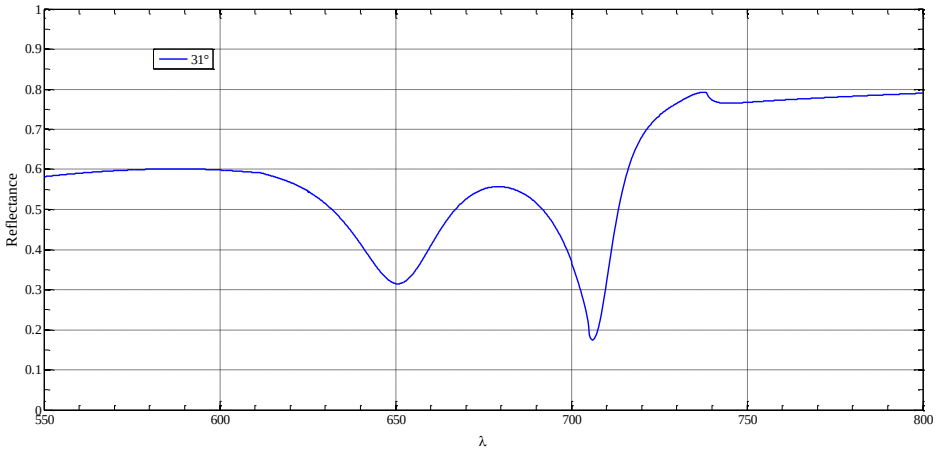

Fig. 5.27 Reflectance vs wavelength at fixed incidence angle of 31°.

In Fig.5.27 the angular scans at azimuth 0° for wavelength close to 600 nm (simulated data). In air, single interference dip is observed at 29° for both the samples here reported (fig. 5.28) , accordingly with the simulations.

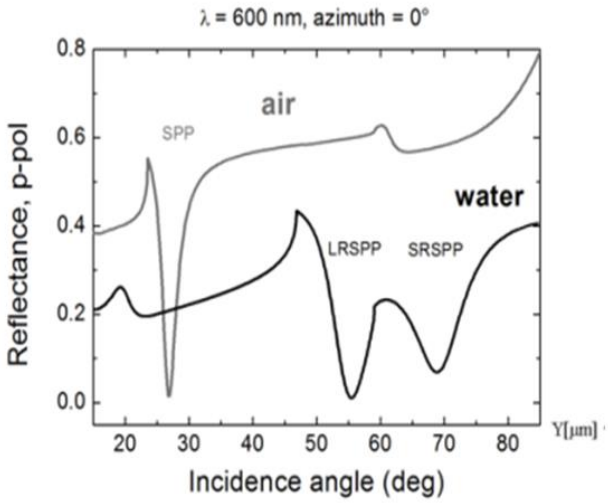

Fig. 5.28 Simulated reflectance spectra of the plasmonic grating in air and in water and experimental data in air.

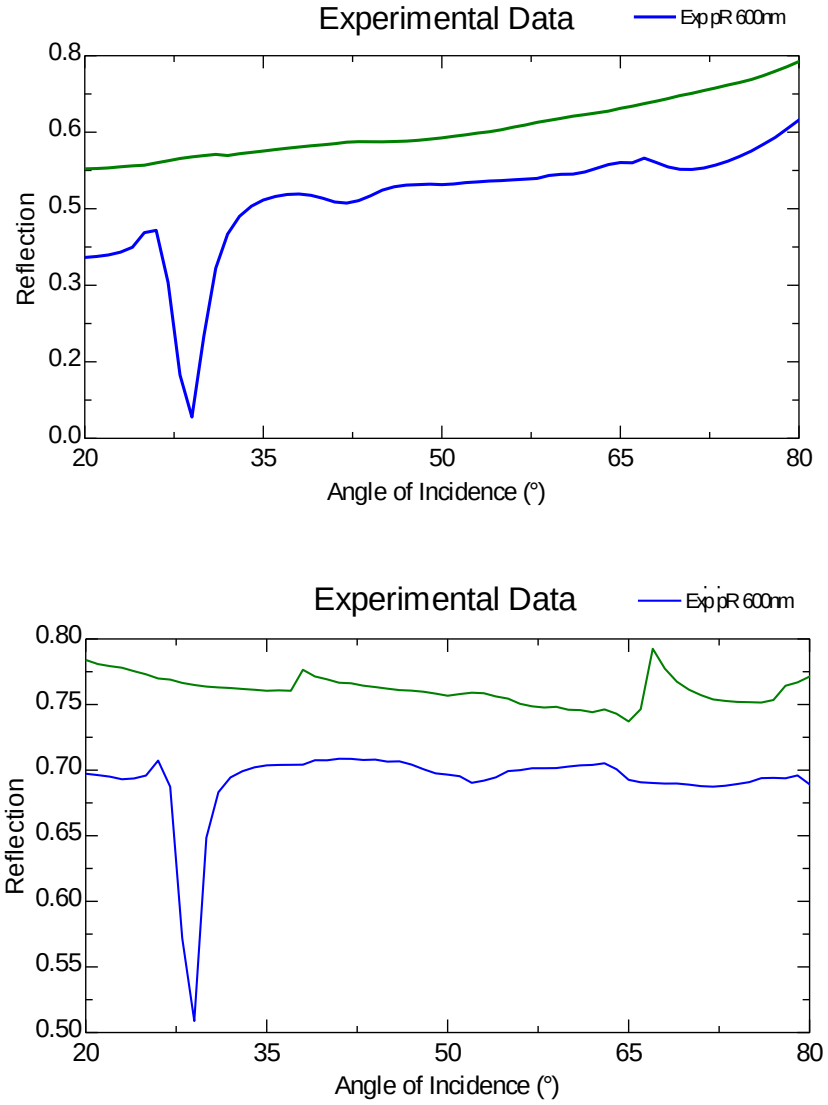

Fig. 7.29 Experimetal reflectance spectra of the plasmonic grating in air of two samples.

At this stage of the study it is still not possible to state which is the most performant system. However they both represent two potential promising strategies to face with the problem of the detection of antibiotic residues. In principle nanoparticles are more suitable for complex liquid media because magnetic extraction can be esaily performed, while plasmonic gratings are more stable, easier to be functionalized and, as shown, they allowed to obtain the very first sensing measurements.

Chapter 6

Conclusions

In this work functional materials and micro/nano structures for the realization of optical sensors for zinc ions or residual antibiotic detection in liquid media were developed.

As regard to the first biological application, a sensor system distinguished by a selective, dynamic and reversible response and able to detect zinc divalent ions in the biological range of interest was successfully obtained.

Engineered functional films were synthesized via a sol-gel process starting from different SiO_2 precursors: bridged polysilsesquioxanes and TEOS. The most promising systems were sol-doped with Zinpir-1 and film depositions were achieved through spin-coating.

By properly tuning the process parameters and by adopting different strategies, we obtained nanoporous and mesoporous systems.

The first developed host-guest system was synthesized starting from bridged silsesquioxane precursors presenting different organic fragments, which act as rigid rod spacers, allowing to enlarge the silica network, generating nanoporosity.

In the latter case, the thermal extraction of cetyltrimethylammonium bromide exploited as template allowed to have a mesoporous system. Furthermore soft-lithography was employed to induce the formation of a SiO_2 sinusoidal pattern allowing to increase the specific detection area, compared to flat films.

The sensor systems are dynamic as demonstrated by obtained response time in the order of tens of seconds. Nanostructured mesoporous silica-based films are more sensitive, having a detection limit of 100 nM in water, which falls into the concentration range of interest. Selectivity overall other ions was proved by sensing tests carried out in buffer solutions containing other species; stability of the systems was reached thanks to the adopted strategies to achieve immobilization of the flurophore, thus minimizing the leaching process. And furthermore a reversible behaviour of the samples was observed, which represents an important step forward in the development of these sensors as, to best of our knowledge, a similar result was not obtained before.

Several efforts were made for the integration of sensor films in microfluidic devices but further tests are still in progress as higher sensitivity measurement systems would be required. Besides solving this issue, further research work will concentrate on increasing the sensor performances pushing

toward the 100 nM selectivity in buffer solution or culture media. As final tests the sensor will be placed in chip where pancreatic islets are cultured, thus allowing to follow zinc fluctuations over time as a consequence of the release and spontaneous dissociation of the insulin-zinc complex.

Concerning the second project, related to a food industry application, two different plasmonic architectures were developed for performing high-sensitive, selective and cost-effective detection of residual antibiotics in milk. The proposed approaches are innovative with respect to sensor systems reported in literature and requiring challenging synthetic and technical solutions. The study was firstly focused on the detection of ampicillin, which belongs to the ß-lactams family.

The first structure consists of a sinusoidal surface plasmon metallic grating embedded in a refractive index symmetric architecture. This architecture was already studied by our research group to develop gas sensors. The system was modified and adapted to be exploited for the detection of analytes in complex liquid solutions, e.g in milk. The nanostructured plasmonic sensors were fabricated as sinusoidal metallic gratings deposited on a functional and porous hybrid sol–gel material, phenyl-bridged polysilsesquioxane (ph-PSQ), to be used in water. Thus, the requirement to be satisfied was the fabrication of a sinusoidal pattern with proper period and peak-to-valley height in a material of refractive index close to 1.33.

A preliminary study was conducted on thin ph-PQ films thermal treated at different conditions in order to modify their composition and optical properties, while preserving nanostructures fabricated on them. However combination of thickness and refractive index was not sufficient to produce symmetric gratings for excitation of LRSPP. Therefore the transfer of sinusoidal gratings on an commercial amorphous fluoropolymer (CYTOP) was optimized varying the thickness and dilution of Cytop. Simulations of the optical properties of grating-coupled plasmonic sensors were carried out and are in agreement with the experimental data.

The second architecture consists of superparamagnetic-core gold-shell nanoparticles of around 180 nm and having a resonance peak close to 520 nm.

Magnetite nanoparticle were prepared using polyol route through a multistep process.

The growth of an Au layer on the magnetic nanoparticle started with self-assembly of gold colloids on the magnetite nanoparticles, previously functionalized with an amine-modified alkoxide. The small gold nanoparticles of a few nm diameter acted as nucleation sites for the final reduction of plating solution with formation of a metal shell.

The colloidal samples were characterized through UV-Vis absorption spectroscopy and dynamic light scattering (DLS), SEM and TEM analysis to obtain information about dimension, composition and morphology of the synthesized system.

As regards future developments, encouranging results are being obtained concerning the functionalization of both the architectures and preliminary ampicillin detection tests in water are in progress. Further tests will be carried out to confirm the effectiveness of the functionalization protocol and to reach selective detection of ampicillin and other antibiotic residues in complex liquid media or in milk. The developed plasmonic architectures are suitable for straightforward integration of these sensor systems in a microfluidic chip. The work will involve the realization of such optofluidic device, able to test in situ small quantities of milk sample and, in principle, parallel multiple detection of different antibiotics using an array of variable selective functionalizations.

Thinking to potential further applications, these typologies of sensors can be engineered and exploited for highly sensitive detection of other analytes in complex liquid media. The selectivity will be provided by specific probe molecules functionalizing the plasmonic surfaces.

References

Introduction

[1] Prof. J. Homola (**2011**). Cycle of lessons on "Optical Biosensors" given at Department of Physics and Astronomy, University of Padova, 04-06/05/2011.

[2] M. Chudy, W. Wróblewski, A. Dybco, Z. Brzózka (**2001**). Chapter 3: Miniaturized chemical sensors in the monitoring of water in Novel head for testing and measurement of chemical microsensors. Anal. Chim. Acta, 429, 347 (2001).

Chapter 1

[1] R.E. Timms (**1971**). J. Chem. Soc. A 1969-1974.

[2] W. Stöber, A. Fink, E. Bohn (**1968**). Controlled Growth of Monodisperse Silica Spheres in the Micron Size Range. Journal of colloid and interface science, 1968, 26, 62-69.

[3] Douglas A. Loy and Kenneth J. Shea (**1995**). Bridged Polysilsesquioxanes. Highly Porous Hybrid Organic-Inorganic Materials. Chem. Rev. 1995, 95, 1431-1442.

[4] Li-Chih Hu and Kenneth J. Shea (**2011**). Organo-silica hybrid functional nanomaterials: how do organic bridging groups and silsesquioxanes moieties work hand-in-hand? Chem. Soc. Rev., 2011, 40, 688-695.

[5] Kenneth J. Shea and Douglas A. Loy (**2001**). Bridged Polysilsesquioxanes. MolecularEngineered Hybrid Organic-Inorganic Materials. Chem. Mater. 2001, 13, 3306-3319.

[6] K. J. Shea, D. A. Loy, O. W. Webster (**1992**). J. Am. Chem. Soc. 1992, 114, 6700.

[7] K. J. Shea, D. A. Loy, O. W. Webster (**1990**). Polym. Mater. Sci. Eng. 1990, 63, 281.

[8] D. A. Loy, J. P. Carpenter, S. A. Yamanaka, M. D. McClain, J. Greaves, S. Hobson, K. J. Shea (**1998**). Chem. Mater. 1998, 10, 4129.

[9] J. P. Carpenter, S. A. Yamanaka, M. D. McClain, D. A. Loy, J. Greaves, K. J. Shea (**1998**). Polym. Prepr. (Am. Chem. Soc., Div. Polym. Chem.) 1998, 39, 589.

[10] R. M. Shaltout, D. A. Loy, J. P. Carpenter, P. K. Dorhout, K. J. Shea (**1999**). Polym. Prepr. (Am. Chem. Soc., Div. Polym. Chem.) 1999, 40, 906.

[11] D. A. Loy, K. J. Shea, E. M. Russick (**1992**). Mater. Res. Soc. Symp. Proc. (Better Ceram. Chem. V) 1992, 271, 699.

[12] H. W. Oviatt Jr., K. J. Shea, J. H. Small (**1993**). Chem. Mater. 1993, 5, 943.

[13] D. A. Loy, G. M. Jamison, B. M. Baugher, E. M. Russick, R. A. Assink, S. Prabaker, K. J. Shea (**1995**). J. Non-Cryst. Solids 1995, 186, 44.

[14] L. Brigo, A. Pistore, G. Grenci, A. Carpentiero, F. Romanato, G. Brusatin (**2010**). New hybrid organic-inorganic sol-gel positive resist. Microelectronic Engineering 87 (2010) 947-950.

[15] L. Brigo, V. Auzelyte, K. A. Lister, J. Brugger and G. Brusatin (**2012**). Phenyl-bridged polysilsesquioxane positive and negative resist for electron beam lithography. Nanotechnology 23 (2012) 325302.

[16] L. Brigo, G. Grenci, A. Carpentiero, A. Pistore, M. Tormen, M. Guglielmi, G. Brusatin (**2011**). Positive resist for UV and X-ray lithography synthesized through sol-gel chemistry. J. Sol-Gel Sci. Technol. (2011) 60, 400-407.

[17] L. Brigo, E. Gazzola, M. Cittadini, P. Zilio, G. Zacco, F. Romanato, A. Martucci, M. Guglielmi and G. Brusatin (**2013**). Short and long range surface plasmon polarion waveguides for xylene sensing. Nanotechnology 24 (2013) 155502.

Chapter 2

[1] Larry L. Hench and Jon K. West (**1990**). *The Sol-Gel Process.* Chem. Rev., 90, 33-72.

[2] C. Jeffrey Brinker, George W. Scherer (**1989**). Sol-gel science. Academic Press, New York.

[3] E.R. Pohl and F.D. Osterholtz (**1985**). In Molecular Characterization of Composite interfaces.

Eds. H. Ishida and G. Kumar, New York, pg. 157.

[4] R.E. Timms (**1971**). J. Chem. Soc. A 1969-1974.

[5] W. Stöber, A. Fink, E. Bohn (**1968**). Controlled Growth of Monodisperse Silica Spheres in the Micron Size Range. Journal of colloid and interface science, 1968, 26, 62-69.

[6] Douglas A. Loy and Kenneth J. Shea (**1995**). Bridged Polysilsesquioxanes. Highly Porous Hybrid Organic-Inorganic Materials. Chem. Rev. 1995, 95, 1431-1442.

[7] Li-Chih Hu and Kenneth J. Shea (**2011**). Organo-silica hybrid functional nanomaterials: how do organic bridging groups and silsesquioxanes moieties work hand-in-hand? Chem. Soc. Rev., 2011, 40, 688-695.

[8] K. J. Shea and D. A. Loy (**2001**). Bridged Polysilsesquioxanes. Molecular Engineered Hybrid Organic-Inorganic Materials. Chem. Mater. 2001, 13, 3306-3319.

[9] K. J. Shea, D. A. Loy, O. W. Webster (**1992**). J. Am. Chem. Soc. 1992, 114, 6700.

[10] K. J. Shea, D. A. Loy, O. W. Webster (**1990**). Polym. Mater. Sci. Eng. 1990, 63, 281.

[11] D. A. Loy, J. P. Carpenter, S. A. Yamanaka, M. D. McClain, J. Greaves, S. Hobson, K. J. Shea (**1998**). Chem. Mater. 1998, 10, 4129.

[12] J. P. Carpenter, S. A. Yamanaka, M. D. McClain, D. A. Loy, J. Greaves, K. J. Shea (**1998**). Polym. Prepr. (Am. Chem. Soc., Div. Polym. Chem.) 1998, 39, 589.

[13] R. M. Shaltout, D. A. Loy, J. P. Carpenter, P. K. Dorhout, K. J. Shea (**1999**). Polym. Prepr. (Am. Chem. Soc., Div. Polym. Chem.) 1999, 40, 906.

[14] D. A. Loy, K. J. Shea, E. M. Russick (**1992**). Mater. Res. Soc. Symp. Proc. (Better Ceram. Chem. V) 1992, 271, 699.

[15] H. W. Oviatt Jr., K. J. Shea, J. H. Small (**1993**). Chem. Mater. 1993, 5, 943.

[16] D. A. Loy, G. M. Jamison, B. M. Baugher, E. M. Russick, R. A. Assink, S. Prabaker, K. J. Shea (**1995**). J. Non-Cryst. Solids 1995, 186, 44.

[17] L. Brigo, A. Pistore, G. Grenci, A. Carpentiero, F. Romanato, G. Brusatin (**2010**). New hybrid organic-inorganic sol-gel positive resist. Microelectronic Engineering 87 (2010) 947-950.

[18] L. Brigo, V. Auzelyte, K. A. Lister, J. Brugger and G. Brusatin (**2012**). Phenyl-bridged polysilsesquioxane positive and negative resist for electron beam lithography. Nanotechnology 23 (2012) 325302.

[19] L. Brigo, G. Grenci, A. Carpentiero, A. Pistore, M. Tormen, M. Guglielmi, G. Brusatin (**2011**). Positive resist for UV and X-ray lithography synthesized through sol-gel chemistry. J. Sol-Gel Sci. Technol. (2011) 60, 400-407.

[20] L. Brigo, E. Gazzola, M. Cittadini, P. Zilio, G. Zacco, F. Romanato, A. Martucci, M. Guglielmi and G. Brusatin (**2013**). Short and long range surface plasmon polarion waveguides for xylene sensing. Nanotechnology 24 (2013) 155502.

[21] L. Brigo, G. Grenci, L. Baù, A. Carpentiero, F. Mancin, F. Romanato, M. Tormen, M. Guglielmi, G. Brusatin (**2011**). Hybrid porous resist with sensing functionality. Microelectronic Engineering 88 (2011) 1913-1916.

[22] L. Brigo, M. Cittadini, L. Artiglia, G. A. Rizzi, G. Granozzi, M. Guglielmi, A. Martucci, G. Brusatin (**2013**). Xylene sensing properties of aryl bridged polysilsesquioxane thin films coupled to gold nanoparticles. J. Mater. Chem. C, 2013, 1, 4252.

Chapter 4

[1] W.J. Fischer, B. Schilter, A.M. Tritscher, R.H. Stadler, Encyclopedia of Dairy Sciences, 2nd Ed. (**2011**) 887-897

[2] http://www.dsm.com/markets/foodandbeverages/en_US/products/tests/delvotest.html

[3] J. Adrian, D. G. Pinacho, B. Granier, J.M Diserens, F. Sánchez-Baeza. A multianalyte ELISA

for immunochemical screening of sulfonamide, fluoroquinolone and ß-lactam antibiotics in milk samples using class-selective bioreceptors. Anal Bioanal Chem (**2008**) 391: 1703.

[4] B. G. Knecht, A. Strasser, R. Dietrich, E. Märtlbauer, R. Niessner, M. G. Weller. Automated Microarray System for the Simultaneous Detection of Antibiotics in Milk. Anal. Chem (**2004)** 76 (3), pp 646–654.

[5] http://foodsafety.neogen.com/en/betastar

[[6] J. Homola. Present and future of surface plasmon resonance biosensors. Anal Bioanal Chem (**2003**), 377:528–539

[7] J. Homola. Surface Plasmon Resonance Sensors for Detection of Chemical and Biological Species, Chem. Rev., (**2008)**, 108 (2), 462–493

[8] https://www.biacore.com/lifesciences/index.html

[9] A. G. Brolo. Plasmonics for future biosensors. Nature Photonics, **(2012**), 6, 709–713

[10] Yang Wang, Yuhua Shen, Anjian Xie, Shikuo Li, Xiufang Wang, and Yan Cai. A Simple Method To Construct Bifunctional Fe_3O_4/Au Hybrid Nanostructures and Tune Their Optical Properties in the Near-Infrared Region. J. Phys. Chem. C, (**2010)**, 114 (10), pp 4297–4301

[11] C. S. Levin, C. Hofmann, T. A. Ali, A. T. Kelly, E. Morosan, P. Nordlander, K. H. Whitmire, and N. J. Halas. Magnetic_Plasmonic Core_Shell Nanoparticles. ACS Nano, (**2009)**, 3 (6), pp 1379–1388

[12] L. Brigo, E. Gazzola, M. Cittadini, P. Zilio, G. Zacco, F. Romanato, A. Martucci, M. Guglielmi, G. Brusatin, Nanotechnology, 24 (**2013**) 155502

[13] R. Zheng, B.-W. Park, D.-S. Kim, B. D. Cameron, Biomed. Opt. Express. 2 (**2011**) 2731–2740.